



TECHNISCHE
UNIVERSITÄT
DRESDEN



INSTITUTO DE FÍSICA
Universidade Federal Fluminense

UNIVERSIDADE FEDERAL FLUMINENSE
INSTITUTO DE FÍSICA

Daniel Grimm

**Estudos do transporte em nanoestruturas
moleculares quasi unidimensionais a
partir de experimentos e modelos teóricos**

Tese apresentada como requisito parcial para obtenção do título de

Doutor em Física

Orientadores: Prof. Dr. Thomas Pichler & Prof. Dr. Andrea Latgé

Niterói 2008

Livros Grátis

<http://www.livrosgratis.com.br>

Milhares de livros grátis para download.

*To my beloved family,
Christiana & Juliano*

If liberty means anything at all,
it means the right to tell people what they do not want to hear.
Oscar Wilde

Abstract

This thesis comprises detailed experimental and theoretical investigations of the transport properties of one-dimensional nanostructures. Most of the work is dedicated to the exploration of the fascinating effects occurring in single wall carbon nanotubes (SWCNT). These particular nanostructures gained an overwhelming interest in the past two decades due to its outstanding electronic and mechanical features. The experimental work was carried out at the IFW Dresden, whereas the theoretical part was performed in the framework of the Brazilian-German research project *ProBral*.

We have investigated the properties of a novel family of carbon nanostructures, named here as Y-shaped rings. The studies show that they present very interesting quantum interference effects. A high structural stability under tensile strain and elevated temperatures is observed. Within the semi-classical potential adopted, the critical strain values of structure rupture lie in the same range of their pristine SWCNT counterparts. This is directly verified by the first observations of these ring-like structures in a transmission electron microscopy. A merging process of asymmetric into symmetric rings is investigated in-situ under electron beam irradiation at high temperatures. The electronic properties of these systems are theoretically studied using Monte Carlo simulations and environment dependent tight-binding calculations. From our results, we address the possibility of double-slit like interference processes of counter-propagating electron waves in the ring-like structures. The nature of well defined, sharp peaks in the density of states are determined as the discrete eigenenergies of the central loop part. Furthermore, the formation and dispersion of standing waves inside the ring is shown to originate from the quantum-dot like confinement of each branch between the leads. The obtained dispersion relation is shown to be the same occurring in purely one-dimensional quantum dots of similar geometries. Furthermore, Fabry-Perot-like interferences are observed.

We established at the IFW a bottom-up processing route to fabricate nanotube based electronic devices. The SWCNTs are grown by chemical vapor deposition and we present a detailed study of the different approaches to obtain individual nanotubes suitable for a successful integration into electronic devices. Wet-chemistry and ultra-thin films as well as ferritin were employed as catalyst particles in the growth of SWCNT samples. By adjusting the optimized process parameters, we can control the obtained yield from thick nanotube forests down to just a couple of free-standing individual SWCNTs. The nanotubes are localized, contacted by standard e-beam lithography and characterized at ambient- as well as liquid helium temperatures. We usually obtain quite transparent contacts and the devices exhibit metallic or a mixed metallic/semiconducting behavior. The well-known memory effect upon gate voltage sweeping as well as single electron tunneling in the Coulomb blockade regime are addressed.

Resumo

Nesta tese apresentamos resultados de investigações detalhadas, teóricas e experimentais, de propriedades de transporte de nanoestruturas quasi-uni-dimensionais. A maior parte do trabalho é dedicada à busca de efeitos interessantes que ocorrem em nanotubos de paredes únicas (SWCNTs). Tais nanoestruturas tiveram interesse crescente nas última duas décadas devido as suas características eletrônicas e mecânicas, consideradas bastante peculiares e promissoras. Todas as medidas experimentais foram realizadas no IFW Dresden, enquanto a parte teórica foi desenvolvida no âmbito do projeto de cooperação internacional, Brasil-Alemanha (*ProBral*).

Investigamos as propriedades de uma nova família de nanoestruturas de carbono, denominadas aqui de anéis em forma de Y. Os estudos mostram que elas apresentam efeitos de interferências quânticas bastante interessantes. Foi observado uma estabilidade acentuada destes sistemas quando submetidos a tensão e à altas temperaturas. A estabilidade desses sistemas do tipo anéis foi verificada pela primeira vez em medidas de microscopia de transmissão eletrônica. Investigações experimentais in-situ foram feitas e reportaram processos de transformações de anéis assimétricos em anéis simétricos quando submetidos à radiações de feixe eletrônico controladas e à altas temperaturas. Propriedades eletrônicas desses sistemas foram estudadas usando-se simulações de Monte Carlo e cálculos do tipo "Tight Binding" dependentes das configurações vizinhas locais. A partir de nossos resultados, propusemos a possibilidade de observar processos de interferência na propagação de elétrons nestas estruturas anelares do tipo os anéis em forma de Y. A natureza bem definida dos picos encontrados nas densidades de estados locais e globais foi determinada e relacionada com os auto-estados de energia da parte central dos laços estruturais. Além disso, mostramos que a formação e dispersão de ondas estacionárias nos anéis, tem como origem o confinamento do tipo ponto quântico que se manifesta em cada um dos ramos que formam os anéis entre os contatos.

Estabelecemos no IFW uma rota de processo do tipo "bottom-up" para fabricar nanotubos, baseada em dispositivos eletrônicos. Os SWCNTs são crescidos por deposição química de vapor e apresentamos um estudo detalhado de diferentes processos utilizados na obtenção de nanotubos individuais, adequados para uma integração bem sucedida em dispositivos eletrônicos. O controle da produção de largas florestas de tubos finos até um par de SWCNTs individuais suspensos a partir da otimização dos parâmetros dos processos foi alcançado. Os nanotubos são localizados e contatados a partir de litografias padronizadas utilizando-se feixes eletrônicos e caracterizadas tanto à temperatura ambiente quanto a 4K. Usualmente obtemos contatos muito transparentes e os dispositivos exibem comportamentos metálicos ou misturas de comportamentos metálicos e semicondutores. O conhecido efeito de memória mediante variação do valor da voltagem de porta, bem como o tunelamento de elétrons individuais no regime de Coulomb blockade são discutidos.

Contents

1	Motivation	13
1.1	Why carbon nanotubes	13
1.2	History	13
1.3	Properties and applications	14
1.4	Aim of this thesis	16
2	Transport in 1-dimensional systems	19
2.1	Transport regimes	19
2.1.1	Density of states of low-dimensional systems	20
2.2	Ballistic transport	21
2.3	Quantum interference effects in 1-dimensional structures	22
2.3.1	Coulomb-blockade	23
2.3.2	Higher-order tunneling: Cotunneling and Kondo effect	24
2.3.3	Fabry-Perot interference effects	25
2.4	The contact barrier problem	26
2.4.1	Schottky barrier formation	26
3	Basics of Carbon Nanotubes	29
3.1	Hybridization	29
3.2	Basics of Graphene	29
3.2.1	Crystallographic structure of graphene	29
3.2.2	Electronic structure of graphene	30
3.3	Basics of SWCNTs	32
3.3.1	Real space description of the SWCNT crystal structure	32
3.3.2	Reciprocal lattice of SWCNT	34
3.3.3	Electronic band structure of SWCNTs	35
4	Device fabrication	39
4.1	Placement of nanotubes	40
4.2	Imaging and precise positioning of the structures	40
4.3	Synthesis of SWCNTs - Basics	42
4.4	Chemical vapor deposition	43
4.4.1	Experimental setup	44
4.4.2	Characterization of the as-grown SWCNTs	46

4.5	Device fabrication: e-beam lithography	55
5	Theoretical model	59
5.1	Real-space tight-binding model	59
5.1.1	Green's function renormalization method	59
5.1.2	Electronic transport by the Landauer-Kubo formalism	61
5.1.3	Electronic transport in SWCNTs	62
5.2	Mechanical properties using a semi-quantical many-body potential	63
5.3	Environmental tight-binding description	65
5.4	Magnetic field effects	66
5.4.1	Application: DWCNTs in magnetic fields	69
6	Y-Junction rings & quantum dots	73
6.1	Atomic structure of SWCNT YJRs	73
6.2	Atomic configuration of SWCNT quantum dots	77
6.3	Experimental realization of YJRs	78
6.4	Thermal Stability	80
6.5	Mechanical strength of YJRs	83
6.6	Electronic properties	88
6.6.1	Strictly one-dimensional ring	88
6.6.2	General electronic properties of YJR	89
6.6.3	Standing wave formation in YJRs	91
6.6.4	Standing wave formation in quantum dots	95
6.6.5	Fabry-Perot oscillations	97
7	Transport measurements	99
7.1	Room temperature transport measurements of SWCNT devices	99
7.1.1	Removing redundant CNTs in ready devices	102
7.2	Low temperature measurements	105
7.2.1	Theory of single electron tunneling	106
7.2.2	Measurements of the Coulomb blockade regime at 4.2K	109
7.3	Non-carbon nanostructures	111
7.3.1	Transport properties of non-carbon nanostructures	112
8	Conclusions & Outlook	115
8.1	Conclusions	115
8.2	Outlook	118
	Bibliography	119
	List of Publications & Curriculum Vitae	129
	Acknowledgements	133

List of Figures

2.1	DOS in low dimensional systems	21
2.2	Short channel length SWCNT devices	22
2.3	Coulomb blockade of SWCNT devices at T=4K.	24
2.4	Fabry-Perot oscillations of SWCNT devices at T=4K.	25
2.5	Formation of Schottky barrier between a metal and semiconductor . .	27
2.6	Basic operation of a CNTFET upon applying bias and gate voltage .	28
3.1	Honeycomb lattice of a graphene sheet in real and reciprocal space .	30
3.2	Energy dispersion relation of graphene	31
3.3	Tinkering instructions of rolling up a SWCNT	32
3.4	Schematic atomic configurations of SWCNTs	33
3.5	Allowed \vec{k} vectors of SWCNTs in the graphene Brillouin zone	34
3.6	Energy dispersion of SWCNTs	36
3.7	LDOS of SWCNTs	37
4.1	Positioning and EBL layout procedure	41
4.2	Hot wall CVD reactor used for the nanotubes synthesis	45
4.3	FT-Raman spectra as function of temperature as well as multi-line laser Raman spectra of an optimized SWCNT sample	46
4.4	TEM images of SWCNT and MWCNT synthesized at 680°C	47
4.5	Bulk CNT samples employing wet-catalysts and multilayers	48
4.6	SWCNT growing on homogeneously evaporated thin-film catalysts . .	50
4.7	Ferritin and Co-Apoferritin catalyzed synthesis of SWCNT	51
4.8	Individual SWCNTs growing off pre-patterned wet-chemistry islands .	52
4.9	Individual SWCNTs growing off pre-patterned thin film catalyst islands	53
4.10	Towards free-standing nanotubes devices on Si ₃ N ₄ membranes	54
4.11	e-Beam lithography cycle	55
4.12	Resist structure	57
5.1	Schematic representation of a zigzag SWCNT and its hopping integrals	60
5.2	Schematic picture of a conductor connected to two semi-infinite leads	61
5.3	Conductance of zigzag SWCNTs	63
5.4	Aharonov-Bohm effect in MWCNT	67
5.5	Band structure of SWCNTs under influence of a magnetic field	68

5.6	Energy gap evolution under the influence of an axial magnetic flux . . .	69
5.7	Schematic view of the atomic configuration of a (5,5)@(10,10) DWCNT	69
5.8	Electronic properties of DWCNTs in a magnetic field	71
6.1	Snapshots of several relaxed configurations of small YJR at 0 K	74
6.2	Equilibrium atomic and potential energy configurations of YJRs	75
6.3	Formation energies and length contraction of different YJR systems .	76
6.4	Side and cross-sectional view of a quantum dot and YJR	77
6.5	Transmission electron micrographs of asymmetric and symmetric YJRs	79
6.6	Temperature dependence of the potential energy of small YJRs	80
6.7	Coalescence process of small symmetric YJR	82
6.8	Length variation dL/L_0 versus temperature	83
6.9	Stone-Wales defect formation and activation barrier energy	84
6.10	Closeups of the polygon opening in strained YJRs at 800K	85
6.11	Atomic energies and bond angle distribution as function of strain . .	86
6.12	Atomic configuration of YJRs under strain at 300K	87
6.13	Conductance and LDOS of a 1D chain	88
6.14	Conductance of a 1D-ring and YJRs as function of branch length . .	89
6.15	Conductance and total DOS of metallic and semiconducting YJRs . .	91
6.16	LDOS energy contour plots and atomic structure maps of YJRs	92
6.17	LDOS map of asymmetric metallic YJRs	93
6.18	LDOS map of symmetric semiconducting YJRs	94
6.19	Standing wave dispersion in YJR adopting CHI and EDHI approaches	95
6.20	LDOS energy contour plots of a QD compared to a metallic YJR . .	96
6.21	Standing wave dispersion relation in QDs and YJRs	96
6.22	DOS and conductance of a quantum dot	97
7.1	Equipment of the sample mounting for transport measurements	100
7.2	Transport measurements of SWCNT devices at room temperatures .	101
7.3	Memory effect of SWCNT devices in ambient environment	101
7.4	Controlled electrical burn-down of nanotubes	102
7.5	Electronic device sustaining large currents	103
7.6	H ₂ O etching of unwanted CNTs in ready devices	104
7.7	Equipment for low-temperature measurements	105
7.8	Electric circuit diagram of a SWCNT quantum dot	106
7.9	Schematic level diagram of the Coulomb blockade regime	107
7.10	Coulomb blockade oscillations at 4.2K	109
7.11	Coulomb blockade transistor at 4.2K	110
7.12	Transport results vs. gate voltage in the Coulomb blockade regime . .	111
7.13	Transport properties of manganese dioxide nanotubes	112

Abbreviations used in this thesis

AB	Aharonov-Bohm (effect)
AFM	atomic force microscope
CB	Coulomb blockade
CHI	constant hopping integral (approach)
CI	constant interaction (model of quantum dots)
CNT	carbon nanotube
CVD	chemical vapor deposition
DOS	density of states
DWCNT	double-wall carbon nanotube
EBL	electron-beam lithography
EDHI	environment-dependent hopping integral (approach)
E_f	formation energy
E_F	energy of the Fermi level
E_c	energy of conduction band edge
E_v	energy of valence band edge
FIB	focused ion beam
FET	field effect transistor
ϕ_0	magnetic flux quantum = $h/e = 4.13 \times 10^{-15} Tm^2$
FT Raman	Fourier Transform Raman
Γ_0	conductance quantum = $2e^2/h = (13k\Omega)^{-1} = 1/\rho_0$
γ_0	tight-binding hopping parameter $\approx -2.7eV$
I_{ds}	drain to source current
MC	Monte Carlo (simulation)
MWCNT	multi-wall carbon nanotube
PMMA	polymethyl methacrylate (resist for e-beam lithography)
QD	quantum dot
RBM	radial breathing mode
SB	Schottky barrier
s_c	critical tensile strain
SET	single electron tunneling
SEM	scanning electron microscope
SW	Stone-Wales (defect)
SWCNT	single-wall carbon nanotube
TB	tight binding (approximation)
TEM	transmission electron microscope
vHs	van Hove singularities (one-dimensional DOS peaks)
V_a	acceleration voltage (in electron microscopy)
V_{ds}	drain to source voltage (bias)
v_F	Fermi velocity (= $8.5 \times 10^5 m/s$ in SWCNTs)
V_g	gate voltage
YJR	Y-junction ring

1 Motivation

1.1 Why carbon nanotubes

Why should we investigate carbon nanotubes? The answer lies in the peculiar properties of carbon. Carbon is presumably the most diverse and important element in the periodic table and is one of the few elements known to man since antiquity. In most compounds known and employed nowadays in biology, chemistry and solid-state physics, carbon plays the major role. It has a high affinity to form multiple bonds as well as bonds with other atoms which lead to a vast variety of allotropes. It is the only element which is present in all dimensions, i.e., diamond (3d), graphite (nearly 2d), graphene (2d), carbon nanotubes (1d) as well as Buckminsterfullerenes (0d). Its electronic properties range from insulating (diamond), semiconducting (nanotubes, fullerenes), semimetallic (graphene, nanotubes) to metallic (nanotubes). It can be transparent and the toughest natural mineral known (diamond) as well as be black colored, highly ductile and serving as dry lubricant (graphite).

Among the different allotropes, the discovery of fullerenes in 1985 and carbon nanotubes (CNT) initiated a real 'boom' of carbon-based investigations worldwide. The experimentalists were fascinated because for the first time they had a true low dimensional hollow molecule at hand, mechanically very stable with superb electronic properties. On the other hand, the theoreticians were captivated by the well understood easy honeycomb-based crystal structure and could predict many interesting properties verified later on by experiments. The importance of these developments can be quantified by the fact, that just eleven years after the first synthesis of fullerenes, their discoverers R.F. Curl, H.W. Kroto and R.E. Smalley were decorated with the Nobel Prize in Chemistry.

1.2 History

But the story actually does not start here. One-dimensional structures have been a rich and active playground for theoreticians for many decades. The possibility to use molecules as building blocks for electronic devices was already foreseen by R. Feynman in 1959[1]. But the technology was always a step behind and only late in the 70s the theoretical predictions and experimental realization first met in the field of conductive polymers. The technology interest was huge and many advances

could be achieved due to the progress in synthesis and characterization techniques. Nevertheless, the conductivity remained low and only in the 90s the world gained a truly one-dimensional system with exceptional high current densities, the carbon nanotubes.

Already the Crusaders encountered extraordinary mechanical properties of the opponent Muslim's Damascus blades. Recently it was shown by a group of the TU Dresden, that a Damascus sabre from the seventeenth century contained CNTs as well as cementite nanowires creating an ultrahigh carbon steel[2]. The possibility of the existence of CNTs by rolling-up a graphene sheet, just like a honeycomb wax candle, was foreseen at a Carbon Workshop in 1990[3]. Indeed, in 1991 the first clear unambiguous evidence for the possibility of growing carbon nanotubes was reported by Iijima[4]. Thus, many papers in the field of carbon nanotubes start with the reference "the discovery of carbon nanotubes by Iijima in 1991...". This paper published in *Nature* had an overwhelming impact on the scientific community of the nanoscale which was just emerging at these times. Nevertheless, the credit of the discovery should be given to two Russian scientists, which published back in 1952 in the *Journal of Physical Chemistry of Russia* several micrographs of tubular and hollow graphite fibers, possibly multi-walled carbon nanotubes (MWCNT) 50nm in diameter, obtained by iron assisted synthesis[5]. This fact was brought to light only recently due to the difficult access and language (for the Western scientists) of the original paper. Unfortunately, the world was ready to realize and implement the intriguing properties of carbon nanotubes only 40 years later.

It is perfectly clear that the formation of single-wall carbon nanotubes (SWCNT), tubes with only one shell, was first reported in 1993 by two independently submitted contributions[6, 7]. Actually, in both cases the discoveries were in fact failed attempts to produce MWCNT filled with transition metals. Up to now, the synthesis of SWCNTs is quite similar to the reported one: it requires high temperatures and the aid of catalytic action. From now on, the CNT community should steadily grow and many important insights into the world of the nanoscale could be gained.

1.3 Properties and applications

There are many ideas how to implement and where to benefit from the interesting properties of carbon nanotubes. Their huge mechanical strength with a Young's modulus in the range of TPa, the highest among known materials, makes CNTs a natural candidate for strength-enforced materials, such as sports gear or bullet-proof jackets. Even the vision to built a space-elevator based on a carbon nanotube cable is seriously envisaged. Its outstanding electronic properties, which can be merely by geometric changes triggered from metallic to semiconducting, raise many possible applications in electronic industries. The metallic CNTs behave as ballistic conductors with the ability of carrying huge current densities, whereas the semiconducting

ones can be implemented in switching devices. Up to now, the improvement in switching rates of modern logical circuits was mainly achieved through miniaturization of bulk semiconductors. When following Moore's law, a prediction which foresees that the number of transistors in a integrated circuits should double each two year, the downscaling of bulk semiconductor will reach its limit in a couple of decades. New materials and device concepts are needed in order to overcome those limitation. This makes understandable, why so many hope and efforts were and still are put into the investigations of CNTs. The major drawback is the up-scalability and mass-production of CNT based circuits. Most experimental measurements reported in this field require a prior arduous student work on individual electronic devices. However, several successful many-circuitry approaches are already realized, e.g., the controlled mass-deposition of individual SWCNT in electric fields with millions of devices per cm^2 [8], controlled electrical breakdown [9] or lithography-free contacting of in-situ grown CNTs in a parallel device concept[10].

Substantial insights into fundamental physics notions could be reviewed and verified in the theoretical and experimental research of carbon nanotubes. Due to their low-dimensionality, many effects are driven by basic quantum mechanical concepts. Furthermore, new structures and multi-terminal devices could be idealized and realized based on CNTs by controlled synthesis employing a template-based chemical vapor deposition technique[11] or, alternatively, by joining SWCNTs with the use of an electron beam[12]. In the latter method, exposure of the cross-contact region to the beam causes structural changes that promote the merging, leading to the formation of X-shaped type of junctions. Later, under careful irradiation, a branch of an X junction may be removed to produce T- or Y-shaped junctions. Junctions composed of semiconducting and metallic nanotubes have been explored and also junctions with three points acting as transistors[13, 14]. Annular structures[15] can be very useful for investigating interesting physical phenomena such as Aharonov-Bohm effects[16–18], magnetotransport[19–21] and the establishment of persistent currents[22]. Fano resonances and orbital filtering in multiply connected SWCNTs have been discussed[23].

Shortly after the synthesis of CNTs, the first implementations in electronic devices were realized. A lot of progress was achieved since then, mainly in diminishing the contact resistance of the electrodes to the nanotubes. The technological advances allowed the fabrication of very small device channel lengths with near transparent leads. It turned out, that many phenomena are driven by the resulting quantum confinement not only around the nanotube circumference but also along the nanotube axis. Well-known quantum effects were observed for the first time in purely one-dimensional structures, namely Kondo effects[24, 25] and Fabry-Perot interferences[26, 27], among others. In this device configuration, the nanotube channel acts as a quantum dot with discrete energy level spacing, similar to the case of double heterojunctions[28], where nanotubes serve as the metallic leads coupled to a finite-sized nanotube of different diameter[29, 30].

1.4 Aim of this thesis

The scope of this thesis is a combined theoretical and experimental investigation of quantum interference effects in SWCNT based electronic devices. For this purpose, a thorough study on the mechanical and electronic properties of SWCNT based systems was carried out. The structural stability of a new ring-like system was demonstrated based on theoretical calculation and subsequently proven by high-resolution images in a transmission electron microscope. A controlled structural reshaping route, converting an asymmetric into a symmetric ring, was developed under high-energetic electron beam exposure in a high-temperature environment. Many interesting quantum effects could be observed in the theoretical transport calculations of the interferometric structure as well as in SWCNT quantum dots. The challenging project was the combined investigation of theory and experiment of those peculiar quantum interference effects. For this purpose, we installed and improved a new experimental setup at the IFW. We followed a bottom-up device fabrication where all process steps are made in the IFW. We managed to synthesize SWCNTs via chemical vapor deposition (CVD), integrated the as-grown nanotubes in electronic devices fabricated by employing top-electrodes patterned via electron beam lithography (EBL) and determined the electronic properties in preliminary transport measurements.

In order to present a complete and conclusive picture, chapter 2 introduces some basic concepts of electronic transport in one-dimensional systems. Basic length scales are compared with the dimensions of the systems and the consequences caused by the confinement in all spatial directions is shown. Interference effects caused by the discrete energy level spacing as well as Fabry-Perot like interferences are depicted. Furthermore, the omnipresent contact problem of the electrodes is touched as well as the possibilities of improving the coupling between the nanotubes and leads. Chapter 3 concentrates on the peculiar properties of carbon nanotube and define the basic notation used throughout this thesis. The next chapter 4 deals with the detailed fabrication process of the electronic devices. We introduce the different ways of placement and precise localization of nanostructures on a insulating dielectric. We summarize the results and characterizations of diverse CVD synthesis processes and determine the optimal parameters of SWCNT growth suitable for integration in electronic devices. In chapter 5, a detailed description of the theoretical tight-binding model based on a Green's function formalism entirely defined in the real space is specified. This model is able to include any topological defects as well as arbitrary SWCNT-based structures in the formalism and we present a proposal of an environment dependent tight-binding approach. The effects of an external magnetic field are incorporated in the real-space Green's function using the Peierls phase approximation and as an example, we touch on the electronic properties of double-wall CNTs under the influence of a magnetic field. In chapter 6 we introduce a new proposed SWCNT ring-like system resembling two interconnected Y-junctions and compare the transport properties with SWCNT quantum

dots. We present the atomic configurations and a thorough study of the mechanical and electronic properties of both systems. We demonstrate the high structural stability of Y-junction rings (YJR) evidenced by the first experimental realization of these double-slit like interferometers. Subsequently, we explore by theoretical calculations the rich quantum interference effects, including standing wave formation and Fabry-Pero-like oscillations. The preliminary results of the experimental realization of electronic devices are summarized in chapter 7. Transport measurements at room temperature demonstrate the memory effect upon gate voltage, whereas low temperature measurements show well-defined Coulomb blockade peaks. At the end of this thesis we present in chapter 8 our conclusions of this work and give a short outlook on ongoing experiments as well as means to achieve free-standing interferometric transport devices to verify the theoretical predictions.

2 Transport in 1-dimensional systems

A macroscopic conductor usually shows Ohmic behavior. This picture changes when we consider electronic transport in nanostructures. When thinking of a conventional ohmic system, the conductance Γ reads linear in the size-independent conductivity σ as $\Gamma = \sigma W/L$, with W and L being the width and length of the conductor. As the size of a device becomes comparable to the electron coherence length, this classical conductance formula cannot longer stand, because it would diverge for small lengths. Thus, we have to review our concept of resistance at the microscopic level. Quantized transport and quantum interference effects between electron waves become increasingly important, leading to dramatic changes in transport properties, especially at low temperatures[31, 32]. As nanotubes (carbon and others) can be considered as very thin cylinders (1-100nm in diameter), such effects certainly will dominate the transport properties in these molecular systems.

2.1 Transport regimes

Using 3 basic characteristic lengths, we can divide the electronic transport in three regimes: ballistic, diffusive and classical (macroscopic) transport.

Fermi wavelength λ_F

At low temperatures, the current is carried mainly by carriers at and near the Fermi energy. The also so-called de Broglie wavelength is defined as

$$\lambda_F = 2\pi\hbar/mv_F \quad , \quad (2.1)$$

with $v_F = \hbar k_F/m$ being the Fermi velocity, which in SWCNTs is $v_F = 8.5 \times 10^5 m/s$ [33]. Thus, it is related to the kinetic energy of the electron. In a 2-dimensional free-electron gas, λ_F scales down with the root of the electron density n . In modern semiconductor heterostructures, the Fermi wavelength can become as large as $100nm$ and may be comparable to the structure size.

Mean free path L_m

Simply speaking, the mean free path L_m is the average distance an electron can travel

through the structure before scattering at impurities, phonons or other electrons and thus changing its momentum:

$$L_m = v_F \tau_m \quad , \quad (2.2)$$

with the momentum relaxation time τ_m being the time until an electron suffers collision. The mean free path in high mobility semiconductors can reach several tenths of μm . The mobility μ can be defined analogously as $\mu = \frac{e}{m} \tau_m$.

Phase coherence length L_ϕ

The phase coherence is destroyed by inelastic scattering events at a time scale of τ_ϕ . Only fluctuating scatters are able to destroy the phase of the electrons by individual collisions. The elastic and inelastic scattering processes are expected to freeze out at low temperatures and thus, both length scales to depend strongly on the temperature.

Now we can relate the system's dimension L with these lengths and can distinguish several transport regimes:

Ballistic	$L \ll L_m, L_\phi$	No significant momentum and phase relaxation.
Diffusive	$L_m < L < L_\phi$	Involves many elastic scattering events but the electrons remain coherent with no substantial phase relaxation.
Classical	$L_m, L_\phi \ll L$	Both momentum and phase relaxation processes occur frequently and thus an electron can be considered as a particle. The resistance obeys the simple Ohm's law.
Size quantization	$L < \lambda_F$	Size quantization effects have to be taken into account.
Weak localization	$L_\phi \approx L \ll L_c$	Conductor with M channels can be divided into phase-coherent units with many scatterers (localization length $L_c \sim M \cdot L_m$). Transport reduction by $\sim e^2/h$. Can be easily destroyed by a weak magnetic field.
Strong localization	$L_c < L_\phi \approx L$	Transport suppression.

2.1.1 Density of states of low-dimensional systems

The density of states $\rho(E)$ represents the number of states per volume in a small energy range between E and $E + \delta E$. Thus, the local density of states (LDOS) is proportional to $|\delta E(\vec{k})/\delta \vec{k}|^{-1}$. In general, due to the spatial confinement we obtain the following dependencies:

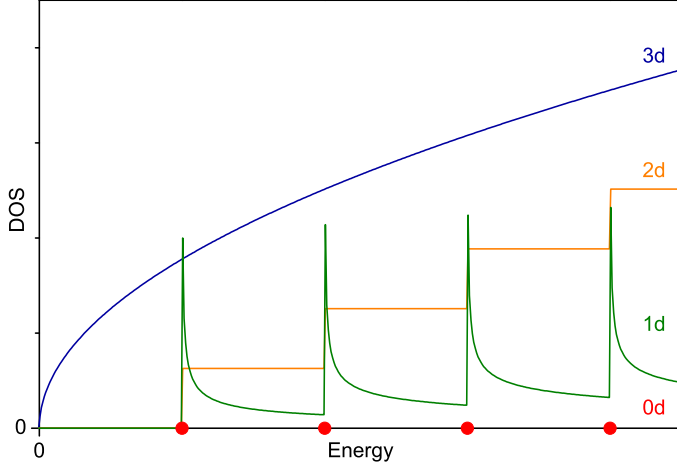


Figure 2.1: Sketch of the density of states in low dimensional systems obtained via eq. (2.3).

$$\begin{aligned}
 \rho_{3d} &\propto \sqrt{E} \\
 \rho_{2d} &= \text{const.} \\
 \rho_{1d} &\propto 1/\sqrt{E - E_n} \\
 \rho_{0d} &\propto \delta(E - E_n) \quad ,
 \end{aligned} \tag{2.3}$$

where E_n denote the eigenvalues of the system. In Fig. 2.1, the resulting DOS is sketched for all dimensions obtained via eq. (2.3). Usually, a finite DOS reflects also a non-vanishing conductance. We will show many correlations between the density of states and the transport. A remarkable feature in one-dimensional systems is the low DOS with superposed sharp peaks with a $E^{-\frac{1}{2}}$ tail, which are responsible for many interesting optical as well as transport properties. We will treat the resulting effects of these so-called van-Hove singularity (vHs) peaks further on.

2.2 Ballistic transport

Depending on the measurement setup, other length scales have to be taken also into account. As we will see further on in section 5.1.2, SWCNTs usually fit into the class of ballistic conductors with quite high mean free paths L_m of the order of μm [35–39]. However, this picture may change when considering high-bias conditions. In Fig. 2.2(a) AFM images of SWCNT devices with varied channel length from μm down to 10nm are shown. The current saturation at high applied voltages indicates the occurrence of phonon-assisted scattering processes, see Fig. 2.2(b). Javey *et al.* obtained for the quasi-ballistic electronic transport a mean free path of acoustical phonon scattering l_{ap} around 300nm and of optical phonons l_{op} around 15nm [34]. They reported that the maximum current values of individual SWCNTs range up to nearly $100\mu\text{A}$, indicating that SWCNTs can withstand current densities as high as $10^9\text{A}/\text{cm}^2$. This current density is about 3 orders of magnitude higher than for common metals such as Al or Cu.

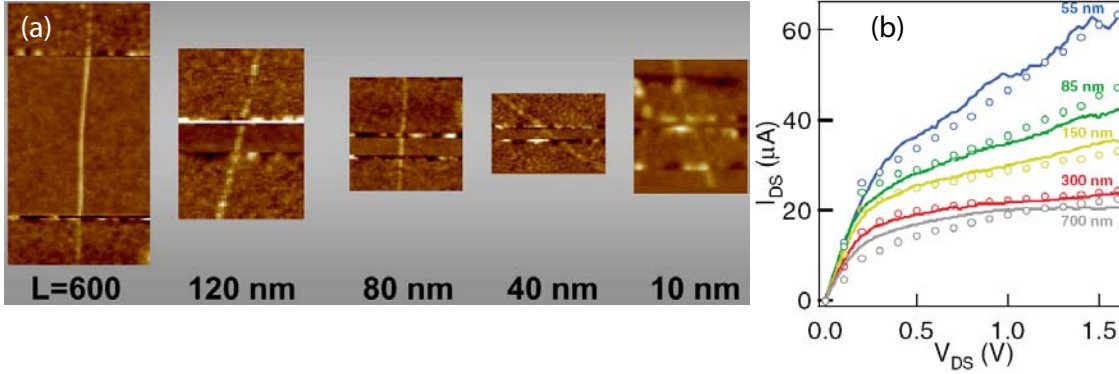


Figure 2.2: (a) SWCNT devices with channel lengths ranging from 10nm to μm . (b) Saturation current of Ohmically contacted devices in function of applied bias. For short channel lengths ($< 100\text{nm}$), the current I_{ds} remains a function of bias V_{ds} . Adapted from [34].

In the low-bias ballistic regime, the transmission probability T through an (ideal) conductor equals unity once the electron enters the system. But if there are no scattering processes, would not the resistance vanish and the conductance diverge? The answer is no. The conductance will reach a maximum of the order of $\Gamma_0 = 2e^2/h$ upon diminishing the dimensions of the device. As we will see further on, no voltage drop occurs inside a ballistic conductor, only at the interfaces at the contacts, even for totally transparent contacts. The Kubo-Greenwood as well as the Landauer-Büttiker formalisms, introduced further on in sec. 5, give us the detailed mathematical description of this phenomena. For system dimensions of the order of the characteristic lengths, the conductance starts to be quantized

$$\Gamma = M\Gamma_0 T \quad , \quad (2.4)$$

where M gives the available transport channels in the conductor and T the transmission coefficient. An ideal lead has an infinite number of channel modes, whereas a (small) conductor only M modes. In the ballistic regime, the contact resistance $R_c = 1/M\Gamma_0 = 13k\Omega/M$ can be explained by a current redistribution at the interfaces required due to this channel mismatch. And, this resistance is far from being neglectable!

2.3 Quantum interference effects in 1-dimensional structures

When two metallic electrodes are deposited on top of a nanostructure, often these mesoscopic probes are invasive, non-identical and not totally transparent: tunnel barriers develop at the contact/nanotube interfaces, leading to the formation of a quantum dots (QD) within the nanotube segment in between the electrodes (\sim

few hundred nm spaced). Even being actually a three-dimensional system, the quantum confinement in all spatial directions lead the formation of discrete energy states. In a finite conductor of length L , the \vec{k} vectors in the longitudinal direction also appear quantized, $k_{||,n} = n \cdot \pi/L$. This leads to an energy level spacing of $\Delta E = \frac{dE}{dk_{||}} \Delta k_{||} = \frac{\hbar v_F}{2L}$, cf. eq. 3.6. Metallic nanotubes have a high Fermi velocity so that this spacing amounts to $\Delta E \sim 1.7eV/L[nm]$. When the thermal energy is smaller than ΔE , this discrete QD spectrum should be observable. Indeed, the short channel length as well as the small diameter of CNTs make it possible to observe the quantum properties at temperatures below $\sim 10K$. As the main part of the theoretical work in chapter 6 is dedicated to the exploration of quantum interference effects, we will now present some of these intriguing effects present in mesoscopic devices.

We can distinguish three quantum regimes depending on the coupling Ξ between the nanotube and the leads. At small device dimensions, the energy $U_c = e^2/C$ required to store an additional electron in the QD may become larger than the thermal energy. C denotes the total capacitance of the device to the macroscopic world and is rather low, around some electrons per Volt per μm [26].

Opaque contacts	$h\Xi \ll U_c$	Coulomb blockade where QD charging effects dominate.
Intermediate	$h\Xi \leq U_c$	Charging and higher-order tunneling processes, e.g. cotunneling and Kondo effect.
Transparent	$U_c \ll h\Xi$	Fabry-Perot interferometer. The nanotube acts as a coherent electron wave guide and quantum interference effects of non-interacting electrons take place.

2.3.1 Coulomb-blockade

When the discrete energy spacing and the contact resistances are large enough, Coulomb-blockade in the transport properties are observed at low temperatures. In this regime, the electronic levels are filled up to the N th level. Due to the low capacitance C , the Coulomb repulsion in nanotubes is quite high (meV) and an onset of Coulomb blockade is expected for $C_{CB} \sim \frac{e^2}{2k_B T}$. In the small bias and low temperature regime, the $N + 1$ th electron cannot enter the dot and the transport is then blocked. Upon varying the gate voltage V_g , the energy levels in the QD can be tuned. Eventually the next available level $N + 1$ gets into the range of the bias window between μ_d and μ_s and a single electron can transmit through the QD. μ_s and μ_d denote the electrochemical potentials of the source and drain electrode, respectively. At these values of V_g we expect a sudden augment of the current, as depicted schematically by the sharp current peaks in Fig. 2.3(a). Another way of lifting the blockade is by changing the bias voltage $V_{ds} = (\mu_s - \mu_d)/e$. For a large

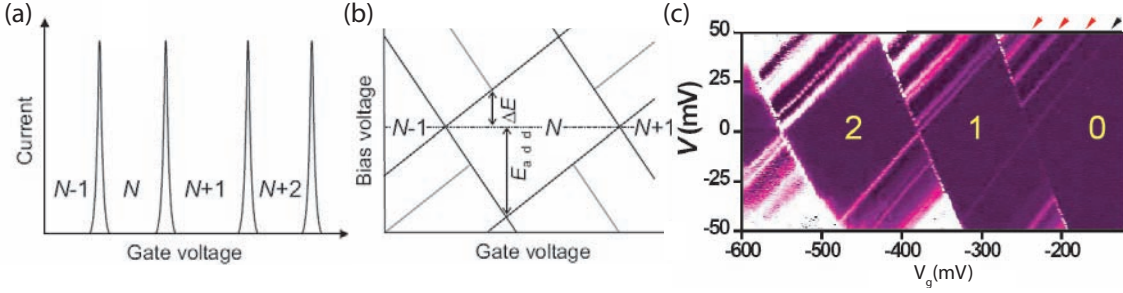


Figure 2.3: *The Coulomb blockade regime. (a) Coulomb peaks appearing in current as a function of V_g . (b) Coulomb diamonds in differential conductance, dI/dV_{ds} , versus V_{ds} and V_g . The edges of the diamond-shaped regions (black) correspond to the onset of the current, i.e. the peaks in (a). Diagonal lines emanating from the diamonds (dashed) indicate the onset of transport through excited states. (c) Two-dimensional conductance color plot, vs. V_{ds} and V_g at $T = 4$ K (dark is zero conductance, bright is $3\mu S$). Adapted from [25].*

enough bias voltage, the QD's charge exceeds $|Q| > e/2$ and tunneling may occur; the threshold voltage (for the ideal case) is given as $V_t = \frac{e}{2C}$. For voltages higher than V_t , the device is in the on-state with a constant conductance. Thus, a complex conductance dependence on both V_{ds} and V_g is expected, as shown in Fig. 2.3(b). In the (diamond-like) center region, the tube is charged with N electrons and no transport occurs. At the edges of the so-called Coulomb diamonds an onset of current is detected, indicated by the black lines. The transport mediated through excited intermediate states are depicted as dashed lines. Actually, Fig. 2.3(a) is a horizontal cut at zero bias of Fig. 2.3(b). An experimental measurement, Fig. 2.3(c), of a small semiconducting SWCNT device ($L \sim 200nm$) evidences all the expected results discussed[25]. The yellow numbers in the Coulomb diamonds give the number of charged holes. The excited intermediate level transitions are indicated by red arrows.

2.3.2 Higher-order tunneling: Cotunneling and Kondo effect

When the contact resistance is reduced, also higher-order beside the sequential tunneling described before may occur. Although we are not going to explore this transport regime in the thesis, we discuss shortly its main effects. Inelastic (elastic) cotunneling takes place in processes where one electron enters the dot, while another electron simultaneously exits the dot, leaving the dot in a (non) excited state. Temporarily, the QD is left in a classically forbidden 'virtual' state[40].

If the electron spin is taken into account, then coherently formed correlated many-electron state events may take place. The spin in a virtual intermediate QD state may be flipped when being replaced by another spin from the metallic reservoir. Many such events combine to produce the Kondo effect, which leads to the appearance of an extra resonance at the Fermi energy. Since the transport

properties are determined by electrons with energies close to the Fermi level, the extra resonance can dramatically change the conductance[24]. The electrons in the two leads are then strongly coupled, allowing current flows even at low temperatures $T < T_K$. The Kondo resonance effect is a theory that describes the scattering of electrons from a localized magnetic impurity below the Kondo temperature T_K [41, 42]. When the number of spins in the dot is odd, resonance tunneling occurs, which is not possible for even numbered spins. The resulting pronounced 'odd-even asymmetry' is detectable in transport measurements[43].

2.3.3 Fabry-Perot interference effects

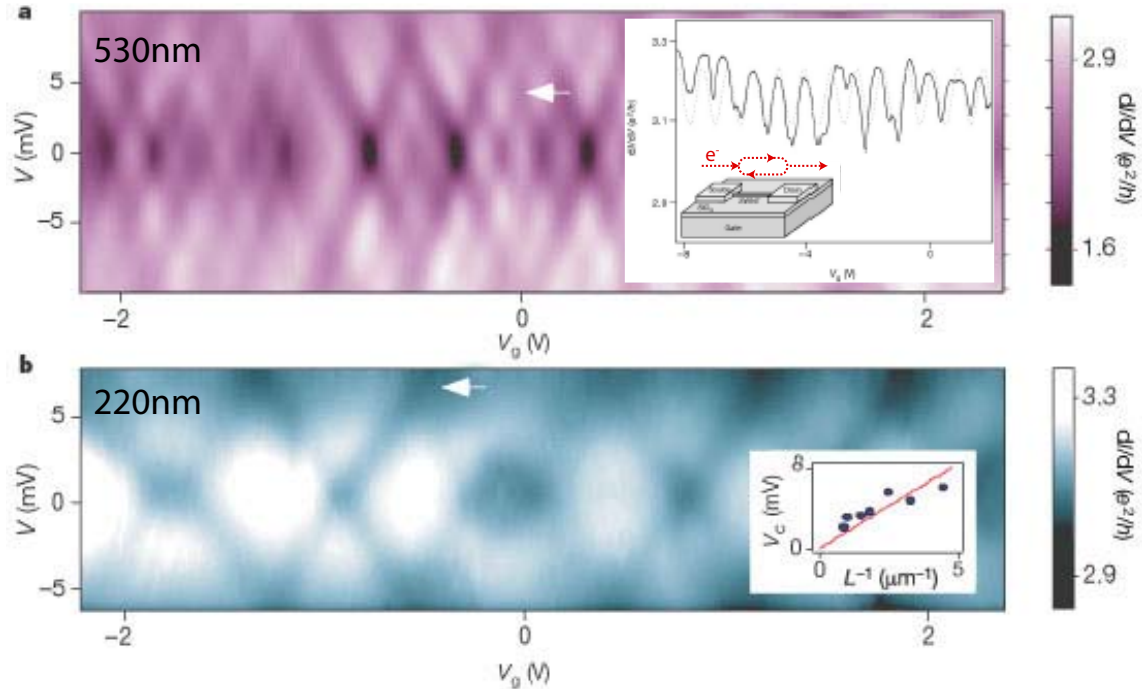


Figure 2.4: Fabry-Perot oscillations at $T=4\text{K}$: Conductance $\delta I_{ds}/\delta V_{ds}$ map as function of V_{ds} and gate voltage V_g . SWCNT device with $L=530\text{nm}$ (a) and 220nm (b) channel length. Insets: a horizontal cut near $V_{ds} = 0$ as well as a device scheme depicting the electron interference path (top). Linear dependence of the first conductance minimum V_c , as indicated by arrows, as function of inverse device length L (bottom). Adapted from [26].

In the regime of transparent contacts, coherent quantum interference effect may be observed. Here, the nanotubes act as coherent waveguides, with the resonant cavity formed in between the contact interfaces. The situation can be compared to the light transmission in an optical Fabry-Perot cavity. The inset of Fig. 2.4(a) depicts the device setup of the QD. Possible electron wave interference paths are indicated by dashed lines. Multiple reflection of the electronic waves can occur, leading to well defined conductance oscillations [see inset of Fig. 2.4(a)]. The pronounced $\delta I/\delta V$

oscillations are quasi-periodic as a function of V_g , which shifts the quantum path's interference phase[26, 27]. The results are very similar to the smooth conductance oscillation, as a function of the Fermi-level, we obtained by the theoretical calculations of zigzag metallic QD; compare with Fig. 6.21. The interference phase can also be modulated by the applied bias. The resulting conductance maps in Fig. 2.4 show a well defined oscillation pattern. The interference period scales with the length L of the device. When comparing the first crossing V_c of destructive interference conductance dips (marked by white arrows), a linear dependence with the inverse of channel length is obtained, $V_c \propto L^{-1}$ [see inset of Fig. 2.4(b)]. This provides an experimental evidence that the scattering processes take place at the metal/nanotube interface, whereas the transport through the SWCNTs remains ballistic[26].

However, to observe those intriguing coherent interference effects, the contacts have to be nearly perfect Ohmic. This requires state-of-the art device fabrication. Nevertheless, just a few devices out of a batch of many prepared samples show conductance values close to the theoretical maximum value of $2\Gamma_0$. We will now have a further insight into the contact/nanotube interface region.

2.4 The contact barrier problem

It took nearly a decade until SWCNTs could be reliably contacted by transparent lead interfaces. The challenging device fabrication as well as the right choice of the contact metal play the mayor role to achieve near-perfect Ohmic leads. The interaction between nanotube and metal will also be important for proper contact formation. Several different metals were utilized, such as Au, Pd or Ti. In the latter case, an additional high temperature annealing step is required to mediate the transport through covalent Ti_xC [44]. It turned out that Pd worked best to obtain reproducible small contact resistances[39, 45]. It should be stressed out, that in most cases a thin adherence layer of usually $5nm$ Cr under the contact material is needed to ensure a successful lift-off during device processing.

2.4.1 Schottky barrier formation

Already back in 1998 it was experimentally demonstrated that semiconducting SWCNTs can act as field effect transistors (CNTFET)[46, 47]. When a semiconductor is brought into contact with a metal, charge transfer near the interface region will occur to align the Fermi levels of both materials. A depletion region will form in the semiconductor leading to rectifying behaviors equivalent to the well-known diodes. The situation before the two materials are brought in contact is shown in Fig. 2.5(a). The Fermi level E_F lies in between the valence E_v and conductance E_c band edge. After contact is established, electrons will enter the p-type SWCNT and the joined system in equilibrium will have an aligned Fermi level, as schematized in Fig. 2.5(b). The resulting barrier will hinder the electronic transport.

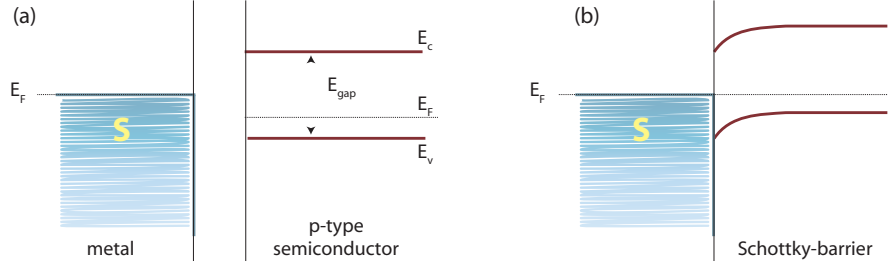


Figure 2.5: Formation of a Schottky barrier at the interface between a metal and a p-type semiconductor with gap $E_{gap} = E_c - E_v$. (a) Before getting into contact the Fermi levels E_F of both systems are not aligned. (b) Depletion zone in the semiconductor near the interface is created upon contacting and a Schottky barrier is formed in the semiconductor.

Many experimental results evidence the formation of a Schottky barrier (SB) at the interfaces between the metallic leads and semiconducting SWCNTs[48, 49]. Conductive AFM scans indicate the scattering centers to be localized at the SB interfaces [50]. The asymmetry of current/voltage curves and different saturation currents cannot be explained by the common channel-pinching in metal-oxide field effect transistors (MOSFET). Another hint for the gating action on the interface rather than on the bulk SWCNT is the temperature dependence of the inverse subthreshold slope $S = dV_g/d(\log I_{ds})$. Whereas in MOSFET it is expected to depend linearly on the temperature, CNTFET does not show any dependency under $T = 200K$ [48]. For high switching rates of the SWCNT device, characterized by S , much efforts have been done to minimize the contact barrier. The total on-resistance of a SWCNT transistor will be the sum of contact resistances at the electrodes and of the nanotube itself. The reduction of the resistances is important to reduce power dissipation, increase the on-currents, and decrease the delay τ of the transistor ($\tau \sim RC_g$, where R is the on-resistance at saturation and C_g the gate capacitance). To reduce the resistance of the contacts one has to find an appropriate contact metal, whereas to minimize the resistance of the nanotube, ballistic transport of the carriers within the tube is necessary. The height of the Schottky barrier depends largely on the diameter of the SWCNTs as well as the fabrication process and the choice of the contact metal[39, 45, 51]; e.g. the work functions of palladium or rhodium ($\Phi \sim 5eV$) are similar to the one of larger diameter semiconducting SWCNTs ($\Phi_{CNT} \sim 4.7eV$)[52], providing reliable transparent contacts.

Usually, as-processed semiconducting SWCNTs show p-type characteristics when measured in air. This behavior is attributed to a shift of the Fermi level towards the valence band by the presence of adsorbed oxygen, a modulation of Schottky barriers due to the introduction of oxygen into the interface region or charge transfer from metal electrons into the SWCNT device[48, 53, 54]. The p-type characteristics can be changed to bipolar or n-type by removing the adsorbed oxygen through heating or high current modulation in vacuum. This transition is reverted once the devices are again exposed to oxygen.

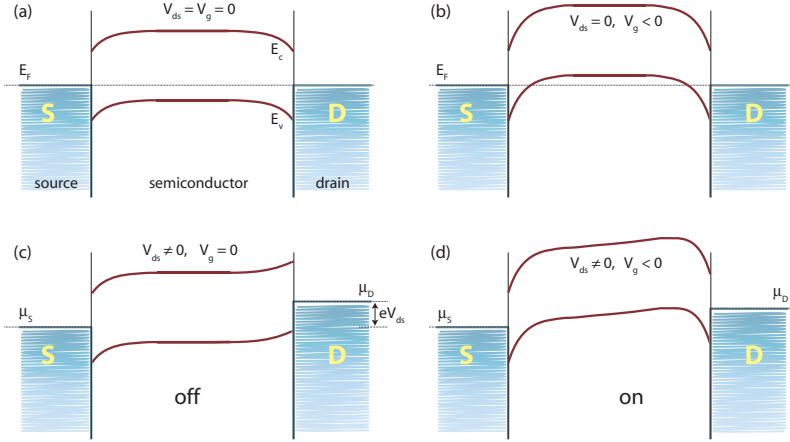


Figure 2.6: Basic operation of a Schottky barrier with the gate acting along the entire length of a p-type semiconducting SWCNT. At $V_g = 0$, no tunneling of the holes is possible (a), whereas a negative voltage turns the Schottky barrier more transparent (b). Upon applying a bias voltage $V_{ds} = e(\mu_d - \mu_s)$, the off and on states, for V_g higher than the threshold voltage, are depicted in (c) and (d), respectively.

The Schottky barrier will block the conductance through the system. The situation of inhibited transport is depicted in Fig. 2.6(a). At low bias V_{ds} , the current from source to drain remains still blocked by the barrier at the source interface, see Fig. 2.6(c). However, the effective barrier thickness and thus the tunneling probability through the SB can be modulated by both V_g and V_{ds} fields. Tunneling of holes become possible at voltages higher than the threshold voltage V_{th} , as shown in Fig. 2.6(b). The on-state of the CNTFET for $V_g > V_{th}$ and higher bias is observed in Fig. 2.6(d). The bulk part of the SWCNT, represented by the region with linear band dispersion in the central part of the QD, is not directly involved in affecting the switching behavior of a CNTFET exhibiting a SB.

However, initially contradicting results were reported concerning the nature of the transistor action. Whereas some papers reported that the current is modulated by varying the channel (SWCNT) conductance[46, 47], others indicate a modulation solely of the Schottky barrier height[48, 49]. Other experimental results evidence the influence of both the SWCNT bulk and the contact barrier height[36, 55]. They fabricated a long nanotube device with a series of individual addressable gates. The ones close to the SWCNT indicate a bulk switching, whereas the ones near the contact electrodes hint at a barrier height modulation[36]. Nevertheless, to access the fascinating properties of CNTFET, the main efforts have to be driven into the barrier height reduction in order to obtain an improved transistor behavior.

3 Basics of Carbon Nanotubes

Carbon is the only element which appears in many different allotropes in all possible dimensions: graphite (3d), graphene (2d), carbon nanotubes (1d), and fullerenes (0d). As we will see, we can encounter metallic, semiconducting or insulating properties in the world built by carbon. To understand their rich properties we present in this chapter some basics of carbon structures and carbon nanotubes in particular.

3.1 Hybridization

Due to atomic orbital hybridization, carbon can present diverse electronic configurations. Meanwhile the two $1s^2$ core electrons are strongly localized and only show minor influence on the electronic properties, the orbitals of the four valence electrons $2s$ e $2p$ can mix quite easily. The energy separation between these two orbitals is small compared to the binding energy, raising the appearance of varied hybridizations sp^n , with n ranging from one to three. For example, in the sp^2 hybridization two $2p$ orbitals appear mixed with the $2s$ orbital. Usually these three σ electrons form trigonal strong bindings with the neighbor atoms meanwhile the forth, weakly bounded electron perpendicular to the trigonal plane is responsible for the mayor electronic effects of the material[56].

3.2 Basics of Graphene

3.2.1 Crystallographic structure of graphene

Carbon nanotubes are new forms of carbon-based sp^2 material and may be idealized as rolled-up graphene sheets. In order to understand the properties of CNTs, we first have to gain insights into the properties of graphene sheets. The weekly bounded graphene layers compound the three-dimensional graphite, where the interplane distance (3.35\AA) is much greater than the intraplane C-C atomic distance (1.42\AA). Thus, the electronic properties of both graphite and CNTs can be well approximated by those of graphene. Very recently, in 2004, it could be demonstrated, that planar graphene exists in the free state and that single graphene sheets could be integrated into electronic devices[57, 58]. Currently, graphene is under intense

research[58]. Graphene is composed of a hexagonal carbon lattice where each carbon atom is covalently bounded by the molecular orbitals sp^2 to its three neighbor atoms. Fig. 3.1(a) depicts a graphene sheet, with the π electron perpendicular to it

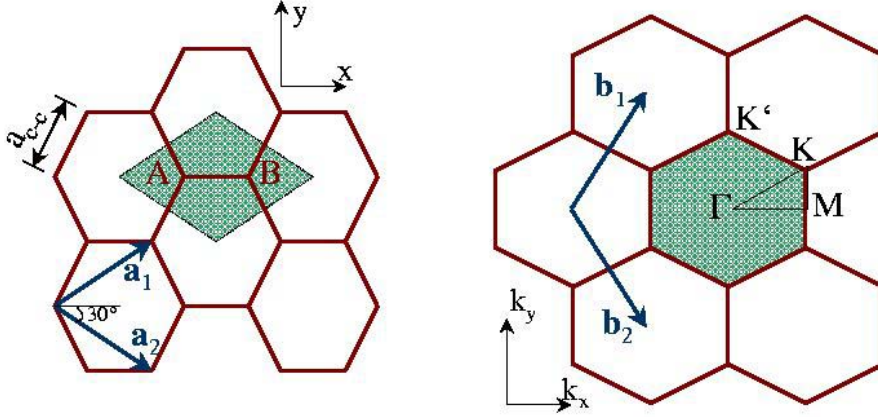


Figure 3.1: Graphene honeycomb lattice, primitive vectors and unit cell in (a) real space and (b) reciprocal space. The unit cell contains two carbon atoms (A and B) belonging to the two sublattices. High symmetry points (Γ , K, M) are also depicted.

and Fig. 3.1(b) the reciprocal lattice. The unit cell and the first Brillouin zone are shown in green. The real space honeycomb lattice with a two atom basis (A and B) is spanned by the primitive vectors

$$\vec{a}_1 = \left(\frac{\sqrt{3}}{2}a, \frac{a}{2} \right), \quad \vec{a}_2 = \left(\frac{\sqrt{3}}{2}a, -\frac{a}{2} \right), \quad (3.1)$$

where $a = |\vec{a}_1| = |\vec{a}_2| = a_{cc}\sqrt{3} = 2.46\text{\AA}$ is the lattice constant. The next-neighbor distance a_{cc} is around 1.42\AA .

3.2.2 Electronic structure of graphene

The electronic structure may be obtained, in a first approximation, by considering only the contributions of the nearest neighbors. As base functions to generate the graphite lattice we use an expansion in localized Bloch functions:

$$\phi_j = \frac{1}{\sqrt{l}} \sum_{\vec{R}} e^{i\vec{k}\cdot\vec{R}} \psi_j(\vec{r} - \vec{R}) \quad (j = A, B) \quad , \quad (3.2)$$

with A and B being the two non-equivalent carbon atoms of the lattice. In this tight-binding model, the σ electrons form covalent bonds whereas the π electron can easily hop 'along' these bonds between the atomic sites A and B. The hopping parameter γ_0 can be expressed as

$$\gamma_0 = \langle \phi_A(r) | H | \phi_B(r - a_{cc}) \rangle \quad , \quad (3.3)$$

and its value is reported around -2.7eV [59]. Thus, the hopping matrix element $H_{AB} = H_{BA}^*$ is given by $H_{AB} = \gamma_0 f(k)$ with

$$f(k) = e^{ik_x a/\sqrt{3}} + 2e^{-ik_x a/2\sqrt{3}} \cos\left(\frac{k_y a}{2}\right) . \quad (3.4)$$

Solving the secular equation $\det(H - ES) = 0$, two energy eigenvalues are obtained

$$E_{g2D}^\pm(\vec{k}) = \frac{\epsilon_{2p} \pm \gamma_0 \omega(\vec{k})}{1 \pm s\omega(\vec{k})} , \quad (3.5)$$

where the signal $+$ ($-$) denotes the bonding π (anti-bonding π^*) energy bands. The overlap integral is given by $s = \langle \phi_A(r - R) | \phi_B(r - R - a_{cc}) \rangle$, and $\omega = \sqrt{|f|^2}$. Considering $s=0$, the energy dispersion relation reads then

$$E_{g2D}^\pm(k_x, k_y) = \pm \gamma_0 \sqrt{1 + 4\cos\left(\frac{\sqrt{3}k_x a}{2}\right) \cos\left(\frac{k_y a}{2}\right) + 4\cos^2\left(\frac{k_y a}{2}\right)} . \quad (3.6)$$

The energy dispersion of the first Brillouin zone is shown in Fig. 3.2. The valence

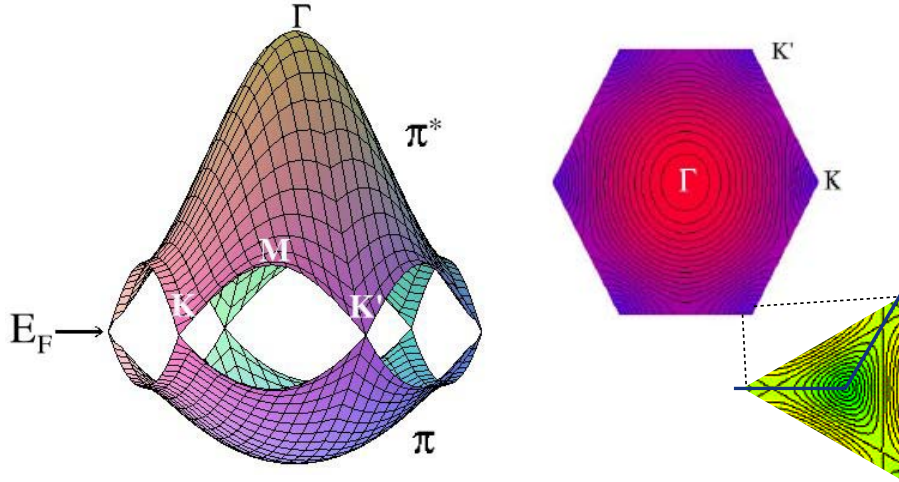


Figure 3.2: Energy dispersion of a graphene sheet for a non-vanishing overlap integral s . Left panel shows the bonding π and anti-bonding π^* bands as well as the six touching points at the Fermi level E_F . Top view of π^* -electrons visualize in right panel the conical shape of the band structure near $E_F = 0$. Zoom in around the K' point demonstrate the trigonal warping effect.

and the conduction band are all separated apart from the six vertexes and the Fermi surface of graphene (Fermi energy $E_F = 0$) shrinks to a point. However, at these touching points, which in fact are two non-equal points K and K' , the density of states is zero. The graphene sheet is thus called a zero-gap semiconductor. As shown in more detail in the right panel, the band structure near the Fermi-level consists of six cones with a linear dispersion[56]. The linearity of the dispersion relation indicates that the effective masses of electrons and holes are zero. The vanishing of

the effective mass signifies that there is no interaction between electrons, holes and the graphene lattice, so that electrons propagate ballistically through graphene with the velocity $v_{E_F} \approx c/300$, where c is the speed of light.

3.3 Basics of SWCNTs

3.3.1 Real space description of the SWCNT crystal structure

Although SWCNTs are not actually synthesized in this way, the easiest way to visualize the crystallographic structure is a graphene sheet rolled up in a cylindrical form such that its structure can be considered as *unidimensional*.

Chiral vector $\vec{C} = (n, m)$

In general, the tube exhibits a spiral form, called chirality, with axial symmetry. As will be shown in this section, all important variables can be derived from this single vector, also called chiral or *Hamada* vector. In Fig. 3.3 a rectangular section of a

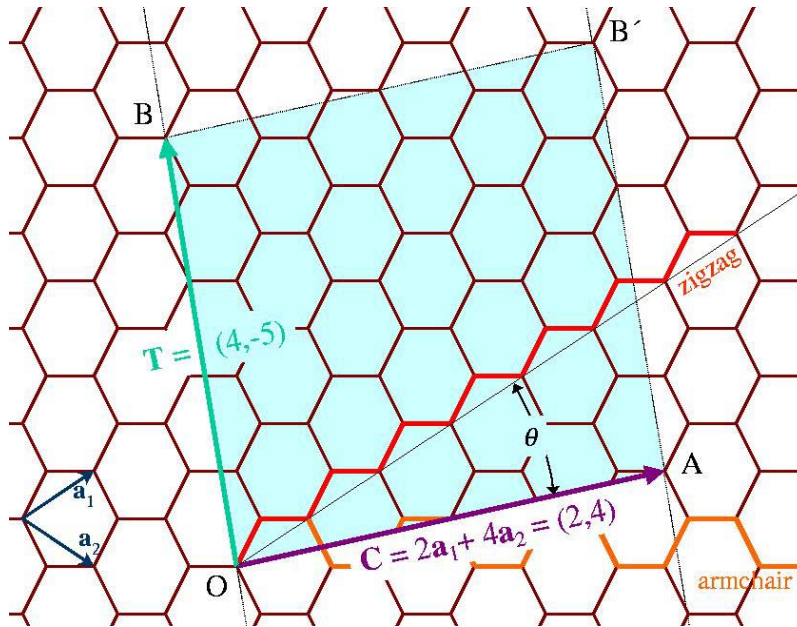


Figure 3.3: Schematic honeycomb lattice with rectangular blueish section to tinker a SWCNT. Connecting sites A and B rolls up the chiral tube with the circumference $\vec{C} = (4, 2)$, translational vector $\vec{T} = (4, -5)$ and number of hexagons $N = 28$.

graphene sheet is shown. The circumference \vec{OA} defines the Hamada vector \vec{C} in terms of the primitive vectors as

$$\vec{C} = n\vec{a}_1 + m\vec{a}_2 =: (n, m) \quad . \quad (3.7)$$

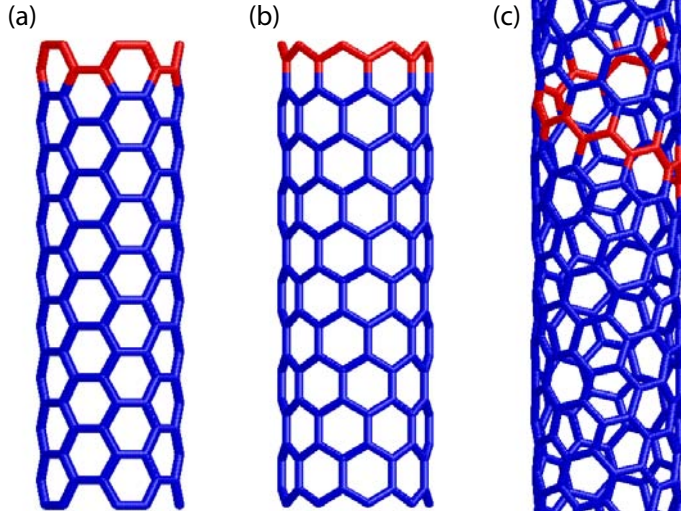


Figure 3.4: Schematic atomic configurations of SWCNTs with different chiralities. The atoms along the Hamada vector \vec{C}_h are highlighted with red colors. A (5,5) armchair tube (a), a (9,0) zigzag tube (b) and a general case, a (10,5) chiral tube (c).

The SWCNT is 'rolled-up' so that the equivalent atoms O and A (as well as B and B') coincide. The translational vector T along the tube axis is also depicted in the figure and is given by

$$\vec{T} = (t_1, t_2) = \left(\frac{3m+n}{d_R}, -\frac{2n-m}{d_R} \right) , \quad (3.8)$$

where d_R denotes the greatest common divisor $d_R = \text{gcd}(2n+m, 2m+n)$. The diameter d_t of the as-built tube can be expressed by the length of the Hamada vector

$$d_t = |\vec{C}|/\pi = \sqrt{n^2 + m^2 + nm} \cdot a/\pi . \quad (3.9)$$

Due to the hexagonal symmetry of the honeycomb lattice, the values of the chiral angle θ are in the range 0° and 30° . Two special roll-up angles are identified in the figure as having a zigzag ($\theta = 30^\circ$) and armchair ($\theta = 0^\circ$) shape. These two angles, forming the so called achiral tubes, are of special interest among the theoreticians due to the resulting, very simple structure, maintaining the symmetry plane perpendicular to the tube axis.

The number N of hexagons in the tube unit cell shown as the blue rectangle in Fig. 3.3 is given by the area spanned by \vec{C} and \vec{T} divided by the area of a hexagon

$$N = \frac{|\vec{C} \times \vec{T}|}{|\vec{a}_1 \times \vec{a}_2|} = \frac{4(n^2 + m^2 + nm)}{d_R} . \quad (3.10)$$

Due to the two-point basis, there are $2N$ carbon atoms in the unit cell. The atomic configurations of the three tube types are schematized in Fig. 3.4. In general, SWCNTs are expressed in terms of the two integers n and m and called:

- **armchair** (n,n) for $\theta = 0^\circ$, $d_t = \sqrt{3}na/\pi$, $N = 2n$
- **zigzag** (n,0) for $\theta = 30^\circ$, $d_t = na/\pi$, $N = 2n$
- **chiral** (n,m) in all other cases.

As the zigzag tubes can be either metallic or semiconducting, we will use in this thesis only the zigzag type to explore e.g. Fabry-Perot-like interferometric properties as well as semiconducting tunnel barriers.

3.3.2 Reciprocal lattice of SWCNT

The reciprocal lattice, spanned by K_i , is defined by the relation $\vec{R}_i \cdot \vec{K}_j = 2\pi\delta_{ij}$. The first Brillouin zone of SWCNTs is thus expressed by the chiral \vec{C} and translational vector \vec{T} as

$$\vec{C} \cdot \vec{K}_1 = 2\pi, \quad \vec{C} \cdot \vec{K}_2 = 0, \quad \vec{T} \cdot \vec{K}_1 = 0, \quad \vec{T} \cdot \vec{K}_2 = 2\pi \quad .$$

Using the given definitions (eq. (3.7), 3.8) of the real space lattice vectors, the primitive vectors of the SWCNT reciprocal lattice are given by

$$\vec{K}_1 = (-t_2\vec{b}_1 + t_1\vec{b}_2)/N, \quad \vec{K}_2 = (m\vec{b}_1 - n\vec{b}_2)/N \quad . \quad (3.11)$$

Due to the finite number of carbon atoms along the circumference, the reciprocal axis \vec{K}_1 results discretized whereas the other axis \vec{K}_2 remains continuous for an infinite long SWCNT. The resulting Brillouin zone is now a system of parallel lines with a

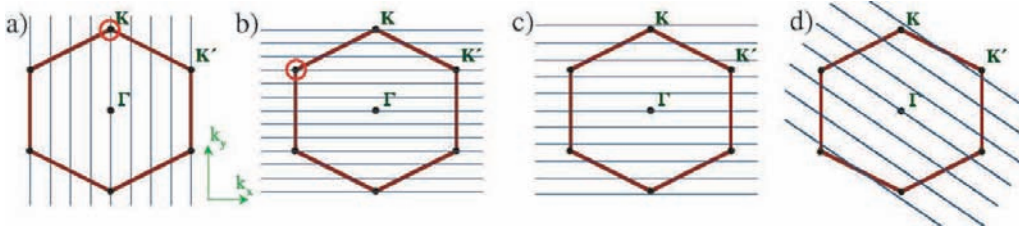


Figure 3.5: Lines of allowed \vec{k} vectors of the following SWCNTs overlaid on the graphene sheet Brillouin zone: (4,4) metallic armchair (a), (9,0) metallic zigzag (b) and (10,0) semiconducting zigzag (c) as well as a chiral semiconducting SWCNT (d).

spacing of $|\vec{K}_1|$ and a length of $|\vec{K}_2| = 2\pi/|\vec{T}|$. The reciprocal lattice of four different SWCNTs based on the graphene first Brillouin zone is depicted in Fig. 3.5. Two points in the reciprocal space which differ by $N\vec{K}_1 = (-t_2\vec{b}_1 + t_1\vec{b}_2)$ are equivalent. $N\vec{K}_1$ corresponds to a translation vector of the graphene reciprocal lattice, whereas all the other vectors $q\vec{K}_1$, with $q = 1, \dots, N-1$ are not equal because t_1 and t_2 don't have a common divisor except unity. The SWCNT reciprocal lattice vector can be expressed as

$$\vec{k} = \left(\mu \frac{\vec{K}_2}{|\vec{K}_2|} + q\vec{K}_1\right), \quad q = 0, \dots, N, \quad \text{and} \quad -\frac{\pi}{T} < \mu < \frac{\pi}{T} \quad . \quad (3.12)$$

3.3.3 Electronic band structure of SWCNTs

The electronic properties of SWCNTs can be easily derived from those of graphite. As seen previously, the periodic boundary conditions along the tube circumference permit only discrete wave vectors. Thus, the SWCNT energy dispersion consists of N one-dimensional energy bands and is obtained by cutting the two-dimensional graphene energy dispersion at the lines \vec{k} fulfilling the condition of eq. (3.12). The so-called zone foldings yields

$$E_{SWCN}(\vec{k}) = E_{g2D}\left(\mu \frac{\vec{K}_2}{|\vec{K}_2|} + q\vec{K}_1\right) . \quad (3.13)$$

The positions and directions of the cutting lines uniquely depend on the chirality (n, m) of the tube. Thus, we may expect that SWCNTs with different chiralities have also different energy bands. Remembering the graphene energy dispersion in Fig. 3.2, there are only two points, the vertexes K and K' , where the valence and conduction bands are in touch. If now a SWCNT cutting line crosses one of the vertexes this results in a metallic tube. If not, a gap appears in the band structure, i.e. the tube has semiconducting behavior. Simple geometrical zone-folding considerations gives the condition of a tube being metallic by

$$2n + m = 3\aleph \quad , \quad (3.14)$$

with \aleph being an integer[56]. As n and m are independent parameters, we expect that approximately one third of the tubes are metallic which indeed is verified experimentally in as-grown SWCNT samples. In Fig. 3.5 we can further identify that due to the symmetry at the Γ -point all armchair (n, n) tubes are metallic. Zigzag $(n, 0)$ tubes are metallic, according to eq. (3.14), if n is divisible by 3. In fact, in Fig. 3.5(b), \vec{K} hits a vertex in the case of the metallic zigzag $(9, 0)$, highlighted by the red circle. On the other hand, there is no vector crossing the vertexes of the semiconducting zigzag $(8, 0)$ in 3.5(c) or the chiral tube in 3.5(d).

Taking into account the curvature of the tube, a small band gap of around tenths of meV is obtained for supposed metallic nanotubes. The curvature reduces the overlap of the π orbitals leading to a small dislocation of the \vec{K} vector which now misses the vertex[60, 61]. These tubes are also called semi-metallic. Nevertheless, this is not the case for armchair tubes always having a metallic behavior. For tubes with diameters bigger than $\approx 1nm$, these corrections of the simple tight-binding model are normally discarded.

Applying the boundary conditions (eq. (3.13)) we now obtain the band structure of achiral SWCNTs. In armchair tubes, Fig. 3.5(a), the k_x axis appears quantized as $\sqrt{3}nk_x a = 2\pi q$, with $q = 1, \dots, 2n$. Whereas in zigzag tubes, Fig. 3.5(b-c), the quantized k_y writes $nk_y a = 2\pi q$, with $q = 1, \dots, 2n$. The energy dispersion relations of three achiral SWCNTs are depicted in Fig. 3.6. Energies are given in units of the hopping parameter γ_0 and blue bands are double degenerated. As stated already

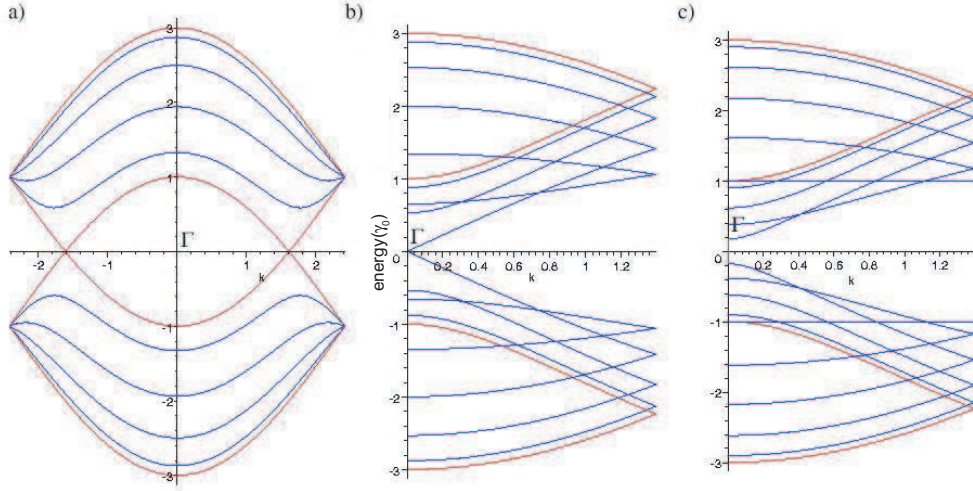


Figure 3.6: Energy dispersion of SWCNTs. (a) Armchair (5,5), (b) zigzag (9,0), and (c) zigzag (10,0). The metallic tubes (5,5) and (9,0) show a band crossing $E_F = 0$ at $ka = \pm 2\pi/3$ and $k = 0$, respectively. Blue bands are double degenerated, red bands are non degenerated.

before, in the case of the (5,5) armchair tube (a), there are two non degenerated bands crossing the Fermi level $E_F = \epsilon_{2p} = 0$, demonstrating the metallic state. The metallic (9,0) zigzag tube, Fig. 3.6(b), has one double degenerated band crossing the Fermi level, whereas in the band structure of the semiconducting (10,0) tube, Fig. 3.6(c), appears a gap of around $0.4\gamma_0$.

Density of states of SWCNTs

The LDOS and energy dispersion of some achiral SWCNTs is depicted in Fig. 3.7. As easily can be seen, at each extrema, the derivative will yield zero and therefore, the inverse will diverge. These spikes in the LDOS, also called van Hove singularities (vHs) are typical traces of one-dimensional systems. As expected, the metallic tubes in Fig. 3.7(a-b) have a finite LDOS plateau at $E_F = 0$ whereas the semiconducting tube in Fig. 3.7(c) gives a gap with zero LDOS.

The high density of states at these spikes leads to enhanced optical transitions between the vHs and thus, the relation between transition energy and diameter is crucial for the optical investigation of SWCNTs by e.g. optical absorption or Raman spectroscopy. These transition energies scale with the inverse of the diameter and are given in the tight-binding approximation as

$$E_{ii} = i \cdot 2\gamma_0 a_{c-c} / d_t \quad , \quad (3.15)$$

where those transitions where i is divisible by 3 belong to metallic tubes, the others to semiconducting tubes. Thus, the width of the metallic plateau is given by $E_{plateau}^m = 6\gamma_0 a_{c-c} / d_t$ and the semiconducting gap by $E_{gap}^{sc} = 2\gamma_0 a_{c-c} / d_t$. A typ-

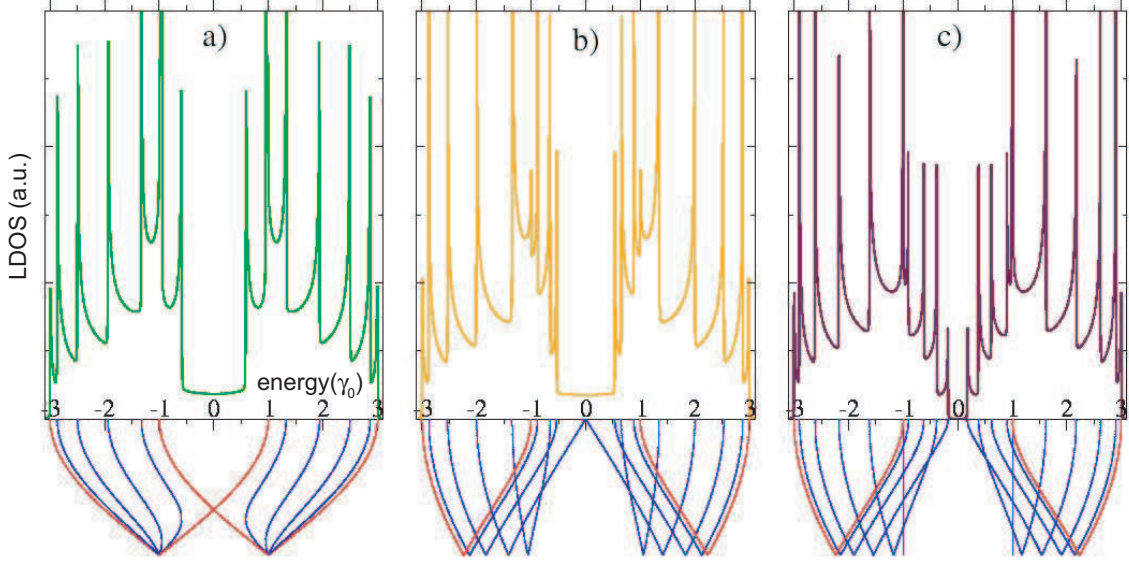


Figure 3.7: LDOS of achiral SWCNTs. (a) Armchair (5,5), (b) zigzag (9,0), and (c) zigzag (10,0), calculated with eq. 5.6. For comparison, the energy dispersion relations are depicted in the lower panel.

ical semiconducting nanotube of 1.4nm has a gap around 0.5eV. Using eq. (3.9), the formula for the semiconducting zigzag tube gap reads $E_{gap}^{zz} = 2\gamma_0\pi/\sqrt{3}/n \approx 9.65eV/n$. Near the Fermi level, all metallic tubes have a linear energy dispersion with $E(\vec{k}) = \pm\gamma_0k\sqrt{3}a/2$, which gives a constant LDOS plateau independent of tube chirality or diameter.

For more sophisticated theoretical simulations or experiments, like the (n, m) chirality assignments of individual peaks in Raman or photoluminescence spectroscopy, a calculation model more accurate than the simple π -band tight-binding picture adopted in eq. (3.15) is needed. It can be achieved e.g. by third-neighbor tight-binding[59], *ab initio* calculations, or by a symmetry-adapted non-orthogonal tight-binding model including $\sigma - \pi$ hybridizations[62–64]. The additional contributions may be included, for instance, by replacing the single value hopping parameter by a 4×4 matrix. These results are commonly joined and illustrated in the so-called Kataura plot[65]. Considerable refinements occur as a result of the trigonal warping effect[66] and the curvature effects. They are more pronounced for smaller tube diameters ($\lesssim 1nm$). However, the tubes used in the experimental section of this thesis are substantially bigger, so that the simple model can be used to adequately describe the quantitative properties of the samples. In the theoretical section we will also use tubes of smaller diameters due to less computational time. Nevertheless, the theoretical dependencies of the geometrical configuration presented here have no ambitions to furnish quantities measurable in experiment. They are qualitative physical properties of the systems investigated and will hold also for larger tubes of the same type.

4 Device fabrication

Since the rise of carbon nanotubes, the main efforts worldwide were directed towards the implementation into semiconducting electronic devices as the future materials. The fact of being mechanically very stable and tough, together with high carrier mobilities, equivalent to that of good metals, indicates a profitable usage of CNTs in nanosized devices as interconnects. The nanoscale dimensions of these structures should allow faster switching rates at lower energy costs for the next generation computers. Superb field effect transistor behavior is expected with the advantage of a well defined and sharp tip end. Furthermore, the ballistic properties of metallic nanotubes address directly the possibility of their usage as energy dissipative-free metal wires. For these purposes, a reliable contacting process is desired with as less as possible transport alteration due to the metallic contacts. Thus, the realization of transport measurements on individual nano-objects requires quite challenging advanced technological steps in order to obtain reliable transparent contacts from the outer world to the investigated structure.

Very fast, but single-use contacts can be obtained by approaching a sharp tip towards another with nanotubes attached under the observation in a scanning electron (SEM) or transmission electron microscope (TEM). There exists two main approaches of four terminal device fabrication. The first requires a very precise placement or synthesis onto pre-defined contacts. Usually the interaction area between the nanostructures and the underlying metal is rather small and in most cases, a post-placement treatment is needed to reduce the contact resistance by, e.g. heat treatment[44], electroless[10] or even anew patterned metal deposition. The second approach is by placing the metal contacts on top of the structures. This can be realized by controlled deposition of e.g. platinum by splitting an organometallic compound ($C_9H_{16}Pt$) in a focused ion beam (FIB) microscope as well as by photo- or electron beam lithography (EBL).

As the main part of the experimental work of this thesis was dedicated to the SWCNT synthesis as well as to the setup and improvement of a new e-beam lithography system at the IFW, I will first introduce with more details the contact fabrication process. Several very different issues have to be addressed for a successful device fabrication. We will start with the topic addressing the placement of the nanotubes on the substrate and (precise) positioning relative to finder alignment markers, followed by an overview over the different synthesis processes available for CNT growth. Then we will discuss the main results of the chemical vapor deposition (CVD) growth process we employed to obtain reliable CNT devices and finish with a detailed description of the contacting lithography step.

4.1 Placement of nanotubes

The precise placement of nanotubes is one of the challenging tasks for a successful integration of these intriguing structures into electronic circuits. Basically, there are two approaches: first, direct growth at predefined positions via patterned CVD synthesis and second, post-production assembly of nanotubes dispersed in liquids. Both methods have advantages and disadvantages.

- **Post-synthesis assembly:** The biggest advantage of post-growth assembly is that any kind of nanotube can be deposited on the substrate. Thus, good-quality laser ablation tubes, chemically functionalized CNTs, non-carbon NTs, or filled CNTs (e.g. with fullerenes[67], endohedral fullerenes[68, 69], pentacene and metallic wires[70, 71]) can be deposited. The major challenge is to break the SWCNT bundles into individual, isolated nanotubes. This can be and is widely done by the use of solvents, ultrasonic treatment and ultracentrifugation which cause contamination and cutting of the tubes. Other approaches include the insertion of wrapping agents which form micelles around the tube and are capable to break up the bundles, e.g. sodium dodecylsulfate (SDS), dodecylbenzene sulphonate (SDBS), sodium cholate[72], or single-stranded DNA[73]. Up to some degree they are able to separate them by their metallic state. Spontaneous dissolution of SWCNTs in polar organic solvents was observed using alkali metals to form polyelectrolyte salts[74]. Directional deposition is achieved by adequate surface functionalization or strong ac-electric fields in liquids[8, 75]. The tendency of bundle formation, deposition of liquid residues as well as synthesis by-products, and the damage caused by the post-growth purification processes are the main disadvantages of this method.
- **Patterned growth:** Micrometer-sized “Petri-dishes” as recipients in a resist structure are patterned on top of an adequate substrate by means of electron beam or optical lithography. Nearly arbitrary catalysts either in solution[76, 77] or by metal evaporation[78] can be deposited in these Petri-dishes. After the lift-off process, the catalyst particles are left on the desired positions ready for the synthesis. Still the controlled directional growths remains challenging, although some degree of control was reported by growth in strong gas flows[79, 80] and electric fields[81, 82]. This method result in very clean samples and no purification has to be done. To obtain individual SWCNTs, the synthesis parameter have to be adjusted to low yield samples. Due to the straight forward and precise positioning capabilities, we will use this method, whenever possible, throughout this thesis.

4.2 Imaging and precise positioning of the structures

Depending on the size of the structure to contact, different means of visualizing the nano-objects can be employed. Normally, the structures are deposited on flat, heavily doped silicon wafers with a thermally grown silicon oxide (SiO_x) layer (100-1000nm). For bigger structures such as MWCNT or VO_x nanoscrolls, both measuring around 50-100nm in diameter, normal optical microscopy in bright or dark-field can be used. The optical

microscope (Zeiss) with 1000x magnification is even able to determine the precise position of individual MnO_2 nanotubes ($d \sim 10 - 20\text{nm}$). Depending on the SiO_x thickness (295nm), a single layer of graphene, a sheet consisting of only one atom thickness, can be observed in the optical microscope. The positions of the structures are then measured with respect to pre-patterned alignment markers made by optical or e-beam lithography, as demonstrated in Fig. 4.1(a). It is worth mentioning that the optical microscope precision is not the highest one but sufficient to contact the rather long nanotubes. After the precise positioning, the electrodes are designed in the EBL patterning CAD software, as depicted in Fig. 4.1(b). An atomic force microscopy (AFM) image of the ready working device is shown in Fig. 4.1(c).

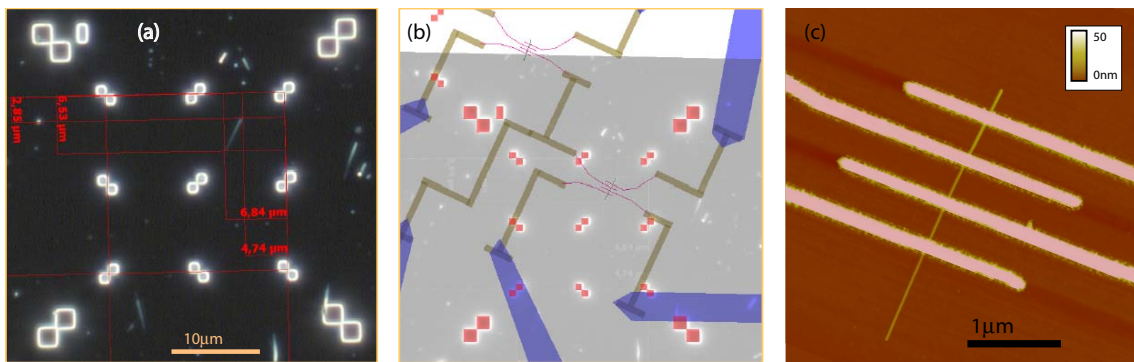


Figure 4.1: Positioning procedure: (a) Optical dark-field micrograph determines the position of the tubes - in this case an individual MnO_2 tube. (b) Four-terminal device layout is designed in the patterning software. The positioning image, shown in gray, can be underlaid for an easier layout design. (c) Topographic AFM image of the ready device with the electrodes on top of the 20nm thick MnO_2 tube.

A more precise positioning can be achieved by using AFM. A cantilever in contact or tapping mode scans the surface and the deviation of a laser spot reflected by the tip is kept constant. Thus, topographic and other informations, such as phase shift, friction or even the conductance and the magnetic stray field can be obtained with a spatial resolution around several tenths of nm . Very clean and flat surfaces are required to distinguish SWCNTs ($\sim 1\text{nm}$) from the surface roughness ($\text{SiO}_x \sim 0.25\text{nm}$). This technique is rather slow but in principle non invasive and very precise. Typically, the x-y-direction errors of the AFM (Veeco Dimension 3100) are below 2% which allows an alignment precision of around 100nm . The biggest advantage of this technique is that we can already characterize our samples and determine very exactly the height of the structures. Thus, individual or small SWCNTs bundles can be distinguished from bundles with many tubes by comparing the height with the mean diameter obtained by e.g. Raman scattering or optical absorption microscopy. Due to the tip convolution, the size information in the x-y plane is of no use.

High-magnification SEM alignment measurements (FEI Nova NanoSem) are a high invasive threat to the samples. During the scanning, the electron beam deteriorate the nanotube wall and a lot of amorphous carbon is deposited by the beam due to the bond-breaking of hydrocarbons. For instance, during one high resolution image ($20\text{k}\times$, beam current = 100pA , chamber pressure = 10^{-5}mbar), a 1.5nm thick amorphous carbon layer is deposited, as determined with AFM. However, using very low acceleration voltages

(1-2keV) and the smallest magnification available (2500×), easy visualization without contamination can be achieved. The SWCNT image is obtained by voltage contrast due to charging rather than by direct backscattering of the electron beam by the SWCNT carbon lattice[83]. The detection of the voltage contrast in the micrographs results in augmented tube diameters (~50nm) when compared with AFM scans of the same tubes (~0.7-3nm). This low-magnification mode is quite non-invasive because the carbonaceous dots caused by the e-beam don't form a continuous film. The transport measurements of samples prepared with and without the usage of a low-magnification SEM positioning step indicate a negligible resistance alteration.

4.3 Synthesis of SWCNTs - Basics

Nowadays there exist plenty of different methods and recipes to synthesize SWCNTs, each with their own advantages and disadvantages. Some tube properties, such as mean diameter, purity or amount of tube walls can already be triggered by the production method (up to a certain extend). The growth of SWCNTs requires the use of metallic catalysts and the diameters range between 0.4 and 3nm[84, 85], whereas the length can be up to several centimeters[78, 86]. Nowadays, virtually any metal can be employed in the growth of SWCNTs. In the beginning, transition metals were used in the synthesis, but recently, also non-magnetic catalysts[87] or even noble metals such as gold[88] were able to assist a successful SWCNT growth. The as-produced soot has many contaminating side-products like MWCNTs, graphitic and amorphous carbon, as well as catalyst particles, and a lot of effort has to be done to purify the as-produced sample. The metrology of the synthesized tubes is still a quite challenging task, so that mostly an estimation of SWCNT amount in the produced soot is given as classification. Unfortunately, up to now, it is not possible to grow tubes with a specific (n, m) chirality and thus, the soot usually contains a mixture of many chiralities. Therefore, every macroscopic sample comprises a distribution of nanotube diameters with both semiconducting and metallic SWCNTs present.

There are three main routes of carbon nanotubes synthesis. In the arc discharge and laser ablation methods, a graphitic carbon target admixed with metallic catalyst is evaporated at very high temperatures. In chemical vapor deposition (CVD), a carbon source is streamed over catalysts particles and catalytically decomposed. We will give now a brief summary of the main ideas.

- **Arc discharge:** The first unambiguously reported MWCNTs were - accidentally - synthesized with this method in 1991 [4]. This technique utilizes two graphitic rods brought close together employing high currents around 100A and 20V and was originally used for the synthesis of C_{60} fullerenes. In the direct arc, the plasma reaches temperatures around 3000°C. With the aid of some percent of admixed catalyst particles, the first SWCNTs were obtained in 1993[6, 7]. The nanotubes are usually collected directly on the reaction chamber. The quality of the as-produced tubes normally is very good with few structural damages but the yield around 20% is rather low. Due to the required large post-production purification, this method got quite out of fashion nowadays.

- **Laser ablation:** In a furnace held at 900 to 1200°C, a powerful laser evaporates the graphitic target and the vaporized carbon carried by an inert gas to a cold finger grows nanotubes of superb quality due to the high temperature environment. The high yield around 70% produces a dense entangled mat of bundles consisting of rather short SWCNT (around some μm). This is the only technique up to now which produces SWCNT with a diameter distribution sufficiently narrow to observe the optical transitions between the sharp one-dimensional peaks in spectroscopic investigations like optical absorption and photoemission spectroscopy[89].
- **Chemical Vapor Deposition:** SWCNTs are produced by streaming a gaseous carbon source over catalyst particles at elevated temperatures between 600 and 1100°C, produced by plasma or heat radiation. Another approach employs a floating catalysts source like pentacene providing carbon plus the required catalyst particles[90]. In both cases, the (molten) metallic catalyst particles act as nucleation sites and absorb carbon atoms. When the particle gets oversaturated, regular carbon structures start to form at the particles surface and eventually, nanotubes start to grow. This method can be easily upscaled. The longest SWCNTs (up to centimeters) can be synthesized with this method[86]. The diameter distribution of the CVD methods employed is rather large and often, the as-produced nanotubes have more intrinsic structural damages when compared to laser ablation tubes. Depending on the density of the catalyst particles, individual up to dense forest of CNTs can be produced. The big advantage of this technique is the possibility of direct and patterned growth of CNTs on a chip. Thus, we employed this technique and will present our CVD results in the next section.

4.4 Chemical vapor deposition

Perhaps the most important part of the device fabrication is the availability of good quality nanotube samples. Whereas laser-ablation and arc-discharge tubes are mostly very defect-free, the tube rebundling and substrate contamination drawback an easy implementation. Devices prepared by using wet-chemistry drop-coating usually exhibited a larger resistance. Thus, we employed and improved diluted and patterned synthesis via CVD. Table 4.1 summarizes the optimized parameters and resulting nanotube types of large variety of CVD synthesis processes carried out in the last two years at the IFW. The results were published in several papers as listed in the last column.

As demonstrated by these reports, the temperature range of a successful SWCNT synthesis is quite large, between 680°C and 1050°C, and depends basically on the catalyst and carbon feedstock employed. We used many gaseous (methane, CH_4) as well as liquid carbon feedstocks such as ethanol($\text{C}_2\text{H}_5\text{OH}$), cyclohexane(C_6H_{14}), *n*-heptane(C_7H_{16}), as well as the N-doping acetonitrile($\text{C}_2\text{H}_3\text{N}$) and benzylamine($\text{C}_7\text{H}_9\text{N}$), all purchased from VWR (*Germany*). Each catalyst type has a minimum temperature, the eutectic limit, at which catalytic decomposition of the feedstock occurs. On the other hand, for too high temperatures, self-pyrolysis of the carbon feedstock sets in[92]. Thus, a temperature window has to be found where the catalyst is active without carbon self-pyrolysis. At the ideal temperature, the catalytic decomposition rate matches the rate of nanotube growth.

Soot	C-feedstock	Catalyst	T [°C]	H ₂	Pressure
SWCNT	<i>n</i> -heptane	MgO + Ni/Co	680-850	Pre	HV/VP [76]
	Ethanol	MgO + Ni/Co, Co/Mo, Fe/Mo, Fe	800-900	Pre	HV/VP [91]
	Methane		900-1000		
	Methane	Al ₂ O ₃ + MoO ₂ + Fe(NO ₃) ₃ (salt)	950	Growth	0.5bar
	Ethanol	Ferritin & Co-ApoFerritin	800-900	Pre	0.6bar
	Ethanol	1nm Co or 1nm Fe	800-900	Growth	Ar, 1bar
	Methane		1000		
	Cyclohexane	10nm Al ₂ O ₃ +	720-820	Pre	HV/VP [92]
	Hexane/Methane	1nm Fe	900		1bar/VP [93]
DWCNT	Ethanol	MgO + Co/Mo	940	Pre	HV/VP [94]
MWCNT	Cyclohexane	10nm Al ₂ O ₃ + individ. Fe particles	800	Pre	HV/VP [95]
					[96]
N-FWCNT	Acetonitrile	10nm MgO + 1nm Fe	900	Pre	HV/VP [97]
N-SW/DW	Benzylamine	MgO, Al ₂ O ₃ + Mo/Fe(citrates)	900-1000	Pre	HV/VP [98]

Table 4.1: CVD synthesis parameters of single, double, multi and nitrogen-doped few wall CNTs produced at the IFW. Thin films are used when the thickness is given, wet chemistry (acac) when not. In the H₂ column, Pre and Growth indicate H₂ treatment before and meanwhile synthesis. In the pressure column, HV denotes that the feedstock is fed into a reaction chamber pumped to high vacuum; VP signifies that the liquid carbon feedstock is held at room temperature and normal vapor pressure is used. Last two rows show the results of N-doped nanotubes.

We followed two synthesis approaches: drop-coating of ferritin or a mixture of oxide nanoparticles and organometallic catalysts dispersed in organic solvents[76, 91, 94] as well as evaporating thin metal films[95–98]. They can be employed in a controlled growth at desired position for integration in transport devices.

4.4.1 Experimental setup

The following three different catalyst types were employed:

1. High purity oxide nanopowders (Al₂O₃ or MgO, *Sigma-Aldrich*) were mixed with transition metal precursors, namely Fe, Mo, Ni or Co acetylacetonate (acac) (*Merck*, >98% purity). The oxide nanopowder serves as a sponge for the liquid metals and prevents the liquid particles clustering together, thus enabling small nucleation centers needed for SWCNT growth. The stirred powder was sonicated in methanol of spectroscopic quality and were subsequently drop-coated on the substrates, clean silicon wafers with a 100nm silicon oxide layer or molybdenum sheets.
2. A defined amount of cobalt or iron can be inserted in the protein shell of Apoferritin from horse spleen (*Sigma-Aldrich*) following a wet chemistry recipe[99]. A theoretical loading factor of 2250 Co atoms was achieved by adding 18 cycles of a solution of cobalt [Co(NO₃)₂ (25mMol, 50μl)], and H₂O₂ as an oxidant (30%, 0.07mMol, 23μl). The resulting dissolved ferritin was then spin-coated onto the substrates (30s

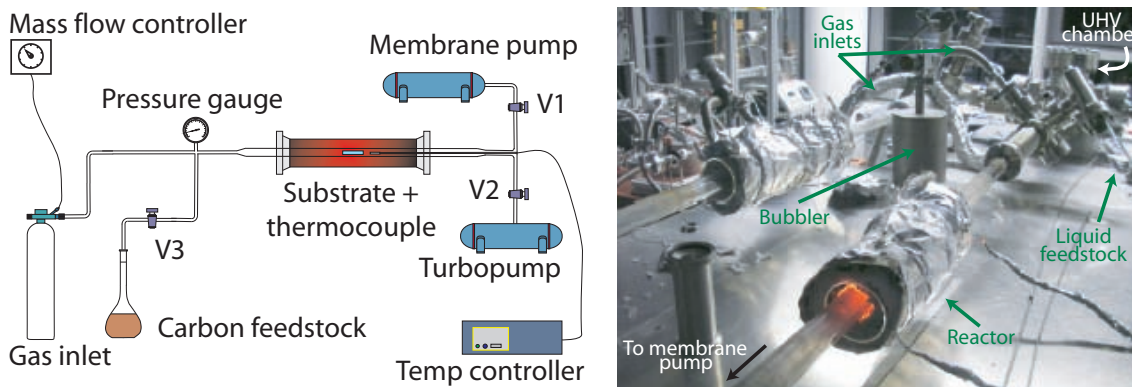


Figure 4.2: Sketch and photo of the hot wall CVD reactor used for the nanotubes synthesis

at 600rpm, 3min at 4000rpm) and thoroughly washed in de-ionized water. Before initiating the synthesis, the protein shell was burnt in air at 400°C for 5 minutes. This insertion procedure yielded small cobalt or iron catalyst particles well dispersed on the substrates.

- Thin catalyst films were directly sputtered, thermal or e-beam evaporated at a minimum pressure of $5 \cdot 10^{-7}$ mbar and the film thickness was controlled by an oscillating quartz crystal monitor. The desired material to deposit was constantly evaporated and the accuracy on the homogeneity achieved was around 90%.

The substrates were then put into a purpose-built horizontal high-vacuum hot wall CVD oven consisting of a 3cm wide quartz tube connected to a turbo molecular pump and a gas inlet, as sketched in Fig. 4.2. To control the temperature, a K-type thermocouple was inserted in the hot zone. After reaching high vacuum ($< 1 \times 10^{-6}$ mbar), the substrates were dried at 400°C for at least one hour to remove any remaining humidity and to initiate the decomposition of the organometallic compounds. While heating to the reaction temperature, H₂ with a flow rate of 2000sccm at 60mbar was fed through the system. In the case of the spin-coated catalyst solutions, the system was evacuated again to high vacuum after five minutes. Once the synthesis temperature was reached the substrates were exposed to methane or the vapor pressure of liquid carbon feedstocks held at room temperature. A mixture of Argon and H₂ is bubbled through ethanol and streamed over the substrates covered with the thin metal films. We varied the temperature between 400°C to 1050°C and the growth time between 5 to 20 minutes. The as-grown samples were analyzed with multifrequency resonant Raman spectroscopy. The Raman spectra were recorded with a Dilor xy triple axis spectrometer for the 2.50eV - 1.83eV laser excitations and a Bruker Fourier Transform (FT) Raman spectrometer with a 1.16eV excitation. All spectra were recorded under ambient conditions with the 180° backscattered light analyzed. The products were imaged with AFM, SEM and TEM (FEI Tecnai F30) using an acceleration voltage of 300kV.

4.4.2 Characterization of the as-grown SWCNTs

We started the investigation with drop-coated substrates. They are thickly covered to ensure an easier characterization of these bulk samples and optimize the synthesis parameters accordingly. Resonant Raman spectroscopy is the first method to choose after the synthesis because of the very fast and non-invasive determination of SWCNT or few-wall CNT (FWCNT) in the soot. For most carbon sources we found a good working catalyst composition and we will start to present Raman scattering experiments of samples of sufficiently high yield.

Bulk samples

We have investigated various metal acac such as Fe, Mo, Ni and Co (acac) using various liquid carbon feedstocks. Bulk samples are achieved by using a mixture of nickel(III)-acac [$C_{10}H_{14}NiO_4$] and cobalt(III)-acac [$C_{15}H_{21}CoO_6$] in equal amounts (by weight) as catalysts. An outstanding selectivity towards a high yield SWCNT growth is obtained when employing *n*-heptane as carbon feedstock. In the case of Fe, Ni, Co or Mo, only moderate SWCNT growth was obtained throughout the temperature range. Regarding the weight ratio metal to oxide nanopowder support only a weak dependence of the overall SWCNT yield was observed upon variation between 1:5 and 1:20 with the optimum at 1:10. The SWCNT synthesis was found to be independent of the chosen oxide powder support. Nevertheless due to easier handling, MgO (particle size around 13nm) was used throughout for the reported results. Typical resonant FT-Raman spectra of the as-produced samples are

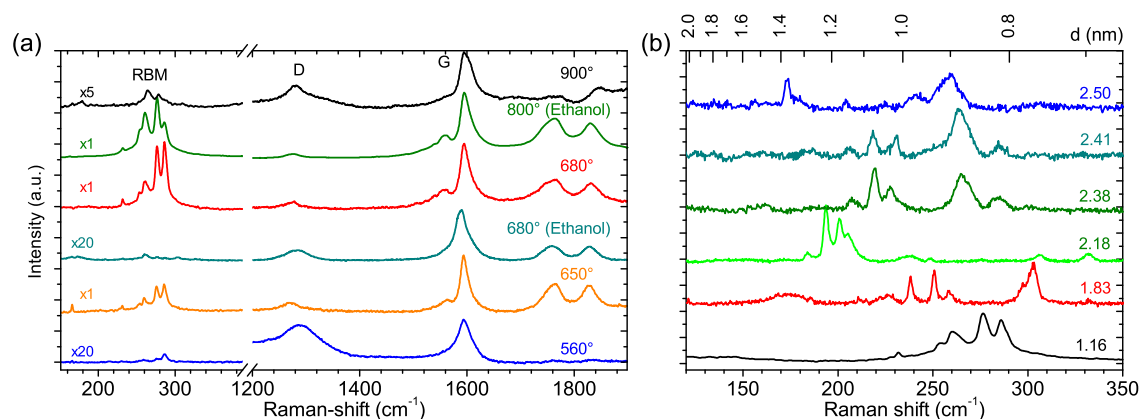


Figure 4.3: (a) FT-Raman spectra of SWCNTs made with Ni/Co (acac) employing *n*-heptane and ethanol as carbon feedstocks for different synthesis temperatures (indicated on the right). (b) Radial breathing mode resonance peaks of a SWCNT sample synthesized at 680°C with *n*-heptane, measured with different laser lines (indicated on the right of the graph in eV). The axis at the top indicates the tube diameter d .

depicted in Fig. 4.3(a) for different synthesis temperatures. The G mode around $1590cm^{-1}$ is present in sp^2 carbon systems like graphite and carbon nanotubes. In addition, around $1300cm^{-1}$ the disorder induced D line is observed. This mode is due to second order Raman scattering on defects[100, 101]. Therefore the relative ratio of the D to G mode

(D/G) is a measure of the quality of the SWCNTs. A unique feature of SWCNTs is the presence of the radial breathing mode (RBM) between 160cm^{-1} - 350cm^{-1} which is a clear indication of successful SWCNT formation. From the frequency of the RBM, the diameters of the tubes can be determined[102] according to $d=223/(\omega-10)$. At 560°C the onset of SWCNT formation is observed as the RBM in Fig. 4.3(a) arises with an initial D/G ratio of 1. Upon increasing the reaction temperature, the D mode diminishes and nearly vanishes, whereas the RBM clearly becomes bigger. For a better comparison, some of the spectra are scaled as labeled in the graph. Since the underlying silicon was never detected, the sample thicknesses were always larger than the laser penetration depth and thus the scaling factors are a measure of the relative SWCNT content. The samples grown between 650°C and 740°C showed a strong RBM response as well as increased total scattering rates, demonstrating a very high SWCNT yield compared to the spectra of other synthesis temperatures. At higher temperatures (e.g. 900°C), the RBM mode diminishes and the D/G ratio increases again due to the loss of selectivity, indicating the onset of counterproductive pyrolysis of *n*-heptane. At 680°C , the RBM peak exceeds the tangential G mode and the D/G ratio is as low (1/15), indicating exceptionally high quality SWCNTs at a rather low synthesis temperature.

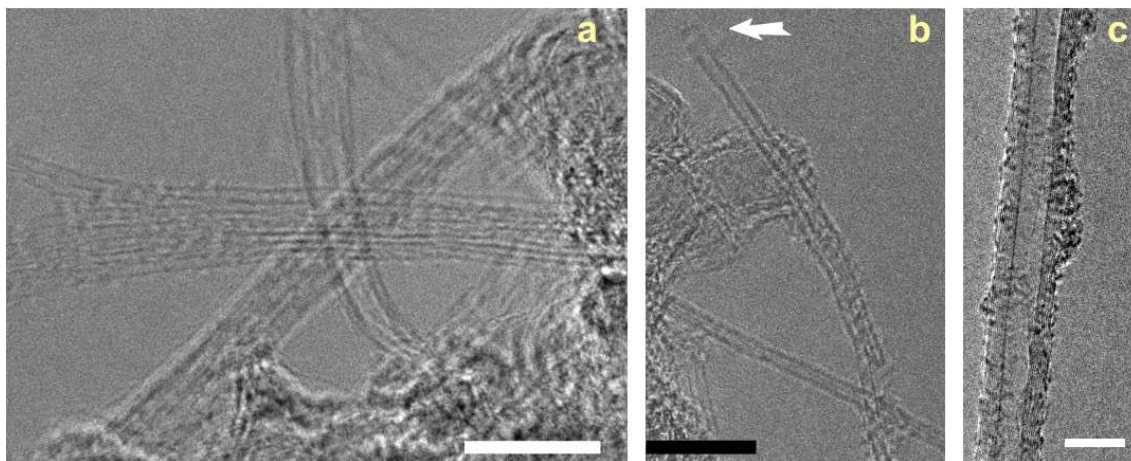


Figure 4.4: TEM images of (a) bundled SWCNTs and (b) individual SWCNTs with a particle-free end as indicated by the arrow, synthesized at 680°C and (c) typical MWCNT image (900°C). In all cases *n*-heptane was used. Scale bars represent 10nm .

When using ethanol, the optimal temperature window is shifted upwards. At 680°C the relative Raman intensity is substantially reduced, as depicted in Fig. 4.3(a). A weaker RBM and an overall lower yield as compared to the synthesis using *n*-heptane is obtained. However, at 800°C the spectrum is very similar to the one of the *n*-heptane sample grown at 680°C [91, 103]. Thus, both feedstocks are able to synthesize high quality SWCNTs at different temperature windows, with the optimum at 680°C for *n*-heptane and 800°C for ethanol.

We now turn to a detailed analysis of a typical sample grown at optimal parameters, regarding the diameter, diameter distribution and overall morphology of the as-produced tubes. As an example, we will first discuss the results of the *n*-heptane soot synthesized at 680°C . To investigate the diameter distribution, we carried out multi-frequency Raman

spectroscopy. In Fig. 4.3(b) the RBM region using different excitation energies is shown. The upper axis depicts the diameter. According to the Kataura plot[102] SWCNTs with diameters between $d=0.7\text{nm}$ and $d=1.5\text{nm}$ can be observed, which is consistent with previously reported values for CVD grown SWCNTs using other carbon sources[91, 104]. This points out that the diameter distribution is mainly governed by the size distribution of the catalyst particles and not by the choice of the carbon feedstock. A slightly lower RBM/G ratio is obtained for the multilayer-grown material[91]. The sample has a very low catalyst particle concentration, but nevertheless, the D/G ratio is roughly doubled when compared to the wet chemistry approach.

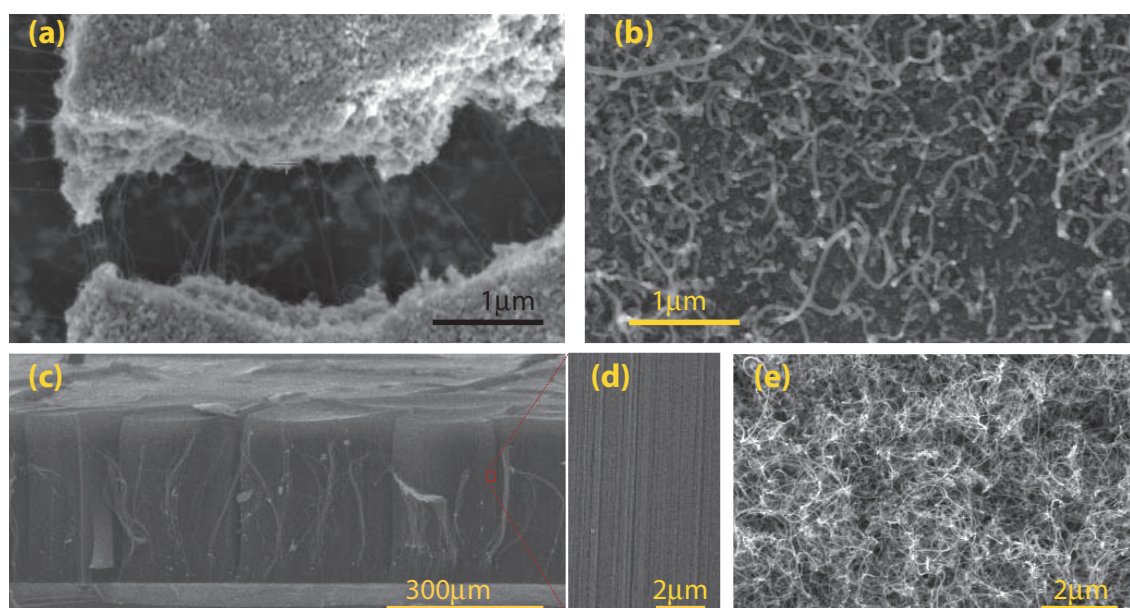


Figure 4.5: SEM images of the as-grown CNT employing the wet catalyst (a,b) and multilayer approaches (c-e). Using *n*-Heptane and Ni/Co (acac) admixed with MgO resulted in SWCNT bundles bridging cracks in the catalyst film at 680°C (a) and thick tubules at 900°C (b). One minute cyclohexane followed by nine minutes methane streamed at 900°C over a homogeneous multilayer film composed of $10\text{nm Al}_2\text{O}_3 / 1\text{nm Fe}$ resulted in vertical aligned thick SWCNT forests (c). In the side-view image, the substrate is at the bottom. The alignment is shown in the augmented image (d). The growth direction is upwards. When cyclohexane is decomposed at 800°C , a substrate heavily covered with rather messy curled SWCNT bundles is obtained (e).

To provide direct evidence of synthesized SWCNTs, we carried out TEM measurements. A copper grid is pressed on the as-grown soot or the material dispersed in acetone is drop-coated on the grid. In Fig. 4.4 typical TEM micrographs of the as-produced tubes using *n*-heptane are shown. In Fig. 4.4(a) bundled SWCNTs and in Fig. 4.4(b) individual SWCNTs, synthesized at 680°C , can be observed. The tubes are very clean showing only a vanishingly small coverage of amorphous carbon species, demonstrating the high quality of the as-grown material. Fig. 4.4(b) also shows an individual SWCNT with a dangling particle-free open end, as indicated by the arrow. At higher temperatures (900°C), MWCNTs of varied diameter like the one shown in Fig. 4.4(c) are found. Despite intensive TEM studies on various samples synthesized between 650°C and 740°C , we did not find

more than the odd occurrence of MWCNTs. This demonstrates that the *n*-heptane CVD process is highly selective toward SWCNT synthesis at these temperatures.

The diverse morphologies of the as-grown material at different synthesis temperatures are shown by the typical SEM images in Fig. 4.5. In the wet chemistry approach (a,b) *n*-heptane and in the 10nm Al₂O₃/1nm Fe multilayer film (c,d) cyclohexane/methane was used. The sample in (a) is grown with optimal process parameters and shows predominately very small tubules bridging a horizontal crack in the catalyst particle film. Presumably, most tubes grow inside the space of the oxide particles not visible in SEM. In a cross-sectional view, the tubes protruding the catalyst film can be visualized. Nevertheless, a length determination is not possible. In samples grown at 900°C only a few regions with small tubules similar to those in (a) are found. As shown in Fig. 4.5(b), predominately very thick tubules with diameters usually over 50nm are detected, suggesting heavy growth of MWCNTs, as confirmed by the TEM studies.

This picture changes drastically when considering multilayer films and cyclohexane. The evaporated 10nm Al₂O₃ / 1nm Fe film yields vertically aligned CNTs of typically 200-400 μ m at optimal parameters. When using a two stage approach of 1 minute cyclohexane followed by 9 minutes methane at 900°C even a much better vertical alignment can be achieved, as shown in Fig. 4.5(c). A closer view demonstrates the alignment of the SWCNT bundles in (d). This alignment can be explained by the homogeneous film thickness leading to a uniform catalyst activity on the substrate and a vertical growth of the SWCNTs. Nevertheless, for non-optimal parameters an entangled synthesis of SWCNT bundles is obtained, see Fig. 4.5(e). This method circumvents the heavy catalyst and supporting oxide particle concentration of the wet-chemistry approach.

Individual SWCNT by using diluted catalysts

In order to avoid an extra lithography step of the islands, we also tried to dilute the catalyst concentration. Under a critical concentration, however, no effective SWCNT production was observed any more. In both above discussed catalyst types, it was not possible to diminish the SWCNT yield substantially to obtain a synthesis route suitable for device integration. When diluting the catalyst below a critical concentration, possibly the catalyst acetyl-acetonates disperse differently to the oxides, inhibiting sufficiently small metal catalyst clusters which are activated for SWCNT growth.

Very long individual or small bundled SWCNTs of more than 300 μ m in length are obtained when using a thin monolayer of 1nm Fe or 1nm Co. Typical SEM and topographic AFM images are shown in Fig. 4.6. As expected, the resulting tube yield is much lower when compared to multilayer films with an additional aluminum oxide layer under the catalyst film, cf. Fig. 4.5(c,d). In no synthesis experiment utilizing monolayers, thick forests produced with multilayers were obtained. Thus, only few catalyst clusters are active during the synthesis. As confirmed by AFM, the Al₂O₃ layer forms a smooth undulated surface. Thus, the melting catalyst film can form a more uniform particle size distribution in these depressions. However, without the aid of aluminum oxide the melting thin monolayer forms not very homogeneous clusters regarding overall spreading of the catalyst particle islands [Fig. 4.6(c)] as well as the particle size (between 5 and 12 nm) [Fig. 4.6(d)]. The tube height determination at particle sparse regions in Fig. 4.6(d) gives 1.4nm, indicating individual SWCNT growth. We tried also with thinner evaporated films

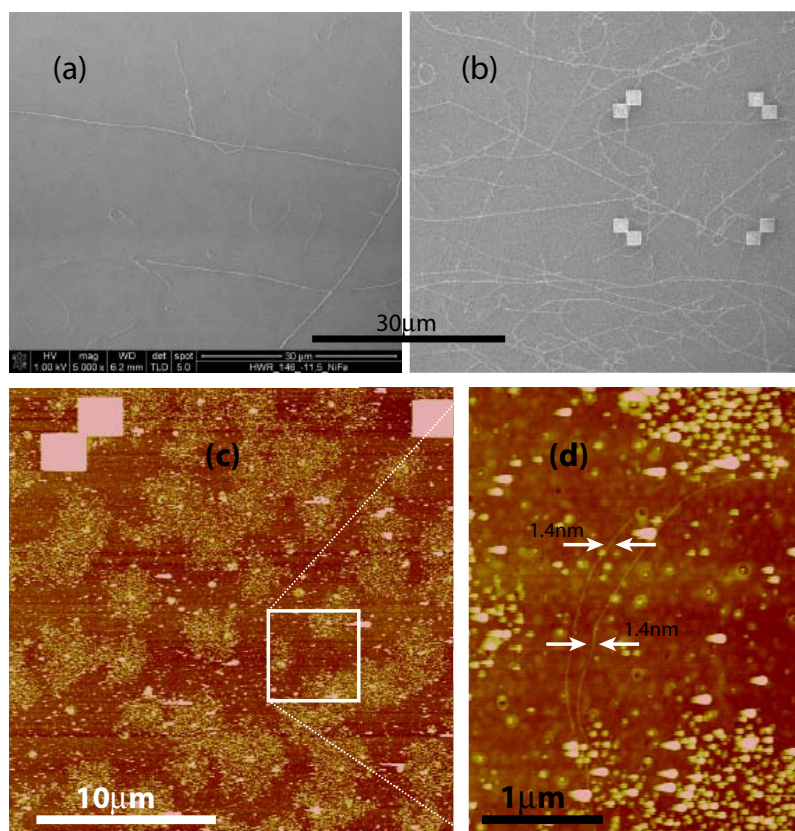


Figure 4.6: SEM and topographic AFM images of SWCNTs grown on homogeneously evaporated thin-films. Methane and a synthesis temperature of 1000°C was employed. Bulk samples using (a) 1nm Fe and 1nm Co (b-d) catalyst films. The AFM images (height scale 10nm) show that the thin metal film of 1nm cluster together to small particles of $5\text{-}10\text{nm}$ in height distributed not very homogeneous (c,d). Only a few are able to activate the growth of SWCNT. Two SWCNTs with a diameter of 1.4nm are shown in (d). The alignment markers in (b-d) are patterned after growth.

(0.6nm Fe) resulting in the same sample morphology with a thick SWCNT covering of the substrate. Depositing even thinner films makes no sense because we are already at the limit of the evaporator machine.

When using Ferritin and Apoferritin with inserted cobalt, individual SWCNT grow at arbitrarily low concentrations. After burning the ferritin protein shell at 400°C in air, we end up with small dispersed iron or cobalt particles, respectively. For a more reproducible dispersion, the silicon oxide surface is hydrophilically treated using H_2SO_4 and H_2O_2 . The concentration of the ferritin solution was adjusted to 0.7mg/ml in both cases. It is believed, that Co-Apoferritin yields smaller catalyst particles when compared to Fe-Ferritin due to the lower mobility of the cobalt atoms on the silicon substrates at elevated temperatures, inhibiting the formation of larger catalyst clusters[105, 106]. The smaller catalyst particles are more suitable for a selective SWCNT growth. Indeed, the SEM images of Fig. 4.7 of the as-produced material indicate a higher SWCNT selectivity of Co-Apoferritin when compared to Ferritin.

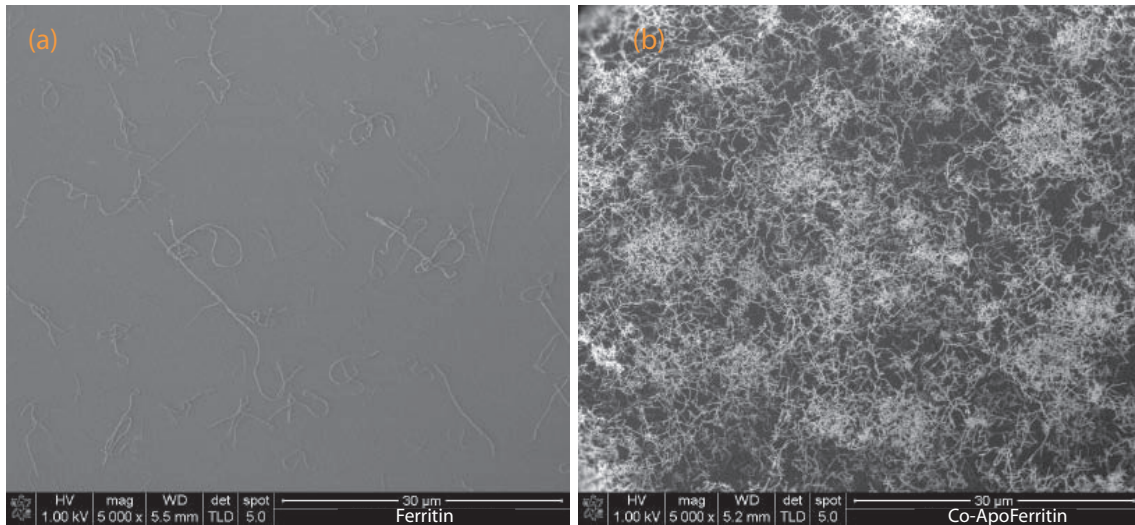


Figure 4.7: SEM images of SWCNTs synthesized by streaming ethanol at 800°C over Ferritin (a) and Co-ApoFerritin (b) homogeneously dispersed on the substrate.

Pre-patterned growth of individual SWCNTs

Finally we explored the possibility to synthesize individual SWCNTs at predefined positions on the substrate. We prepared $1\text{-}5\mu\text{m}$ big catalyst islands, small 'Petri-dishes', with standard electron beam lithography[77], as introduced in the next section 4.5. The regions in between these islands are catalyst-free flat silicon surfaces suitable for tube location and height determination by AFM means. We followed two approaches, i.e. wet-chemistry as well as thin film deposition in the Petri-dishes. We first summarize the results when using a diluted $\text{MgO} + \text{Ni/Co}$ (acac) solution.

Methanol as organic solvent was used due its low chemical interaction with the resist and a small amount of the catalyst solution was dropped on the resist. Fig. 4.8(a) shows an overview of the patterned islands and (b) a single island. The micrographs (c) and (d) show typical images of the nanotubes rooting at the edges of the islands (shown in the right of the pictures). In the SEM image in Fig. 4.8(c) lots of nanotubes can be observed bridging the metal covered oxide particles on the island as well as growing off the island onto the substrate. Due to the non-conducting nature of the silicon wafer with a thick oxide layer, the captured contrast of the tubes changes at the moment the tubes touch the substrates surface, as can be observed throughout the micrograph and indicated exemplarily by the arrow in the top of the image. The SEM contrast is very high for acceleration voltages under 1kV but is reduced substantially for higher voltages. Varying the synthesis time between 5 and 20 minutes did not visibly change the lengths of the nanotubes of typically up to $10\mu\text{m}$. As seen in TEM, the nanotube ends are metal particle free. This indicates catalyst poisoning or a counterproductive carbon-substrate interaction.

The tubes lying on the surface could be further investigated by an AFM in tapping mode. A typical phase image of the catalyst islands and SWCNTs lying on the substrate is shown in Fig. 4.8(d). We used a smaller catalyst film with a height $\sim 150\text{nm}$ compared to 500nm used in (c), resulting in a reduced amount of synthesized nanotubes. Accumulating

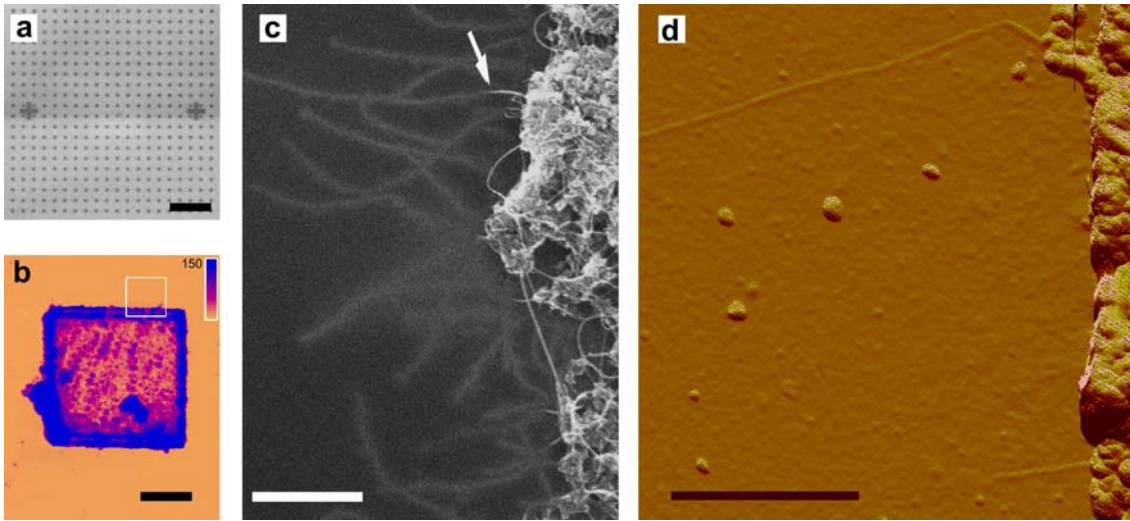


Figure 4.8: Individual carbon nanotubes growing from $MgO + Ni/Co(acac)$ drop-coated on pre-patterned drop-coated catalyst islands on SiO_x . (a) SEM overview of patterned islands. Bar is 0.1mm. (b) Typical topographic AFM picture of a doughnut-like catalyst island. Bar is $2\mu m$. The individual tubes cannot be seen due to the large height scale of 150nm. (c) SEM micrograph showing the entangled nanotubes on the catalyst island, as well as tubes lying on the insulating SiO_x . Scale bar is 500nm. (d) Augmented AFM phase image, as indicated by the square in (b), of individual SWCNTs growing from the catalyst island. Scale bar is 500nm.

the height over the whole tube in the corresponding topographic micrograph of Fig. 4.8(d) amounts to a diameter of $d=0.7\pm 0.1nm$. Nearly all of the tubes measured with AFM gave individual SWCNTs with heights between $d=0.7nm$ and $d=1.5nm$ and lengths of up to several μm . This clearly shows the potential of individual SWCNTs synthesis on pre-defined positions with high selectivity using *n*-heptane at temperatures of $680^\circ C$. The main challenges of this strategy are to assure a clean surface area for AFM measurements. To avoid catalyst penetration, a bake-out step at $150^\circ C$ prior to the lift-off procedure is employed. Furthermore, the catalyst height and thus the number of synthesized tubes is only controllable up to a certain degree. However, an adjustment of the growth parameters has more influence on the amount of individual nanotubes routing off the pre-patterned catalyst islands.

The most promising approach to obtain individual and separate SWCNTs on a clean surface is the synthesis approach using pre-patterned thin-film islands. Fig. 4.9(a) demonstrates, that many SWCNTs grow off 1nm thick cobalt islands using ethanol at $850^\circ C$. The nanotube lengths range typically between 2 and $50\mu m$. As the length distribution is very broad, SWCNT sufficiently isolated for integration into electronic devices can always be found. To avoid an extra lithography step to pattern the alignment markers, we used the proper Petri-dishes for the deposition of 30nm Cr under the catalyst layer. Chromium was used because it can withstand the high synthesis temperatures. The presence of Cr required that some parameters, especially the gas flux, had to be adjusted. However, for optimized conditions the synthesis is independent of the presence of the underlying Cr layer. In Fig. 4.9(b,c), the parameters are adjusted to yield less nanotubes for an easier contacting procedure and the catalyst alignment marker allow a precise tube localization.

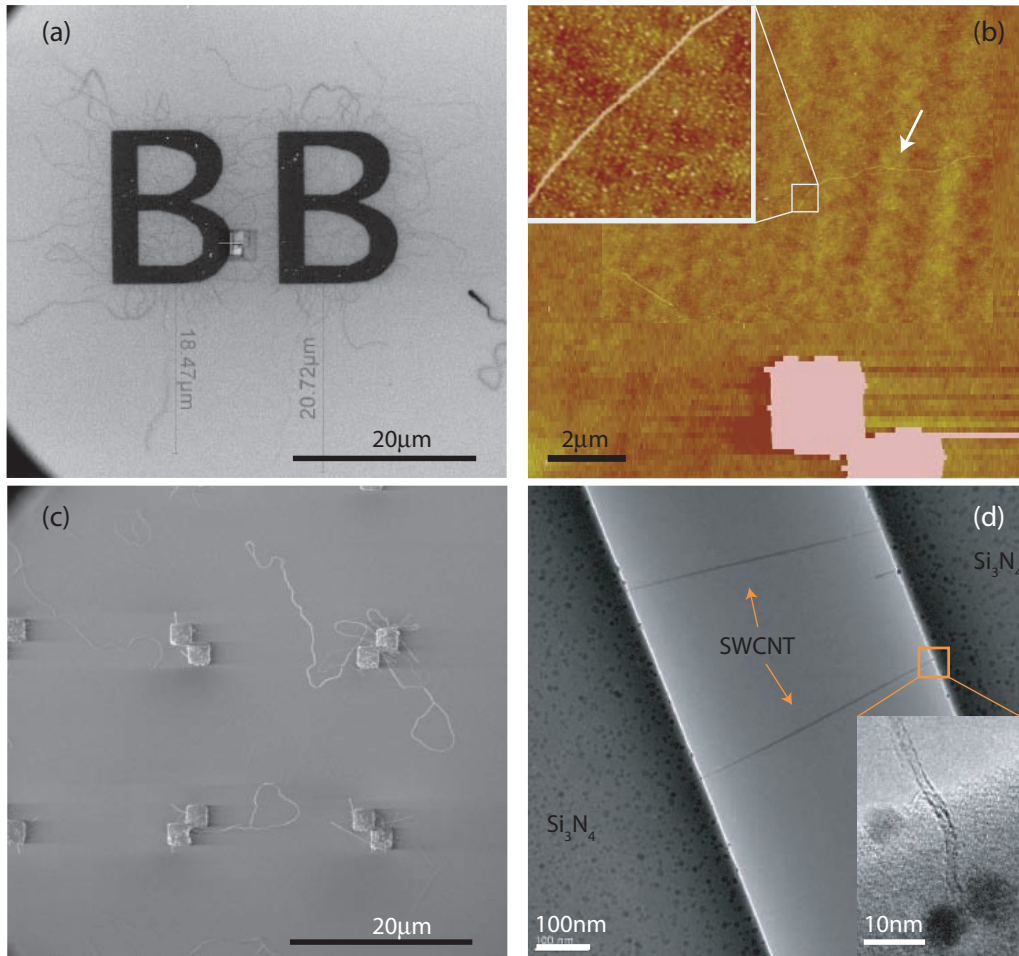


Figure 4.9: SEM and AFM images of individual and small bundles of SWCNTs growing off pre-patterned thin film islands using Ethanol at 850°C . 1nm Co (a) and 30nm Cr / 1nm Co (b,c) catalyst films used. (b) Topographic AFM picture with a height scale of 10nm. Inset: High-resolution image with a height scale of 5nm of the SWCNT marked by the arrow. (d) A TEM image of SWCNT bridging a slit fabricated in a thin 100nm thick Si_3N_4 membrane. Inset: High-resolution image of an individual SWCNT.

Fig. 4.9(b) depicts the position respectively to the alignment marker (bottom part) of an individual SWCNT marked by arrows. The height $d = 1.0 \pm 0.1 \text{ nm}$ of the SWCNT marked by arrows is determined with a high-resolution AFM scan (see inset). The AFM measurements on most samples reveal a height distribution between 0.5 and 2.5nm, indicating the selective growth toward individual and small bundles of SWCNTs.

Synthesis of suspended SWCNTs

A very interesting and active field is a combined study of transport properties with spectroscopical or microscopical tools in order to gain further information about the nanotube nature. The chirality (n,m) assignment of individual, free-standing SWCNTs can be ob-

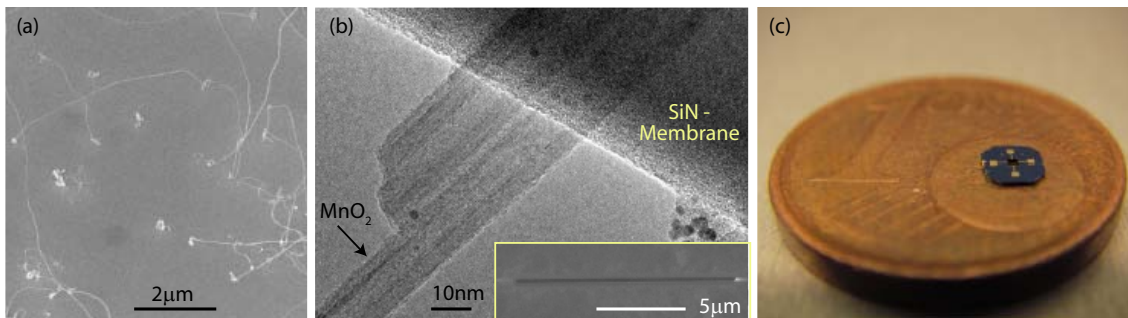


Figure 4.10: Towards free-standing nanotube devices on Si_3N_4 membranes. (a) SEM picture of nanotubes grown on a 100nm thick Si_3N_4 membrane using iron salt and methane at 950°C . (b) TEM image of MnO_2 nanotubes laying across a slit milled by focused ion beam. Inset: SEM overview of the slit. (c) Photograph of the silicon chip on top of a 1-Cent coin, with the central membrane window and with gold electrodes patterned by e-beam lithography.

tained by fluorescence spectroscopy[107], tunable Raman or Rayleigh scattering[108, 109]. The latter works for every type of nanotube, whereas fluorescence only for semiconducting tubes.

We prepared slits in commercial available 100nm silicon nitride (Si_3N_4) membranes mounted on a $200\mu\text{m}$ silicon support (from *Plano*, Germany). $10\mu\text{m}$ long and $200\text{-}400\text{nm}$ wide slits are milled with a focused gallium ion beam, as shown in inset of Fig. 4.10(b). 1nm cobalt was then sputtered on the membrane and subsequently, we carried out the CVD process with ethanol as feedstock at 900°C . TEM measurements unambiguously demonstrate the synthesis of 1-3 individual and very straight SWCNTs bridging each slit, as shown in Fig. 4.9(d). The inset corresponds to a high magnification micrograph, exhibiting an individual SWCNT with a diameter $d \approx 1.5\text{nm}$. The dark spots on the membrane correspond to the melted and coalesced metal particles. No amorphous carbon or catalyst particles can be observed at the nanotube. The imaging condition with a high acceleration of $V_a = 300\text{kV}$ damage very quickly the tube walls. Currently, we are setting up a new TEM with acceleration voltages down 80kV , allowing a longer exposition time prior to wall deterioration.

Also, wet-chemistry can be employed to synthesize SWCNTs. The SEM micrograph in Fig. 4.10(a) shows SWCNT tubules grown on the intact Si_3N_4 membrane. A TEM image of MnO_2 nanotubes deposited on the membrane and bridging the FIB-milled slit is depicted in Fig. 4.10(b). A successful electrode patterning via electron beam lithography, introduced in the next section 4.5, on the rather small silicon chips (2.9mm in diameter) is very challenging and due to the small size, the resist spin-coating process is far from being reproducible. A successful EBL patterning trial with top-fabricated gold electrodes is shown in Fig. 4.10(c). Also, bigger support chips from other suppliers can be used and we are currently adjusting the TEM holder to house the larger membranes.

4.5 Device fabrication: e-beam lithography

The new system at IFW consists of a high-resolution NanoSEM 200 (*FEI*) with an attached patterning generator (*nanonic*, Germany) and a purpose-made beam blander booster for high blanking rates. The SEM is operated by a hot-thermal Schottky field emitter and high beam currents (up to $7nA$) can be employed for the writing of large structures. The acceleration voltages V_A can be varied between 1 and $30kV$. The 16bit pattern generator allows a very precise beam guiding down to the nanometer scale. We use a spin-coater (*Laurell*) with maximum 6000 rounds-per-minute (rpm) spinning velocity. The preparation chamber is not located in a clean room, but a linear flow-box helps to prevent from contaminating particles. All required organic solvents are furnished from *VWR*, i.e. ethanol (C_2H_6O), acetone (C_3H_6O), methanol (CH_4O), isopropanol (IPA, C_3H_8O), methyl-isobutyl-ketone (MIBK, $C_6H_{12}O$) and N-methyl-2-pyrrolidone (NMP, C_5H_9NO). The organic resist, a polymethyl methacrylate (PMMA) with the chemical formula $(C_5O_2H_8)_n$, consists of long chains of MMA linked by a single C-CH₂ bond and is furnished from *Allresist*, Germany. The PMMA solids content is usually given in % and the number of the monomers in thousands, e.g. 50k PMMA has 50.000 monomers. We adjusted the desired resist thickness by dilution in chlorbenzene, maintaining the same spin-coating parameters.

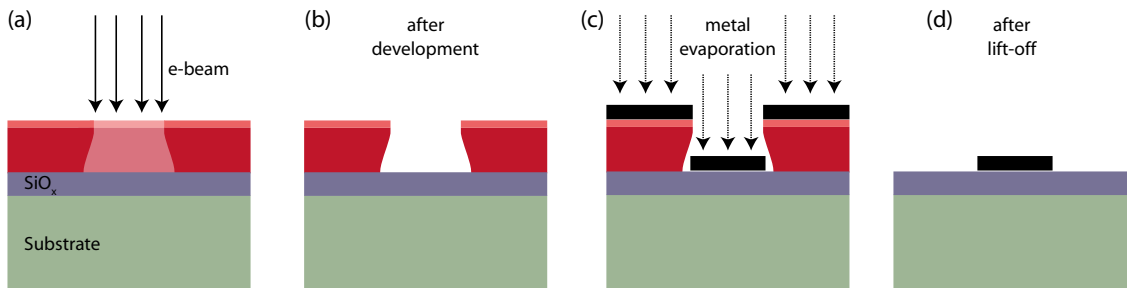


Figure 4.11: Schematics of an e-beam lithography cycle on top and optical microscope images of each step on bottom, scale bar is $100\mu m$. (a) double-layer PMMA resist is spin-coated onto the substrate and subsequently exposed to the e-beam. (b) Development removes the chemically changed resist at the exposed areas. (c) Metal evaporation coats the whole substrate. (d) Lift-off removes the unexposed resist with the metal on top leaving solely the metal at the desired area.

One lithography procedure consists of the following steps and is summarized in Fig. 4.11:

1. If possible, clean sample in acetone and IPA. Then heat out the sample on a hot plate at $150^{\circ}C$ for >10 minutes to get rid of the residue water layer.
2. Spin-coating of first PMMA layer (50k, 9%). The resist is dropped onto the substrates at the acceleration ramp between 2000 to 6000rpm and spinned for 30s at 6000rpm. This yields approximately $200nm$ thickness. Subsequent bake-out for 10 minutes at $150^{\circ}C$.
3. Spin-coating of second PMMA layer (950k, 1%), the procedure is the same as the previous one. This yields $50nm$.
4. e-beam lithography step with alignment procedures on pre-defined markers, see Fig. 4.11(a). The exposed (light colored) areas are chemically changed.

5. Development for 3 minutes in 1:3 MIBK:IPA, then immersing for 1 minute in the stopper (IPA) and dry-blown with nitrogen. The exposed areas are now uncovered of PMMA, Fig. 4.11(b).
6. Metalization of usually 5nmCr/50nmPd or 5nmCr/20nmPd/30nmAu by e-beam or thermal evaporation, Fig. 4.11(c).
7. Lift-off procedure, Fig. 4.11(d). This lifts the metal on top of the PMMA and we end up with metal at the desired, exposed positions (positive process):
 - Immerse in hot acetone or NMP (60°C) for 10 to 30 minutes
 - Leave for >12 hours in solvent bath.
 - Clean surface with strong solvent jet and check in optical microscope, if lift-off was successful. If not, start over again.
 - When metal still does not lift, short dip in ultrasonic bath.
 - Dry-blow with N_2 .

We will now have a short insight into the operation principles of e-beam lithography. Upon irradiating the organic resist, the PMMA is scissored by the high-energetic electrons at the chains between the monomers. This exposed region is more sensitive to the developer which dissolves the resist with shorter chain lengths. As it is a statistical process, there will be a critical irradiating dose when a structure is optimally exposed. Furthermore, MIBK dissolves a greater range of chain lengths, resulting in broader structures, whereas IPA is a very hard developer. Usually we use a mixture of one part MIBK to three parts IPA. Upon entering the resist, the electron beam spot-size broadens from initially $\sim 1\text{nm}$ to over 10nm , thus reducing the resolution of the process. As the penetration depth into the substrate is several μm (depending on V_A), other scattering processes will happen as well. Whereas the energies of the secondary electrons are too low to scissor the chains, the high-energetic backscattered electrons augments the irradiated dosis in the resist. The backscattered electrons leave the substrates up to several μm away from the initial spot, which leads to an unwanted additional exposure and dosis contribution of neighbor structures. This effect is known as the proximity effect and depends on basically everything, e.g. beam spot, substrate, structure neighborhood, resist thickness . . . , thus hindering a global proximity effect correction. To circumvent this aspect in the limit of small structures, tests with a manual correction and varied beam dosis need to be lithographed to adjust the parameters accordingly.

We figured out, that mainly due to our working environment with no controlled humidity, the spin-coating process needed to be improved. The heat-out step before the spin-coating turned out to be crucial in the device fabrication. Furthermore, we observed a large onset of surface roughness due to resist residues at beak-out temperatures above 150°C . For temperatures higher than 180°C , a complete thin resist layer is left on the substrate.

For a successful lift-off process after the EBL and metalization step, the resist profile plays a fundamental role. Monolayer resists, as shown in the cross-sectional SEM images Fig. 4.12(a) could at best be adjusted to have a vertical profile (b) and we could not achieve a reliable lift-off. As sketched in Fig. 4.11(c), a non-continuous metal layer is needed in order to allow the remover to attack the resist and lift the metal. By using a double-layer resist of PMMA 50k/950k, an undercut and successful lift-off could be achieved as demonstrated by Fig. 4.12(c). The 50k resist is slightly more sensitive ($\sim 15\%$) to the

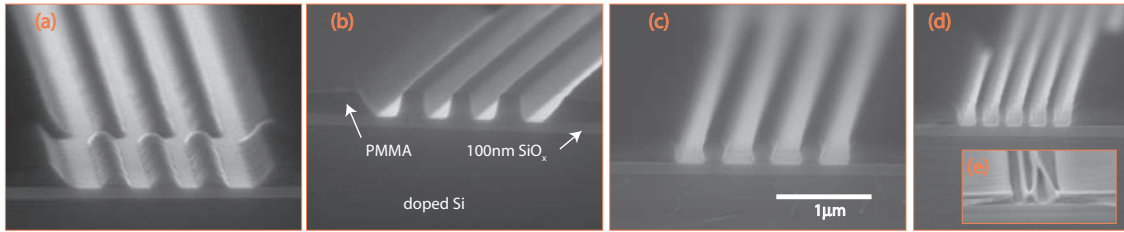


Figure 4.12: SEM images of resist structure on top of 100nm SiO_x : one layer of 200nm PMMA 950k with no undercut (a) and a straight profile (b). Metal lift-off is possible for undercut structures (c) using a 200nm 50k + 50nm 950k double-layer resists. Limit of small structure distances: (d) resist lines could withdraw the surface tension of drying developer, whereas (e) even narrower resist lines of 40nm channel lengths toppled down. $1\mu\text{m}$ scale bar holds for all micrographs.

electron beam than the 950k resist on top, leading to the desired undercut profile. In the limit of small channel lengths, the surface tension of the drying developer toppled down the thin walls of resist, see Fig. 4.12(d,e). A possible solution would be to dry the substrates in a critical point dryer or, up to a certain degree, to diminish the resist height. With the optimized parameters, the lift-off process was successful in most cases and the resulting devices exhibited quite low two-terminal resistance of the order of tenths of $k\Omega$ as will be discussed in more details in the transport measurement chapter 7.

5 Theoretical model

In this chapter we will derive the formula to obtain some electronic properties, like LDOS and conductance of arbitrary one-dimensional systems calculated entirely in real space. Furthermore, we will review a semi-quantical potential to describe the interaction of carbon-carbon as well as some mechanical properties of the systems and will include these atomic energy informations into the simulation of transport properties. Finally, we will introduce a model to determine the action of an external magnetic field on the electronic transport.

5.1 Real-space tight-binding model

The electronic properties are obtained within a tight-binding description using Greens function formalism. We will adopt a renormalization method totally defined in the real space to include directly all nanoscopic structure details, like impurities and topological defects, in the Greens functions and hopping integrals[110]. This method is able to describe arbitrary systems and does not depend on certain structural symmetries. It enables the simulation of complex and quite large structures like heterojunctions and Y-junctions rings studied in this thesis.

5.1.1 Green's function renormalization method

A detailed derivation of the model adopted here can be found elsewhere[111–114]. The electrical properties of CNT systems are studied by using a single π -band tight-binding model. The Hamiltonian is written in the site representation, as a sum over all m lattice sites as

$$\mathbb{H} = \sum_{m \neq n} t_{mn} \mathbf{a}_m^\dagger \mathbf{a}_n + cc \quad , \quad (5.1)$$

in terms of the electronic creation \mathbf{a}^\dagger and annihilation \mathbf{a} operators. cc stands for the complex-conjugated term. The on-site energies are given by $t_{mm} = e_o$ while the hopping integrals t_{mn} are restricted to first neighbor sites. We will use widely the constant hopping integral approach (CHI), where all hopping parameters are considered equal to γ_0 ($\approx -2.7eV$). Using the Green function formalism one defines G as the solution of the inhomogeneous differential equation

$$G^{\{r,a\}}(\omega) = (\omega^{\{r,a\}} - \mathbb{H})^{-1} \quad , \quad (5.2)$$

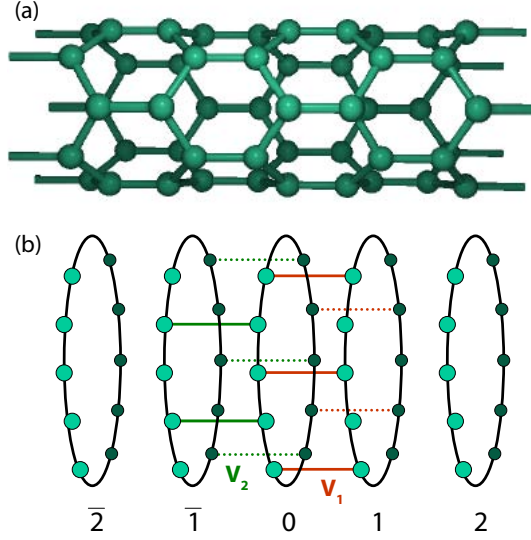


Figure 5.1: Schematic representation of a zigzag SWCNT (top) and the quasi-one-dimensional description of the SWCNT (bottom panel), with the two hopping matrices, V_1 and V_2 , marking explicitly the interactions between alternated carbon sites disposed along the rings.

with w being a complex energy variable. The poles of the Green function define the eigenvalues ϵ of the Hamiltonian. To assure the non-divergence of the Green function over the whole real axis range, a small imaginary part is added, i.e., $\omega^{\{r,a\}} = \epsilon \mp i\eta$. Physically one may think that a finite η value introduces a relaxation time due to electronic scattering mechanisms.

Achiral SWCNTs can be theoretically described by considering a chain of layers disposed along the tubular axial direction as displayed in Fig. 5.1(a). To simulate zigzag SWCNTs, each layer consists of two rings of carbon atoms associated with the two nonequivalent sites of the graphene unit cell. It is connected to the two adjacent layers via two different hopping matrices [see Fig. 5.1(b)] named $V_{01} = V_{10} = V_1$ (joining even numbered atoms) and $V_{0\bar{1}} = V_{\bar{1}0} = V_2$ (odd atoms). All the Green functions are obtained by the matricial Dyson's relation[112, 115, 116]

$$G_{ij} = G_{ij}^0 \delta_{ij} + \sum_k G_{ii}^0 V_{ik} G_{kj} \quad , \quad (5.3)$$

with G_{ij}^0 being the uncoupled propagator. The renormalization procedure starts by coupling layer 0 , 1 , and $\bar{1}$, for example, to their two first neighbor rings respectively, resulting in

$$\begin{aligned} G_{00} &= g + gV_{01}G_{10} + gV_{0\bar{1}}G_{\bar{1}0} \\ G_{10} &= gV_{10}G_{00} + gV_{12}G_{20} \\ G_{\bar{1}0} &= gV_{\bar{1}0}G_{00} + gV_{\bar{1}\bar{2}}G_{\bar{2}0} \quad , \end{aligned} \quad (5.4)$$

where g is the dressed renormalized Green function of the layer, given by $g = (I - g_o V_{oo})^{-1} g_o$, with I being the identical matrix and g_o a diagonal matrix with elements given by $g_{ii} = 1/(w - e_o)$. We use the fact that in pristine achiral SWCNTs, all layers can be taken as equal. The dressed locator after this first step is written in terms of second neighbor layers, and so on. After $N + 1$ recurrence steps, one obtains[114]

$$\begin{aligned}
g^{(N+1)} &= \left[1 - Z_1^{(N)} (1 - Z_2^{(N)} Z_2^{(N)})^{-1} Z_1^{(N)} Z_1^{(N)} - \right. \\
&\quad \left. - Z_2^{(N)} (1 - Z_1^{(N)} Z_1^{(N)})^{-1} Z_2^{(N)} Z_2^{(N)} \right]^{-1} \cdot g^{(N)} \\
V_{1,2}^{(N+1)} &= V_{1,2}^{(N)} (1 - Z_{2,1}^{(N)} Z_{2,1}^{(N)})^{-1} Z_{2,1}^{(N)} Z_{1,2}^{(N)} \quad , \quad (5.5)
\end{aligned}$$

where $Z_i^{(N)} = g^{(N)} V_i^{(N)}$. As $N \rightarrow \infty$, the process converges to a fix point $g^{(N)} = G_{00}$, since $V^{(N)} \rightarrow 0$. The local density of state can be directly obtained from dressed-renormalized Green function by

$$\rho(\epsilon) = \mp \frac{1}{\pi} \text{Im}(\text{Tr} G^\pm(\epsilon)) \quad , \quad (5.6)$$

where the trace is taken over the layer atomic sites. Fig. 3.7 was calculated with this formula.

5.1.2 Electronic transport by the Landauer-Kubo formalism

Electrical transport properties of the carbon nanotube structures are investigated by using the Landauer-Kubo formalism[31, 111, 117]. Within the linear regime, the current of the system is proportional to the external alternating electric field,

$$\vec{J}(\vec{r}, t) = \Gamma(q, w) \vec{E}(\vec{r}, t) \quad , \quad (5.7)$$

where the conductance Γ is the proportional factor. The electronic transport of a system can be thought of a conductor C sandwiched between two semi-infinite leads, R and L (Fig. 5.2). The central region C can be a single tube layer or complex structures such as a large Y-junction ring. The electric field is assumed as constant. The transport through the conductor C can be related to the scattering properties of this region of interacting electrons by the Landauer equation

$$\Gamma = \frac{2e^2}{h} T = \Gamma_0 T \quad . \quad (5.8)$$

The transmission function T represents the probability that an electron injected at one side of the conductor will transmit to the other side. The quantity $\Gamma_0 = 2e^2/h$ is called the conductance quantum. The transmission function can be expressed in function of the

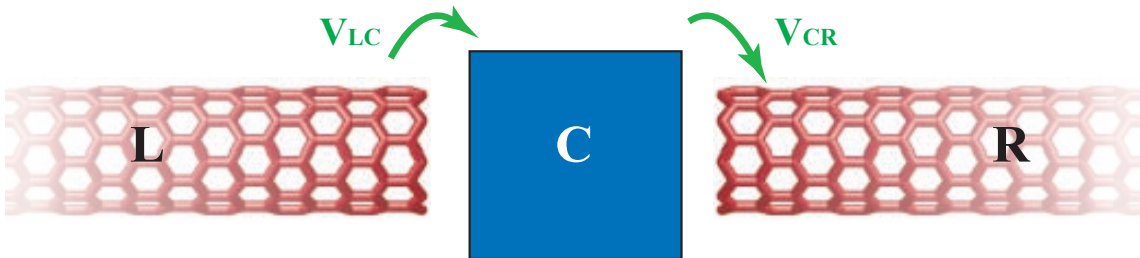


Figure 5.2: Schematic picture of a conductor C connected to two semi-infinite leads L and R via the coupling matrices V_{LC} and V_{CR} .

conductor Green's functions and the coupling to the leads as[31]

$$T = \text{Tr}(\Omega_L G_C^r \Omega_R G_C^a) \quad , \quad (5.9)$$

where $G_C^{r,a}$ are the retarded and advanced conductor Green's functions, and $\Omega_{\{L,R\}}$ describe the coupling of the conductor to the leads. The trace is taken over all atomic sites. From eq. (5.2), one can obtain an explicit expression for G_C [31]:

$$G_C = (\epsilon - H_C - \Sigma_L - \Sigma_R)^{-1} \quad . \quad (5.10)$$

The self-energy terms $\Sigma_{L,R}$ can be viewed as effective Hamiltonians that arise from the coupling of the conductor with the semi-infinite leads. They are defined as $\Sigma_L = V_{LC}^\dagger g_L V_{LC}$ and $\Sigma_R = V_{RC} g_R V_{RC}^\dagger$, with the lead's Green's function $g_{\{L,R\}}$ given by eq. (5.2). The hopping matrices V are indicated in Fig. 5.2 and are non-zero only at sites of conductor-lead connecting atoms. Once the Green's functions are known, the coupling functions $\Omega_{\{L,R\}}$ can be obtained as[31]

$$\Omega_{\{L,R\}} = i(\Sigma_{\{L,R\}}^r - \Sigma_{\{L,R\}}^a) \quad , \quad (5.11)$$

where the advanced self-energy term Σ^a is the Hermitian conjugate of the retarded self-energy Σ^r .

The only unknown quantities in the relations above are the Green's function of the semi-infinite leads. They can be easily obtained by developing the recurrence relation, eq. (5.4), only in one tube direction. One should note that all microscopic details are intrinsically included in this real space picture and the atomic arrangement of the topological defects present at the junctions are properly taken into account, with no need of further approximations.

5.1.3 Electronic transport in SWCNTs

Experimental evidences[34, 35, 37, 38, 47, 118, 119] and theoretical results[120, 121] show that SWCNTs belong to the class of ballistic conductors. In these systems, the transmission probability T is equal 1 and thus, the electrons do not suffer scattering upon transmitting through the conductor. As discussed before, the diffusive transport regime enters the ballistic regime when the free mean path is bigger than the system's dimensions. Experiments show that metallic SWCNTs have free mean paths up to μm lengths[35–38]. As can be seen in eq. (5.8), the conductance in the ballistic regime at zero temperature is quantized and given by integral multiples M of the conductance quantum $\Gamma_0 \approx (13k\Omega)^{-1}$:

$$\Gamma = M \Gamma_0 \quad . \quad (5.12)$$

The M active transversal modes are also called conductance channels. All the energy is dissipated at the metallic contacts/tube interfaces and the contact resistance, the lowest resistance a SWCNT can show, is equal to $1/2\Gamma_0 = 6.5k\Omega$. The conductance quantization was experimentally verified by immersing MWCNTs into liquid mercury[122]. In the presence of defects or impurities, the transmission probability is reduced and the conductance is not longer quantized. Due to the singular structure of SWCNTs, even in the presence

of defects, the free mean path and the conductance near the Fermi level are not greatly affected.

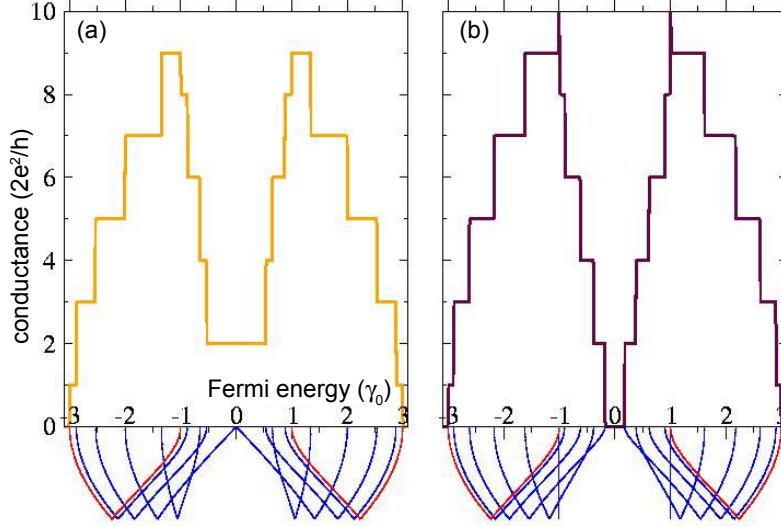


Figure 5.3: Conductance in terms of Fermi energy for pristine zigzag SWCNTs: (a) (9,0) and (b) (10,0). The metallic (9,0) shows two conductance channels, meanwhile the semiconducting (10,0) does not conduct near the Fermi level. Bottom panel depicts the energy dispersion with non and double degenerated bands in red and blue, respectively.

With the equations derived in the previous section 5.1.2 we now can calculate the conductance of a pristine and perfect SWCNT. Fig. 5.3 depicts the transport properties (top panel) of two zigzag SWCNTs. Not surprisingly, two conductance channels can be observed for the metallic (9,0) in Fig. 5.3 when remembering that the energy dispersion relation (bottom panel) of metallic SWCNTs has two bands crossing the Fermi level. Interestingly, for all metallic SWCNTs we obtain $M = 2$ conductance channels near the Fermi level. The semiconducting (10,0) tube shows no conductance channels up to energies of the first vHs. Non (double) degenerated bands contribute with one (two) conductance quantum Γ_0 .

5.2 Mechanical properties using a semi-quantical many-body potential

Single-walled carbon nanotubes are known to possess attractive practical mechanical and electronic characteristics. The extremely high Young's modulus has been experimentally confirmed[123–125] as predicted by theoretical studies[126–128], making SWCNTs one of the toughest materials known. With their high mechanical resistance, SWCNTs even outclass diamond in hardness and at the same time, their big elasticity allows great deformations without altering their crystal lattice structure. In this section we will derive the required theoretical tools to simulate some mechanical properties of the carbon systems, i.e. thermal stability as well as systems under uni-axial tensile load. First we give the theoretical recipe of the simulation method and go further into details in the second part.

(I) The Monte Carlo (MC) simulations are performed with the Metropolis algorithm[129, 130], using the canonical (NVT) or isothermal-isobaric (NPT) ensembles. In the NVT ensemble, a MC trial move consists in displacing an atom to a new position inside a small cube, which is centered at the original atomic position. On the other hand, in the NPT ensemble MC trial moves are related to atomic displacements and changes in the simulation box length. Adopting periodic boundary conditions one is restricted to simulation cells of constant volume in the NVT ensemble whereas it may vary in the NPT ensemble. The interactions between the carbon atoms are given by Tersoff empirical potentials[131–133].

The thermal stability simulations were done in the NPT ensemble with zero pressure. After the simulations reach equilibrium at 0K, the temperature is raised by consecutive steps of 50K, maintaining the system in quasi-equilibrium states. At each step the system is completely thermalized. The mechanical stability simulations were performed within the NVT ensemble. For a given temperature, the simulations begin with the corresponding equilibrium simulation cell size (L_0). After reaching equilibrium, the cell is elongated by ΔL so that a tensile strain is applied to the system. The strain is increased by consecutive steps ΔL of 0.2% or 1.0% and in general, 20,000 Monte Carlo steps are sufficient to reach equilibrium.

(II) We will now review the basic ideas and formula of a Monte-Carlo simulation of a system composed of N atoms. Each MC step consists of N following basic steps:

1. The energy U of a configuration of N atoms is calculated.
2. The position of one atom (NVT) and/or the system's box length (NPT) is varied arbitrarily in space.
3. The new energy and energy difference δU are calculated.
4. If the energy is lower, the trial move is accepted. If the new energy is higher, then a number between 0 and 1 is sorted. According to the Metropolis algorithm, the trial move is also accepted, if the sorted number is less than the Boltzmann factor $\exp(-\beta\delta U)$, where $\beta = 1/kT$.

To be more precise, in the NVT simulations the trial moves are accepted with a probability equal to $\min[1, e^{-\beta\delta U}]$, where δU is the variation of the potential energy caused by the atomic displacement. In the NPT simulations the acceptance probability is $\min[1, e^{-\beta\delta H}]$, where δH is related to the enthalpy change:

$$\delta H = \delta U + P(\delta V) - N\beta^{-1}\ln(V_i/V_f) ,$$

with V_i and V_f being the initial and final volume, respectively. Thus in the two cases, the simulations take in account the Gibbs free energies (NVT simulations) and enthalpy (NPT simulations). Nevertheless, when we analyze the simulation results we refer only to the potential energy U . This is reasonable because we never use the values of the energy to make any statistical mechanics calculations.

The total energy of the system is the sum of the energy of every atom, given by $U = \sum_i U_i = \frac{1}{2} \sum_{i \neq j} V_{ij}$. The carbon-carbon interaction energy V_{ij} is calculated using the empirical semiclassical interatomic potential introduced by Tersoff[131–133]. The Tersoff potential describes the energy of atomic bonds as a function of coordinate number, distance

and direction to the neighbor atoms. The following general form of the potential function is proposed as

$$V_{ij} = f_C(r_{ij}) \cdot \{f_R(r_{ij}) + b_{ij}f_A(r_{ij})\} \quad , \quad (5.13)$$

with the distance between atoms $r_{ij} = |\vec{r}_i - \vec{r}_j|$. The term f_C is just a smooth cut-off function limiting the range of the potential to $r = 2.1\text{\AA}$, reducing substantially computing time. The repulsive pair potential f_R includes the orthogonalization energy when atomic wave functions overlap. The attractive pair potential f_A is associated with bonding. They are given by Morse potentials[131]

$$\begin{aligned} f_R(r) &= A \exp(-\lambda_1 r) \\ f_A(r) &= -B \exp(-\lambda_2 r) \quad . \end{aligned} \quad (5.14)$$

All the dependencies on the bond order and angular direction are included in the term b_{ij} as:

$$\begin{aligned} b_{ij} &= (1 + \beta^n y_{ij}^n)^{-1/2n} \\ y_{ij} &= \sum_{k \neq i,j} f_C(r_{ik}) g(\theta_{ijk}) \\ g(\theta) &= 1 + \frac{c^2}{d^2} - \frac{c^2}{d^2 + (h - \cos \theta)^2} \quad , \end{aligned} \quad (5.15)$$

where θ_{ijk} is the angle between the bonds ij and ik . The fitted parameters for carbon are the following[131]:

$h = -0.57058$, $c = 38049$, $d = 4.3484$, $\beta = 1.5724 \times 10^{-7}$, $n = 0.72751$; $A = 1393.6\text{eV}$, $B = 346.74\text{eV}$, $\lambda_1 = 3.4879\text{\AA}$, $\lambda_2 = 2.2119\text{\AA}$. Applying this potential to the honeycomb graphene sheet, an energy minimum of -7.410eV/atom is obtained which is centered around $r = a_{cc} = 1.42\text{\AA}$ and $\theta \approx 120^\circ$.

This potential has been successfully used to reproduce elastic properties, phonons, defect energies, lattice constants and the migration barriers for different carbon allotropes like graphite and diamond. More recently, it has been extensively adopted in the description of carbon nanotubes[105, 134–139]. Although not being as accurate as quantum calculations (e.g. *ab initio* or density functional approaches), it has the tremendous advantage of being able to deal with systems composed of several thousand atoms, like the Y-junction rings and heterojunctions investigated in this thesis.

5.3 Environmental tight-binding description

We now can exploit the results obtained with the Monte Carlo method described in section 5.2 and use the final, stable atomic configuration to calculate the transport properties of the carbon systems. For deviations of the perfect, pristine SWCNT lattice, there are several approaches in the literature to include the atomic bond environment in the hopping integrals. Maiti *et al.* incorporate a bondlength-dependence in the Hamiltonian H_{ij} and the overlap matrices S_{ij} [140]. Yang *et al.* use the Harrison hopping parameter relation $t_{ij} = \gamma_0(a_{cc}/r_{ij})^2$ to obtain the electronic structure of strained SWCNTs[141]. Other authors include interatomic potentials similar to the presented in sec. 5.2 to acquire the

electronic properties of varied carbon systems[142–144].

In the investigated systems, the electrons are well localized in strong covalent bonds and thus, we choose a pair-like exponential bond length dependence to include the atomistic structure details into the calculation of the electronic structure. To take advantage of the bond environment information, we use the attractive part (eq. (5.14)) of the Tersoff potential $b_{ij} f_A(r) = -b_{ij} B \exp(-\lambda_2 r)$. The interaction radius is restricted to the cut-off sphere given by eq. (5.13), taking into account only first neighbors.

We suppose a parameterized scheme for the environment dependent hopping integrals (EDHI) with the following scaling:

$$t_{ij} = \gamma_0 \cdot \frac{b_{ij} f_A(r_{ij})}{b_{\text{prist}} f_A(r_{\text{prist}})} = \gamma_0 \cdot \frac{b_{ij}}{b_{\text{prist}}} \exp\{-\lambda_2(r_{ij} - r_{\text{prist}})\} \quad , \quad (5.16)$$

with $r_{\text{prist}} \approx a_{cc}$, depending on the tube diameter. This model goes beyond simple bond length scaling of the hopping parameter. If, e.g., three next-neighbor atoms are distanced by a_{cc} but having bond angles very distorted from the ideal triangular graphitic lattice, a smaller hopping parameter, scaled by $\frac{b_{ij}}{b_p(\theta=120^\circ)}$, is assumed.

This scheme naturally takes into account the structural deformations of the SWCNT systems and the creation of defects due to different atomic coordination numbers. As shown later on, this will be important to describe in a good approximation the electronic properties of the investigated systems, in particular at the bifurcation regions of the Y-junctions as well as at the heptagon/pentagon pairs of the heterojunctions.

5.4 Magnetic field effects

The study of the electronic response of a system under the influence of an external magnetic field is a very interesting physical problem. Several proposals for possible application of magnetic effects of carbon nanotube systems are currently studied. Bachtold *et al.* discovered a regular oscillation pattern in the resistance of MWCNTs under the influence of a magnetic field applied approximately along the tubes axis[17]. This oscillatory phenomenon in function of the penetrating magnetic flux has been already observed in cylinder shaped conductors[145] as well as mesoscopic semiconducting rings[146] and is known as the Aharonov-Bohm (AB) effect [147]. The magnetic field causes an electron wave phase shift of the partial waves encircling the conductor in opposite directions and thus interference when recombining. The electrical resistance in the weak localization regime has an oscillating contribution, known as the Altshuler-Aronov-Spivak effect, with the period of half a magnetic flux quantum ϕ_0 ($\phi_0 = h/e = 4.13 \times 10^{-15} Tm^2$).

Fig. 5.4 depicts the magnetoresistance dependence of about 30% of an individual MWCNT showing an oscillation period of $\approx 8T$. Reducing the temperatures freezes out scattering processes and increases the phase-coherence length, thus, leading to a more pronounced oscillation pattern. The weak localization resistance of a cylinder of radius r is periodically modulated with a magnetic-field period given by

$$\Delta B = \frac{h}{2e}/\pi r^2 = 658/r^2 nm^2 T \quad . \quad (5.17)$$

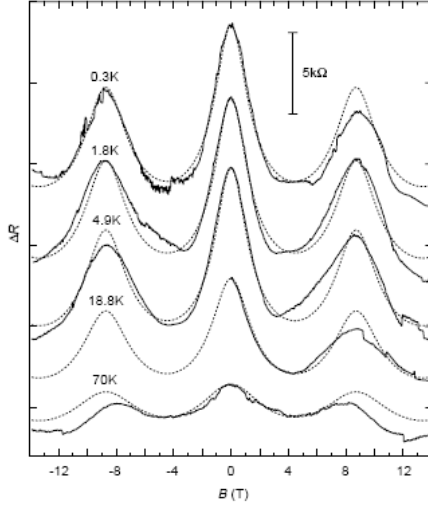


Figure 5.4: Aharonov-Bohm effect: Magnetoresistance at five different temperatures T measured for a MWNT in a parallel magnetic field B . At zero field the absolute values for the resistances are: 30.6, 30.1, 29.8, 25 and 21.4 k Ω from top to bottom.

In the experiment of Bachtold *et al.* this yields exactly the radius of outermost shell of the MWCNT. Nevertheless, there is some controversy about the oscillating periods reported, which may be contributed to the different experimental contacting processes as well as different MWCNT samples. According to 5.17, a magnetic field around thousand Tesla is needed to observe the AB effect in typical individual SWCNT samples which is not feasible in the today's laboratories. This was our motivation to suggest the usage of SWCNT Y-junction rings large enough to permit a magnetic flux entering the loop area and observe an AB oscillation pattern.

We will now introduce a tight-binding (TB) model which includes external magnetic fields. The effects of the field are incorporated in the real-space Green's function using the Peierls phase approximation[148]. As stated above, the external field shifts the electronic wave by a phase G depending on the vector potential $\vec{A} = -\frac{1}{2}\vec{r} \times \vec{B}$. This shift means a unitary cell size modulation dependent on the magnetic field. This approximation was proposed by Peierls to study the diamagnetic behavior of strong-correlated electrons and is valid only if the magnetic fields varies slowly in the range of the lattice constant. The Bloch expansion eq. (3.2) is now written as

$$\phi_j = \frac{1}{\sqrt{l}} \sum_{\vec{R}} e^{i\vec{k} \cdot \vec{R}} e^{ie/\hbar G_{\vec{R}}} \psi_j(\vec{r} - \vec{R}) \quad , \quad (5.18)$$

where the phase shift G is calculated as the integral of the vector potential along line \overline{Rr} :

$$G_{\vec{R}\vec{r}} = \int_{\vec{R}}^{\vec{r}} \vec{A}(\xi) \cdot d\xi \quad . \quad (5.19)$$

We will use the Coulomb gauge, $\nabla \cdot \vec{A} = 0$. The Hamiltonian including the crystal potential V and the magnetic field is written as

$$\hat{H} = \frac{(\vec{p} - e\vec{A})^2}{2m} + V(\vec{r}) \quad . \quad (5.20)$$

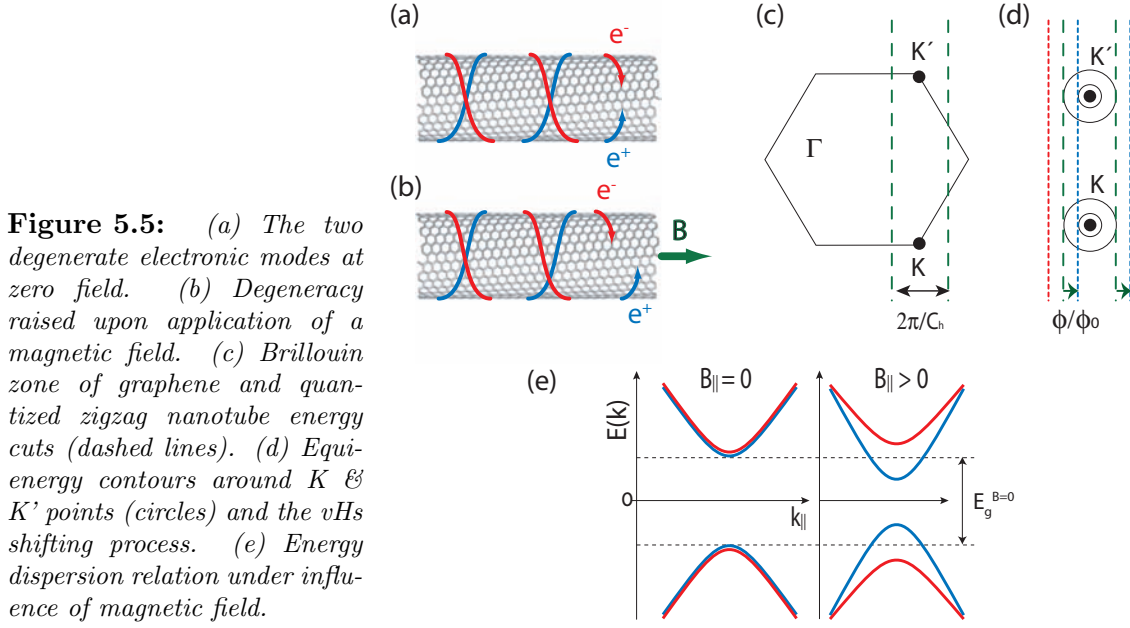


Figure 5.5: (a) The two degenerate electronic modes at zero field. (b) Degeneracy raised upon application of a magnetic field. (c) Brillouin zone of graphene and quantized zigzag nanotube energy cuts (dashed lines). (d) Equi-energy contours around K & K' points (circles) and the vHs shifting process. (e) Energy dispersion relation under influence of magnetic field.

Calculating the matrix element of the hopping integral of $\langle \phi | H | \phi \rangle$ using eq. (5.18) we obtain

$$H_{ij} = V_{ij} \exp(i e / \hbar \Delta G_{\vec{R}_i \vec{R}_j}) \quad . \quad (5.21)$$

Aharonov-Bohm effect

The Aharonov-Bohm effect manifests itself when a magnetic field is applied along a cylindrical conductor as, e.g. the nanotube in Fig. 3.4. The electrons moving along the surface suffer the Lorentz force and the electronic structure is perturbed. Using the same SWCNT supercell of section 3.3.1, the vector potential in this system configuration is written as

$$\vec{A} = \left(\frac{\Phi}{L}, 0 \right) \quad , \quad (5.22)$$

with $\Phi = \pi r^2 B$ the magnetic flux penetrating the cross-section of a tube with a circumference of $L = 2\pi r$. The phase factor $\Delta G_{\vec{R}_i \vec{R}_j}$ between two atoms located at \vec{R}_i and \vec{R}_j can be calculated using eq. (5.19):

$$\Delta G_{ij} = \frac{\Delta x}{L} \Phi \quad , \quad (5.23)$$

where $\Delta x = x_i - x_j$ is the distance of the two atoms along the circumference C . Using eq. (5.21), the response of the electronic structure to an external magnetic field can be calculated entirely in the real space by simple adopting the TB model introduced above.

The axial magnetic fields obliges the electrons to move in a screw-like manner along the nanotube, as shown schematically in Fig. 5.5(a,b). The resulting phase shift of the electrons e^- (blue) and e^+ (red) leads to interference effects manifesting the AB oscillation pattern. It can be described by a rigid band shift of $k_{\perp} \rightarrow k_{\perp} + \frac{2\pi}{C_h} \frac{\phi}{\phi_0}$, where ϕ/ϕ_0 defines the adimensional intensity of the applied field[149]. The magnetic flux rises the

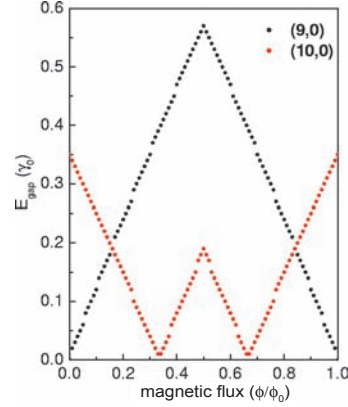


Figure 5.6: Energy gap evolution of the metallic (9,0) and semiconducting (10,0) SWCNTs under the influence of an axial magnetic flux.

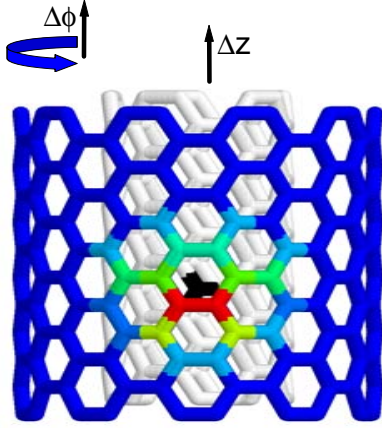


Figure 5.7: Schematic view of a piece of (5,5)@(10,10) DWCNT, showing the relative displacement between the intertube atomic positions along the axial direction (Δz) and in the azimuthal angle ($\Delta\phi$). The color scale refers to different (red high, blue low) intensities for the allowed interatomic hopping energies on the outer wall related to the black atom in the inner tube.

degeneracy of the unidimensional bands and each subband (and thus vHs) is modulated by this oscillating function. On zero field, the quantized zigzag SWCNT energy cuts (green dashed lines) belong to the same equi-energy regions [Fig. 5.5(c)]. Upon the influence of the magnetic flux, they are dislocated, rising the degeneracy and shifting the vHs [Fig. 5.5(d,e)]. Eventually they pass the K point and a transition from semiconducting to metallic nature is observed[18]. Augmenting the flux to an integer multiple of ϕ_0 , the electronic states return to their original position, retrieving the double degeneracy and characterizing the AB effect in CNTs.

The evolution of the energy gap for two zigzag tubes is depicted in Fig. 5.6. Upon augmenting the magnetic field, in the case of (9,0) a transition from metallic at $B = 0$ to semiconducting at $B > 0$ is observed. After one magnetic flux quantum, the gap is closed again, recovering the metallic state. In the (10,0) semiconducting case, the gap closes at multiple integers of $\frac{1}{3}$ and $\frac{2}{3}$ of ϕ/ϕ_0 . The gap evolution is strictly linear as a function of ϕ/ϕ_0 and is the same for all SWCNTs of different chiralities[149].

5.4.1 Application: DWCNTs in magnetic fields

As an example of the derived model, we state here some calculations of double wall carbon nanotubes (DWCNT) under the effects of external uni-axial magnetic fields. An increasing interest has been addressed to the synthesis and study of DWCNTs, motivated mainly by

the possibility they offer on triggering their mechanical, transport, and electronic properties. DWCNTs have been used as channels of field-effect transistors revealing singular transport properties. The semiconducting ones have been proved to exhibit ambipolar characteristics different from the p-type behavior of most of the as-produced SWCNTs devices[150]. DWCNTs may be achieved by peapod-derived methods[151], synthesized by pulsed arc discharge processes and low pressure catalytic CVD[94], among others. X-ray diffraction analysis of the structural transformation from SWCNTs to DWCNTs, via C_{60} peapods[152] determined the intertube spacing between inner and outer tubes as being $3.6 \pm 0.1 \text{ \AA}$, similar to the distance of 3.5 \AA for AB-stacked graphite[153]. Also, studies indicate that the tubes are loosely coupled to each other[154, 155]. Experiments indicate ballistic or quasi-ballistic transport in DWCNT and MWCNTs[156, 157]. The interwall interaction between the atoms of different walls has been usually assumed to decay exponentially with the interatomic distance in tight-binding approaches[158–162]. Previous theoretical works on commensurate DWCNTs have discussed the electronic structure of the coupled system based on symmetry arguments[163, 164]. Considering orientational disorder into the theoretical description, the aperture of an energy gap was observed.

A short piece of an armchair (5,5)@(10,10) structure is depicted in Fig. 5.7. The relative axial (Δz) and angular ($\Delta\phi$) distances between both the tubes are marked in the figure. We can take advantage of our real-space description and investigate how the relative positions of the inner and outer wall atoms affect the conductance of the DWCNT. The TB-Hamiltonian in eq. (5.1) is now extended to include the interwall contribution as:

$$H = e_0 \sum_{i,t} \mathbf{a}_{i,t}^\dagger \mathbf{a}_{i,t} + \gamma_o \sum_{i,j,t} (\mathbf{a}_{i,t}^\dagger \mathbf{a}_{j,t} + cc) + \sum_{i,j} \gamma_1(r_{ij})(\mathbf{a}_{i,1}^\dagger \mathbf{a}_{j,2} + cc) \quad , \quad (5.24)$$

where $r_{ij} = |\vec{r}_i - \vec{r}_j|$ gives the atomic distance between different i and j carbon atoms, and $t = 1, 2$ labels the two isolated tubes. The intershell coupling $\gamma_1(r_{ij})$ is assumed to scale as[161, 165, 166]

$$\gamma_1(r) = \gamma e^{-(r-d)/\delta} \quad , \quad (5.25)$$

where $\gamma = \gamma_o/8$, the damping factor $\delta = 0.45 \text{ \AA}$ and the intertube distance $d = 3.5 \text{ \AA}$ [165, 166]. The variations allowed for the interwall hopping energies γ_1 on the atoms of the outer tube are illustrated as the color map in Fig. 5.7: blue for low, red for high interactions. The reference atom of the inner tube is shown in black. This model allows continuous Δz displacements along the axial direction as well as azimuthal rotations, $\Delta\phi$, as indicated in Fig. 5.7. Both shifts are given in units of percentages of hexagons, taking as reference the graphitic-like stacking ($\Delta z = \Delta\Phi = 50\%$). We will now investigate how these relative movements affect the number of transport channels next to the Fermi level under the effect of an external uni-axial magnetic field.

The dependence of the LDOS and the conductance of a (5,5)@(10,10) DWCNT on the magnetic flux and Fermi energy is shown in Fig. 5.8 in a two-dimensional color map. Integer numbers of quantum conductance channels (0, 1, 2, and 3) are marked in the conductance maps. The (10,10) tube has roughly a twice as large radius and thus, the magnetic flux threading the bigger CNT is nearly four times the one of the smaller (5,5) tube. Consequently, the gap evolution in Fig. 5.6 will show a superposure of two independent magnetic field AB dependencies of both the SWCNTs composing the weakly coupled DWCNTs. The AB evolution is depicted in Fig. 5.8(a,b) for two different atomic configura-

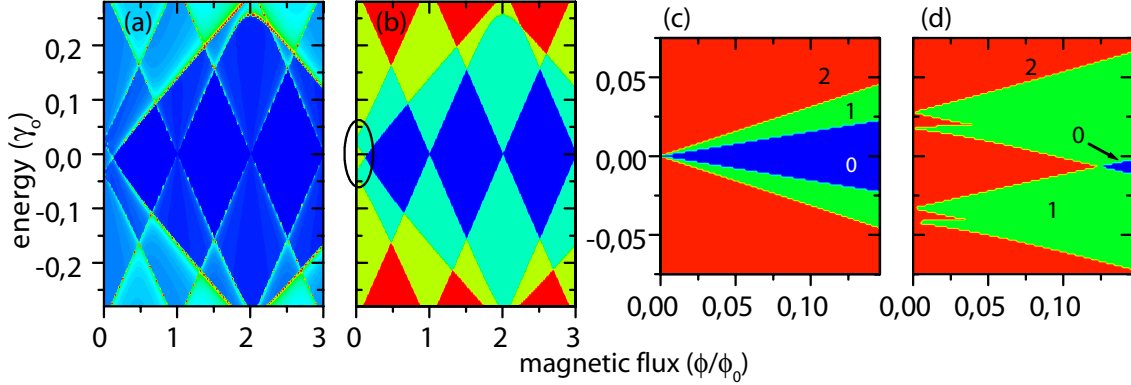


Figure 5.8: LDOS (a) and conductance (b) color maps for a $(5,5)@(10,10)$ DWCNT as function of the magnetic flux threading the outer tube (x -axis) and the Fermi energy (y -axis). Conductance maps in next to the Fermi level [as marked in (b)] for a disconnected (c) and interacting (d) DWCNT. A system with $\Delta z = \Delta\phi = 0\%$ (a) and graphite-like $\Delta z = \Delta\phi = 50\%$ (b-d) was used. The numbers indicate the corresponding transport channels.

rations. Although many other configurations have been explored, the conductance results do not exhibit a significant dependence on the intertube deviations Δz and $\Delta\phi$, in the plotted range of energy, as previously pointed by Tomanek[164].

The energy shifts of the van Hove singularities, as the field increases, are clearly exhibited by the red regions in the LDOS map in Fig. 5.8(a). Slight variations when compared with the harmonic gap evolution in Fig. 5.6 are observed for low magnetic fields. The first conductance suppression diamond (blue region) is smaller than the following ones. Nevertheless, the periodicity of the anew closed gap is again one magnetic flux quantum ϕ_0 . The situation when the magnetic field is turned on is highlighted in Fig. 5.8(c,d). Where the uncoupled system (c) shows the usual AB oscillation gap aperture, the DWCNT (d) with weakly coupled tubes has its degeneracy lift up resulting in four bands. Contrarily to the pristine case, the system retains its metallic nature, until a sufficient large magnetic field is able to open an energy gap. A small electron-hole asymmetry on the conductance results is present, destroying the complete energy-inversion symmetry, due to the hopping energy distribution associated with the atomic interactions between the two tubes. Upon rising the magnetic flux, the gap size of the interacting DWCNT approaches the non-interacting two tube system, indicating a more important contribution of the field than of the tube-tube interaction in this high field regime.

6 Y-Junction rings & quantum dots

Single wall carbon nanotubes could revolutionize the fabrication of novel nano-scale electronic devices. A variety of geometrical shapes, like X-, T-, and Y-junctions[12], quantum dots[21, 28], and crossing objects[167] are needed for a successful incorporation of SWCNTs into devices. Y-junctions made of carbon nanotubes have been considered as natural candidates for multichannel electronic devices at the nanoscale[11, 168, 169] and have been synthesized by chemical routes[170–172] or irradiation techniques[138, 173]. Experimental[174] and theoretical[14, 168] studies have shown that electrical transport across those junctions exhibits robust rectification properties, suggesting the possibility of using them as nanoscopic three-point transistors. Transport measurements and calculations on SWCNT tori revealed rich quantum interference phenomena under external magnetic fields[19, 30]. SWCNT superconducting quantum interference devices were recently realized showing the possibility of quantum confinement rising discrete energy levels of the quantum dot[175].

Section 2.3 already introduced some of the fascinating quantum interference effects present in SWCNT devices and motivated by these contributions, we propose a prototype of a ring-like interferometer made of SWCNTs, resembling two interconnected Y-junctions. The main results were published in several contributions[113, 114, 176–179]. The annular system may be used as a double-slit interferometer allowing a rich variety of quantum phenomena. In this chapter we will show the structural configurations of the Y-junctions, Y-junction rings (YJR) and quantum dots (QD), followed by a simulation of the mechanical and thermal stability. Then we will present the synthesis of YJRs and finally calculate the electronic and transport properties of ring-like and quantum dot structures.

6.1 Atomic structure of SWCNT YJRs

The ring-like structure can be idealized by the joining of two Y-junctions. We thus start with the description of a single three terminal junction. According to the Crespi rule, a specialization of Euler’s theorem for the polygons on the surface of a closed polyhedron of arbitrary number of holes, these systems feature six heptagons as topological defects of the regular honeycomb structure [14, 180]:

$$N_{\text{heptagons}} = 6 \cdot (N_{\text{terminals}} - 2) \quad . \quad (6.1)$$

Scuseria proposed a highly symmetric Y-junction (D_{3h}) with two heptagons in each branch[181], whereas Andriotis *et al.* introduced junctions with different symmetries[13, 14]. A general model to obtain arbitrary junctions based on geometric considerations was developed by Laszlo[182]. We propose a Y-junction with a symmetric arrangement of the topological defects in the bifurcation region. The six heptagons are shown in white colors in the atomic configuration scheme of Fig. 6.1(a), where the carbon atoms are located at the intersection points. By joining two such Y-junctions (YJ) one may build

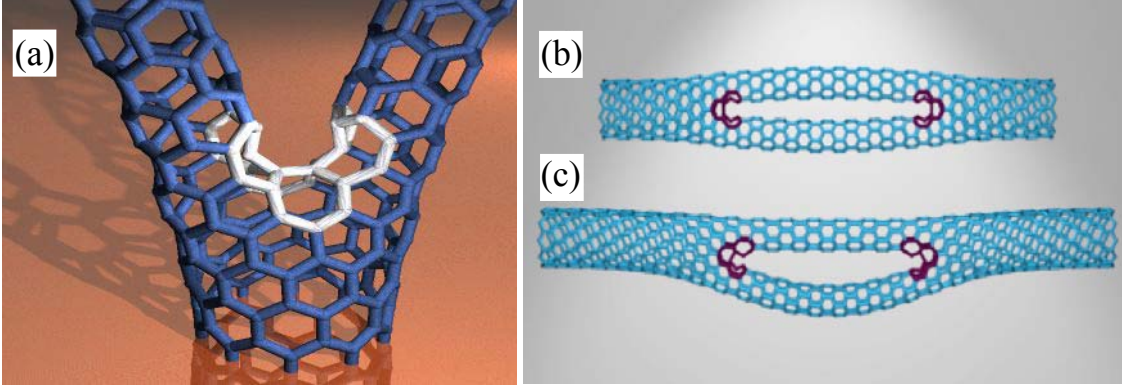


Figure 6.1: Snapshots of several relaxed configurations of small YJR at 0 K. (b) Symmetric semiconducting $10 \rightarrow 5_{16}/5_{16} \rightarrow 10$, (c) asymmetric $10 \rightarrow 5_{16}/5_{12} \rightarrow 10$, and (a) a close-up of the bifurcation region. The topological defect, six symmetrically arranged heptagons, are depicted by different colors.

nanotube-ring-like structures that come naturally connected to a pair of SWCNT leads, as depicted in Fig. 6.1(b,c). Such systems can be viewed as a pair of SWCNT molecular resistors that are arranged in parallel and one may explore quantum interference effects. Both structures are made out of two $(10,0) \rightarrow (5,0)/(5,0)$ YJs, where the $(10,0)$ tube characterizes the zigzag SWCNT lead, that bifurcates into two $(5,0)$ SWCNT arms. The notation used throughout this thesis to describe the (zigzag) YJRs is $S \rightarrow N_l/M_k \rightarrow S$, with l and k being the lengths, in units of pristine zigzag SWCNT unit cells, of the $(N,0)$ and $(M,0)$ branches. As we deal in this thesis mainly with $S = (18,0)$ stem leads, we will also use the short version N_l/M_k for this kind of YJR. If both branches have the same length ($N = M$), the YJR is called symmetric and asymmetric otherwise. To compare rings of different sizes we define an asymmetry coefficient given by $A = \frac{l-k}{l}$, with $l \geq k$. In Fig. 6.1(b) the symmetric ring ($A = 0$) consists of two $(5,0)$ branches of the same length of 16 layers ($24a_{cc}$). The asymmetric ring ($A = 0.25$) in Fig. 6.1(c) has different branch lengths with 16 and 12 layers ($18a_{cc}$). The real length L of the branch is given by $\frac{3}{2}la_{cc} \approx l \cdot 0.21nm$. Due to symmetry reason, $S = N + M$. Thus, the equilibrium atomic structure in Fig. 6.1(c), relaxed at 0K using the methods described in section 5.2 is called a $10 \rightarrow 5_{12}/5_{16} \rightarrow 10$ YJR. We shall show that under certain circumstances those YJ-ring structures act as a double-slit-like electron interferometer. Before we do so, however, it is important to find out if such idealized systems are structurally stable. For this purpose, we have performed Monte Carlo numerical simulations to obtain the mechanical strength and thermal stability.

We start by describing some properties of the YJRs in the absence of stress and

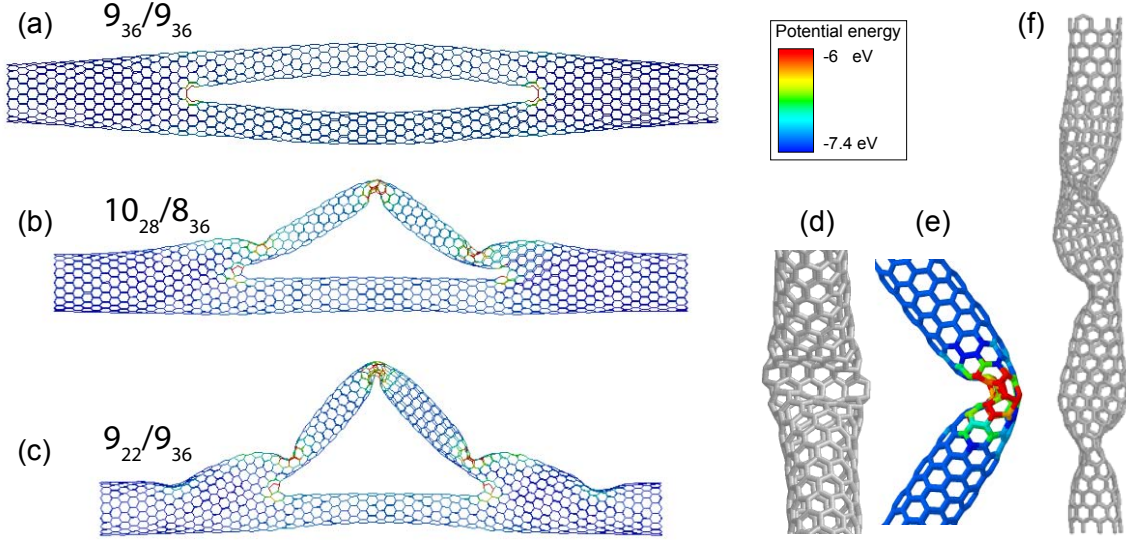


Figure 6.2: Equilibrium atomic configurations of rings with metallic leads ($S = 18$) at $0K$. (a) Symmetric metallic $9_{36}/9_{36}$, (b) asymmetric semiconducting $8_{28}/10_{36}$, and (c) asymmetric metallic $9_{22}/9_{36}$ YJRs. Close-up front (d) and side view (e) of the defect-free kink region of an asymmetric $9_{28}/9_{36}$ YJR. For comparison, (f) a buckled pristine $(9,0)$ under 10% compression. The color scale bar gives the values of the convoluted potential energy.

considering zero and room temperatures (300K). Experimental realization, thermal and mechanical stability of the rings are focused in the subsequent sections. The equilibrium atomic configurations of a $9_{36}/9_{36}$, $8_{28}/10_{36}$ and $9_{22}/9_{36}$ YJR structures convoluted with the potential energy maps are shown in Fig. 6.2, for zero temperature. The color scale bar gives the atomic potential energy. We will use this energy scale throughout the thesis and for the sake of simplicity will omit the scale bar plot subsequently, when not indicated otherwise. The branch lengths vary from 7.6 to 4.6nm and the simulated systems are composed of around 3000 atoms. For asymmetric YJRs, the systems relax forming a kink in the middle of the longer branch. No disturbances of the regular hexagonal lattice in the kink region is observed up to a certain bending magnitude (depending on asymmetry and tube diameter). Then, only few defects, mainly other polygons, tend to be formed. A configurational closeup of the defect-free kink area of a $9_{28}/9_{36}$ is depicted as front and side views in Fig. 6.2(d) and (e), respectively. Experimental evidences show that it is possible to obtain a high bending and buckling rate of the SWCNTs and further to form loops made of SWCNTs[183, 184]. In Fig. 6.2(f), a $(9,0)$ SWCNT is depicted under a compression rate of 10%. The kinks formed resemble the deformation in the larger branch in YJRs.

It is worth mentioning that by considering zigzag SWCNTs, each YJR-brace contains always pair numbers of layers, so that the geometric center of the branch lies at the bond center. As the system relaxes, the kink is formed at one of the carbon atoms rather than in the middle of the bond. So, the symmetry along the tube axis (σ_h) is lost, leading to a longitudinal asymmetry, as it can be seen in the longer branches of the systems in Fig. 6.2(b,c). For very asymmetric YJRs, quite deep depressions tend to form. They happen first in the ring branches, 6.2(b) and then also in the leads, Fig. 6.2(c). The

equilibrium potential energy maps indicate, that only in the bifurcation regions, and, for the asymmetric systems also in the kinks, see Fig. 6.2(e), the atomic energies are raised with respect to the overall, basically undisturbed pristine tube structure, indicating a stable system.

type	A	E_f (eV)	ΔL (Å)
$9_{36}/9_{36}$	0	3.9/heptagon	-
$9_{28}/9_{36}$	0.22	157	-15.5
$9_{26}/9_{36}$	0.28	190	-20.4
$9_{24}/9_{36}$	0.33	242	-24.7
$9_{22}/9_{36}$	0.39	254	-28.4
$9_{20}/9_{36}$	0.44	253	-33.3
$9_{18}/9_{36}$	0.5	257	-37.9
$9_{16}/9_{36}$	0.56	245	-39.6
$10_{36}/8_{36}$	0	5.1/heptagon	-
$10_{36}/8_{32}$	0.11	117	-5.6
$10_{36}/8_{30}$	0.17	145	-10.1
$10_{36}/8_{28}$	0.22	177	-15.2
$10_{32}/8_{36}$	0.11	122	-5.9
$10_{28}/8_{36}$	0.22	151	-15.7
$5_{16}/5_{16}$	0	3.6/heptagon	-
$5_{10}/5_{16}$	0.38	99	-11.3

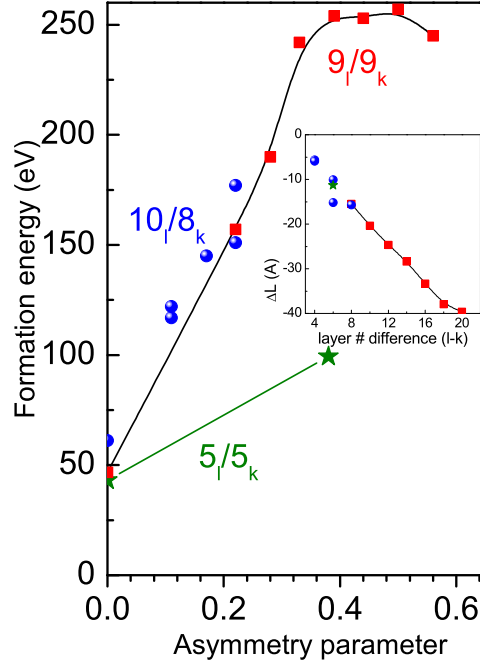


Figure 6.3: Left side: Table of Formation energies E_f (third column) for different YJR systems and corresponding asymmetry coefficient A (second column) at room temperature (300K). The length contraction ΔL is given in the fourth column. Right side: Figure of E_f as function of the asymmetry for $9_l/9_k$ (red), $10_l/8_k$ (blue) and small $5_l/5_k$ (green) YJRs. Inset depicts ΔL as function of the branch length difference $l - k$.

The formation energy of the ring, E_f , is defined as the total equilibrium energy of the rings minus the equilibrium energy of the corresponding pristine SWCNT system¹. The formation energies at room temperature are shown in the third column of table 6.3. Thus, the energy is listed as the total formation energy of the asymmetric YJR. As shown in atomic configuration sketch of the symmetric YJR in Fig. 6.2(a), only the heptagons have raised (red) energies, whereas the remaining structure has basically pristine tube energies. So, it is intuitive to define the formation energy per heptagon. This energy, between 3.6 and 5.1eV, is well above the thermal energies furnished to the systems. On the other hand, it is less than the formation energy of a single vacancy in graphite ($E_{vac} \sim 4 - 9$ eV/vac)[185–187] and SWCNTs ($E_{vac} \sim 6 - 7.1$ eV/vac, for tube diameters similar to ours)[187, 188].

¹For a YJR modeled by two (S,0) SWCNTs stems composed of N_S atoms which bifurcate into two branches, a (N,0) SWCNT with N_N atoms and a (M,0) SWCNT with N_M atoms, the reference energy of the pristine system is $N_S E_S + N_N E_N + N_M E_M$, where E_K is the energy per atom of an infinite pristine (K,0) nanotube.

When augmenting the system's asymmetry, other deformations and topological defects besides the heptagons tend to form with raised potential energies [see Fig. 6.2(b,c)]. Increasing the asymmetry coefficient leads to a linear increase of the formation energies up to $\sim 250eV$, as depicted in the corresponding Fig. 6.3. It means, as expected, that symmetric YJRs are more likely to be formed than asymmetric ones. Further augments in the ring asymmetry ($A > 0.35$), do not induce extra changes in the formation energies which remain in the same range (Fig. 6.3). The local potential energy distribution reveals that most of this energy augment is driven to the kink region whereas the atomic potential energies of the rest of the systems remain nearly unmodified [see energy potential color map in Fig. 6.2(b,c)]. One may, for instance, compare this situation to the behavior of bending a straw. After furnishing the energy necessary to form a kink, nearly no more energy is needed to bend the straw even further, see also Fig. 6.2(f). It is worth mentioning, that there are several hundreds atoms involved in the kink and depression formation and thus, the energy at these atoms is rarely raised more than one eV .

We also calculate the system's length dependence (ΔL) on the asymmetry coefficient. The results are depicted in the fourth column of table 6.3. This quantity is defined as the equilibrium length of the symmetric YJR systems minus the length of the asymmetric counterpart. One may note that upon increasing the asymmetry, the ring structures contract. The length contraction ΔL scales linear with the branch length difference, as demonstrated in the inset of Fig. 6.3. As expected, ΔL is of the order of $(k - l)$ layers $= (k - l) \cdot 2.1\text{\AA}$, indicating that the shorter branch remains nearly uncompressed in the equilibrium configuration.

6.2 Atomic configuration of SWCNT quantum dots

Treating the two branches of the YJR independently, we end up with a system resembling a quantum dot where the finite-sized branch with n layers [e.g. a $(9,0)_l$] is sandwiched between the leads [e.g. a $(18,0)$]. It is reasonable to expect some traces of the $18/9_l/18$ quantum dot behavior in the transport properties of a $9_l/9_l$ YJR when an electron travels through the structure. With this in mind, we will introduce now the atomic configuration of a newly proposed QDs.

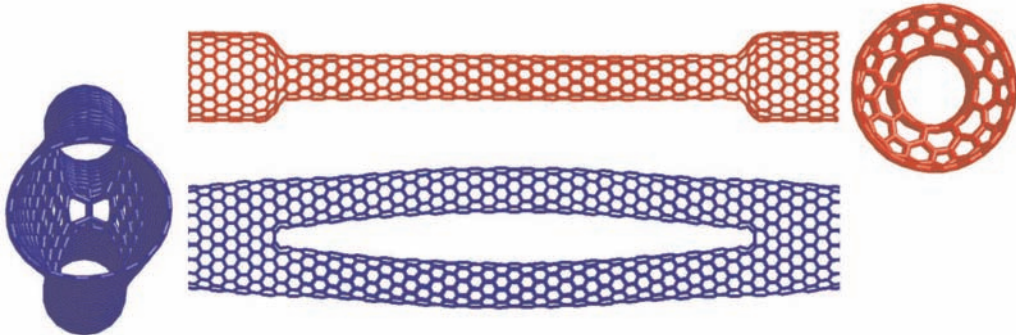


Figure 6.4: Side and cross-sectional view of the equilibrium atomic configurations of a $18 \rightarrow 9_{36} \rightarrow 18$ quantum dot (red) and a symmetric metallic $18 \rightarrow 9_{36}/9_{36} \rightarrow 18$ Y-junction ring (blue) at $0K$.

It is widely accepted, that defects cause deformations of the tube wall. Many intramolecular junctions were observed by Scanning Tunneling Microscopy and the topological defects proven to be stable at ambient conditions, among them heterojunctions[28] and Stone-Wales kink defects[189]. By introducing a pair of pentagon/heptagon (5-7 defect), a change in the diameter can be explained[190]. Including a pentagon in the system, the diameter start to diminish by one chiral index per intermediate tube layer and a heptagon recovers an unpertubated nanotube structure[191]. Nevertheless the change in the atomic configuration is very small, making it difficult to detect these defects in experiment. The presence of ad-dimers (C_2) on carbon nanotubes leads to a changed diameter and helicity in a short part of a tube[192]. Another way of constructing QDs is by including two 5-7 pair defects[193] or a complete ring of pentagons hooked-up by a ring of heptagons[30, 194]. They reported stable QDs, built by joining armchair to zigzag tubes, with a formation energy of $1.22eV/\text{defect}$. We followed the last proposal and present in Fig. 6.4 a new QD system (red) composed of three zigzag nanotubes joined by the inclusion of two rings of 5-7 defects[178]. A total of n 5-7 pair defects is needed to connect a $(n, 0)$ with a $(2n, 0)$ tube. Of course, the chiral index n cannot be arbitrarily high due to the increasing diameter differences between both nanotubes. A maximum radius difference without further tube wall deformations is expected around two tube layers, $\sim 4.9\text{\AA}$. The $18 \rightarrow 9_{36} \rightarrow 18$ QD presented in Fig. 6.4 has a radius mismatch of 3.5\AA and no additional defects or tube deformations are observed beside the two defect 5-7 rings. For comparison, a YJR (blue) with same size and length as well as a cross-sectional view of the equilibrium atomic configurations are also displayed in Fig. 6.4.

Although single heterojunctions with only a few defects have been proven to be stable, the proposed QD contains many topological defects: a ring of 9 pentagons followed by a ring of 9 heptagons, as shown in the cross-sectional view in Fig. 6.4. Topological defects are known to be weak points of the otherwise robust structure of carbon tubes, playing an important role on their stability. Due to the densely distributed topological defects present in the junctions, the mechanical properties of the structure proposed here are interesting to investigate. Surprisingly, the potential energy per atom of the relaxed QD structure is with $-7.27eV$ nearly as low as the one of a pristine $(9,0)$ with $-7.28eV$. Thus, the simulation indicates a very high stability with a formation energy of $60eV$ ($1.67eV$ per polygon). Considering the abrupt change in the diameter within only two tube layers, this formation energy is surprisingly low. We carried out also thermal stability investigations and the results indicate a stable structure to at least $1000K$.

6.3 Experimental realization of YJR

The very first experimental observations with the means of high resolution transmission electron microscopy (HRTEM) of the proposed ring-like structures were recently published in 2007[179]. The observation and reshaping method of YJR paths the way to a successful implementation in experiments exploring the predicted exciting electronic properties. Let us summarize the experimental details of the ring formation process. Samples of SWCNTs are generated using: (i) the arc discharge technique involving Ni-Y-graphite electrodes in a He atmosphere[195], and (ii) gas-phase thermal processes of carbon monoxide (disproportionation) at high pressures over Fe catalyst[196]. One mg of the nanotube material is

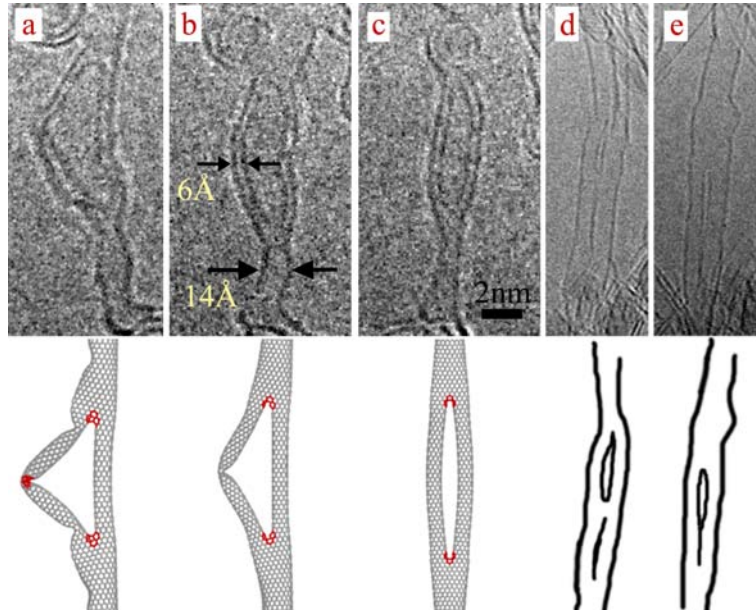


Figure 6.5: HRTEM images of (a-b) asymmetric and (c-e) symmetric ring-like SWCNT structures formed by electron-beam irradiation techniques at 800°C (1.25MeV electron beam energy). Images of reshaped structures are obtained after 30s (b) and 90s (c) of irradiation. Scale bar (2nm) holds for all images. Bottom: Atomic configurations of $9_m/9_n$ YJRs, with $n/m = 36/22$ (a), $36/28$ (b), and $36/36$ (c). Non-hexagonal defects are depicted in red. Structure schematics depicted in (d-e).

dispersed ultrasonically in 10ml ethanol for one minute and a few drops of the suspension were deposited onto Cu grids for high-voltage atomic resolution microscopy observations. The TEM (JEOL-ARM 1250) is located at the Max-Planck-Institut für Metallforschung in Stuttgart, Germany. The studies are performed at specimen temperatures of 800°C , using a Gatan heating stage and HRTEM images are recorded with a slow-scan CCD camera. The nanotube behavior is monitored under electron irradiation of standard imaging conditions (1.25MeV electron energy and beam intensity of ca. $10\text{A}/\text{cm}^2$).

Fig. 6.5(a) shows a typical HRTEM image of an as-produced structure resembling the asymmetric YJR presented in the lower panel. The diameter d of the constituent SWCNTs are approximately 6\AA for the branches and 14\AA for the stems and the length of the loop is around 18nm . Upon electron-beam irradiation, one clearly notices the onset of a merging process between the braces of the system, leading to a less asymmetric structure [Fig. 6.5(b)]. The reshaping process releases the potential energy contained in the compressed bigger branch, resulting in equal branch lengths. Thus, it is a one-way process. Indeed, after 90 seconds of irradiation we end up with the symmetric YJR displayed in Fig. 6.5(c). Another as-produced symmetric structure is shown in Fig. 6.5(d,e). Nevertheless, at this early experimental stage, the yield of the as-producible YJR is not high enough to implement ready devices. This merging process seems to be similar to the recently reported zipper-like fusion mechanism of the two arms of a Y-junction into a single tube[197]. Carbon atoms are knocked out of the tube walls by the intense electron-

beam irradiation. The high-temperature environment allows the remaining carbon atoms to anneal and reconstruct the sp^2 lattice, leading to an overall reshaping of the systems geometry[134, 138, 198]. Therefore, the reshaping process allows the production of ring-like SWCNT structures with defined symmetries upon electron beam irradiation at high temperatures in a controlled manner at relatively short periods of time.

6.4 Thermal Stability

To investigate the thermal stability of the YJRs, we performed Monte Carlo simulations described in section 5.2, adopting the Tersoff semiclassical interaction potential. The temperature is varied from zero to 6000K. During the experimental realization of the merging process, the nanotubes tend to diminish the diameter upon electron beam irradiation[173] or by electromigration[199]. Thus, it is important to compare the stability results of larger YJRs of the initial melting process with systems composed of smaller nanotubes.

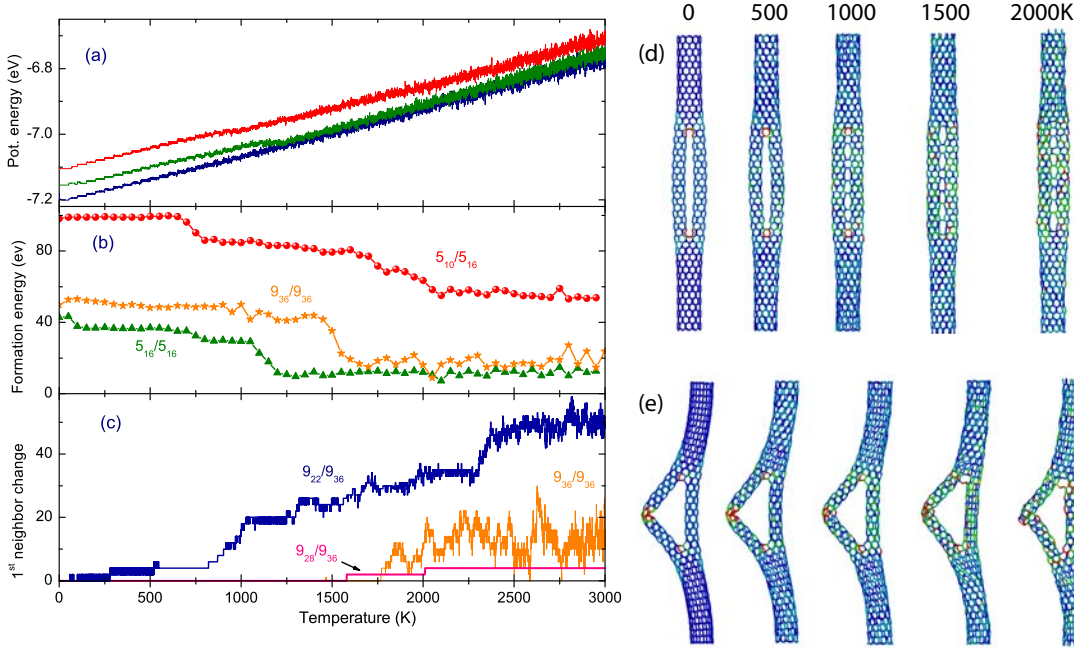


Figure 6.6: Temperature dependence of (a) average potential energy per atom and (b) formation energy of $10 \rightarrow 5/5 \rightarrow 10$ YJRs. Pristine SWCNT in blue, symmetric $5_{16}/5_{16}$ in green, $9_{36}/9_{36}$ in orange and asymmetric $5_{10}/5_{16}$ in red colors. (c) 1st neighbor change in bigger YJRs, as marked. Atomic configurations convoluted with the potential energy of the symmetric and asymmetric YJRs are shown in (d) and (e), respectively, corresponding to temperatures of 0, 500, ..., and 2000K.

Numerical simulations up to $T = 3000$ K for $10 \rightarrow 5/5 \rightarrow 10$ YJRs and the corresponding pristine nanotube counterparts $(5, 0)$ and $(10, 0)$, as well as some larger YJRs are presented in Fig. 6.6. After the simulation reaches equilibrium at 0K, the temperature is increased by consecutive steps of 50K maintaining the system in quasi-equilibrium states. At each step the system is completely relaxed. The average energy per atom and the structural formation energy as a function of temperature, are shown in Fig. 6.6(a) and

(b), respectively. The energy results for symmetric (arms measuring $24 a_{cc}$) and asymmetric ($15 a_{cc}$ and $24 a_{cc}$) YJRs are compared with each other and also with the corresponding averaged system composed of pristine (5,0)/(10,0) SWCNTs (see footnote on page 76). As expected, the average energy per atom increases whereas the formation energy decreases with temperature for all considered systems. The existence of energy plateaus indicates temperature ranges without major structural changes. A small decrease in the potential energy per atoms entails also a step in the formation energy, indicating the occurrence of a structural strain relaxation process. Nevertheless, the average energy for all systems investigated increases nearly linearly by $(1.4 \pm 0.1) \times 10^{-4} eV/K$. At high temperatures, the potential energies of the YJRs assimilate the one of the pristine counterparts. Up to the first plateau ($T_c \sim 700K$) there are no structural changes compared to the 'perfect' YJR configuration (Fig. 6.2), unless thermal atomic vibrations. Above a critical temperature, T_c , however, some important structural rearrangements do occur. This can be verified in Fig. 6.6(d,e), where the atomic configurations at $T = 0, 500, \dots$, and $2000K$ are presented in a potential energy scale map. In Fig. 6.6(e), we observe that the kink region of the asymmetric YJR forms localized defects only for higher temperatures. In the symmetric ring system in Fig. 6.6(d), due to thermal oscillations above T_c some atoms of the opposite branches occasionally approach each other, and the branches start to polymerize[114]. The polymerization process starts near the junctions and propagates to the middle of the arms.

The structural modifications can be visualized as the number of 1st neighbor changes in the YJR in Fig. 6.6(c). An increasing temperature dependence of the highly asymmetric structure $9_{22}/9_{36}$ (blue) is observed indicating the welding of the kink region upon raising the temperature. On the other hand, above the critical polymerization temperature, the first neighbors changes of the symmetric $9_{36}/9_{36}$ (orange) start to oscillate when the atoms of opposite branches approach each other and then separate again. For YJRs with an intermediate asymmetry, e.g. $9_{28}/9_{36}$ (pink), only a few vicinities are changed at elevated temperatures.

A close-up of the starting point of the polymerization is depicted in Fig. 6.7(a) at $T = 1000K$. The black balls represent four-fold coordinated carbon atoms which bind covalently during the polymerization process. Such a zipper-like process was already observed in Y-junctions experiments[138]. As no long-distance interactions are included in the interatomic potential used here, the critical temperatures for the symmetric YJRs are expected to be higher. These van-der-Waals like interactions tend to keep the braces separated at the graphite interplanar distance ($\sim 3.4\text{\AA}$), hindering the polymerization process. The value of T_c depends on the specific YJR geometry. For the bigger tube systems, we found a higher T_c equal to $1800K$ and $1650K$ for the symmetric $9_{36}/9_{36}$ and $10_{36}/8_{36}$ rings, respectively. Nevertheless, the formation energy dependence is very similar to the smaller tubes, as indicated in Fig. 6.6(b).

Coalescence of the branches is observed at very high temperatures ($> 4000K$) for small diameter tubes. In Fig. 6.7(b) a symmetric YJR is depicted at $5000K$. When the system with coalesced arms is taken back to room temperature, a nearly free pristine tube of the same diameter of the stem tube (10,0) is obtained in Fig. 6.7(c). Only polymerization and no coalescence up to carbon evaporation temperatures is noted in bigger diameter systems. It is worth mentioning, that the tube degradation and carbon evaporation temperatures, $\sim 6000K$ for an (18,0), obtained by employing the Tersoff potential

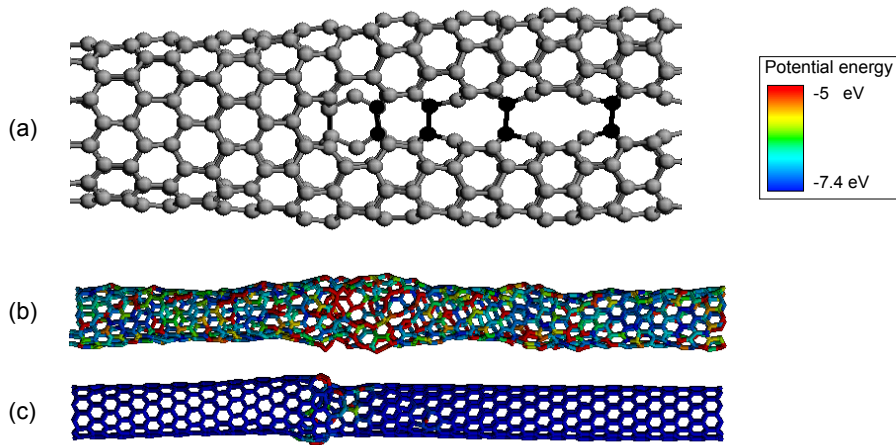


Figure 6.7: (a) Initial stage polymerization process with covalently connected branches at 1000K. Coalescence process of the arms of a small symmetric YJR (a) heated to 5000K and (b) cooled down to 0K. Convolutional potential energy/atom indicated by the scale bar.

are very much overestimated. The potential was developed to describe well carbon allotropes and fail up to a certain degree in the simulation of covalent bond rupture. Other groups which used adapted Tersoff potentials found a SWCNT thermal stability up to 2500°C[200, 201]. In experimental investigations, bundles of SWCNTs are stable up to 1600°C upon thermal treatment[202]. Others observed coalescence at 1800°C[201, 203] and tube wall corrugation between 1000-1700°C[204]. Above 2200°C, the bundles become unstable and transform into MWCNTs.

For asymmetric YJR, on the other hand, the structural rearrangements occurring above T_c are related to the formation of defects in the kink of the larger branch. For instance, $T_c = 1000K$ for a $9_{28}/9_{36}$ ring. High asymmetries, typically $A > 0.3$, lead to formation of different defects such as heptagon-pentagon pair defects. Mostly, higher order polygons are observed in the laterals of the kink. As a result, the critical temperatures decrease for higher asymmetries. At high temperatures, the kink region begin to weld and small YJR tend to rupture starting at the bifurcation areas (2200-3500°C). Also, we find that YJRs composed of arms with different radii, e.g. a $10/8$, are less stable than rings with branches of the same radius, like the double (9,0). The presence of a smaller tube diameter induces higher distortions at the junction areas, leading to lower critical temperatures and higher formation energies. Nevertheless, these values are of the same order and the defect formation processes are similar to the ones of the systems with same diameter branches. For small asymmetries like the $9_{28}/9_{36}$ ($A < 0.22$), indeed a kink is thermally not favorable and the defect formations at the kink region are not observed. Then, the larger branch is compressed, like depicted exemplarily in 6.2(c). The wide-open branches move back to a more parallel arrangement, but the branches remain configurationally separated by a distance higher than the short range of the potential. In this way, polymerization or coalescence processes do not happen as well. Suchlike, besides some few rearrangements at the junction area for temperatures higher than $T_c = 1500K$, these rings resist up to the disintegration temperature of a pristine nanotube.

Fig. 6.8 shows the relative length variation in comparison to the equilibrium length

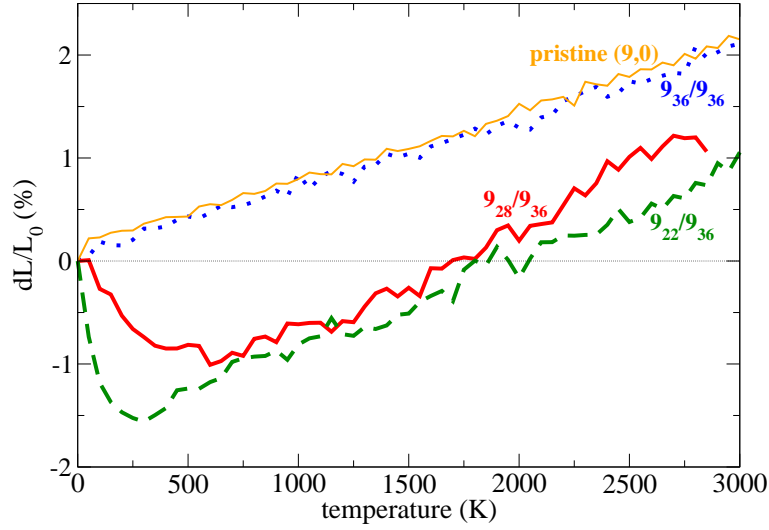


Figure 6.8: Length variation dL/L_0 (%) versus temperature for metallic $9_l/9_k$ Y-rings.

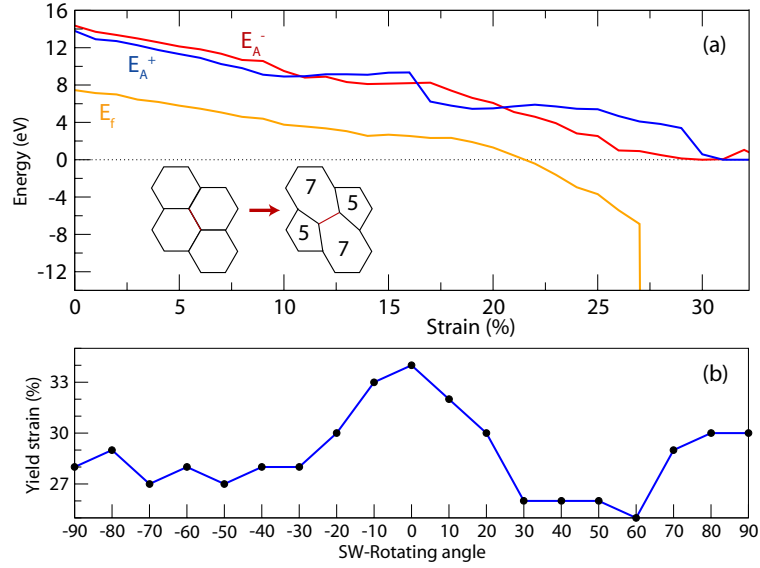
at $0K$ (L_o) as a function of temperature, $dL/L_o = (L - L_o)/L_o$. It can be seen that the symmetric ring $9_{36}/9_{36}$ (dotted blue) expands thermally just as the pristine counterpart (thin solid orange). The expansion coefficient is linear and values in both cases approximately $7 \times 10^{-6} \text{ }^\circ K^{-1}$. Experimental results of the thermal expansion in individual SWCNTs are not available. The studies of thermal treatments of SWCNT bundles indicate a negative thermal expansion up to $1600^\circ C$ [205, 206]. On the other hand, several theoretical models yielded positive thermal expansion coefficients[135, 136, 207] adopting similar interatomic potentials as we utilized. Interestingly, asymmetric YJRs present a negative thermal expansion coefficient up to quite high temperatures, as depicted in Fig. 6.8 for two asymmetric $9_l/9_k$ rings. Small diameter YJRs first contract in the same way, but the contraction temperature range is lower. For higher temperatures, all systems expand. Increasing the asymmetry leads to a contraction enhancement and a reduction in the corresponding temperature value of the maximum contraction temperature. Again, this contraction is due to the presence of the kink, which tend to dislocate away from the shorter branch for higher temperature, diminishing the system's length. The lateral strain in the kink region is increased for more asymmetric YJRs due to the negative thermal expansion and the length reduction ΔL (table 6.3).

Summing up, small and big YJRs show quite different thermal behaviors. Small diameter systems already consist of an atomic structure very distorted from a graphene sheet and are thus more sensitive to external changes. Consequently, we observe polymerization followed by coalescence for symmetric and rupture at the bifurcation for asymmetric YJRs. Bigger systems only show polymerization and no rupture.

6.5 Mechanical strength of YJRs

The details in the rupture process of pristine nanotubes are still a challenge from experimental and theoretical point of view. Several groups have investigated the yield strains,

Figure 6.9: (a) Stone-Wales defect formation E_f and activation barrier energy E_A of a pristine (18,0) under uniaxial strain at room temperature. The + and - sign defines the rotation of the red bond depicted in the inset. (b) Yield rupture strain vs. fixed bond rotation.



the microscopical details, and the formation of defects in CNTs[124, 127, 128, 208, 209]. The Young's modulus is reported in a range between some hundreds of GPa up to several TPa , which makes SWCNTs one of the toughest material known. Yet, it was not possible to define an accepted value for the critical load. However, it seems that the reason of the discrepancy in literature is mainly due to the different theoretical models and potentials adopted. Especially the rupture moment, when a covalent bond is breaking, is treated very differently among the available potentials. Keeping this in mind, we performed thorough stability simulations of the proposed systems and adopt a comparative study rather than considering absolute values. More precisely, we proceed comparing the breaking strain values of several simulation runs with the ones of their pristine SWCNT counterparts.

First, we carried out simulations of the systems under compression. All systems behave as the smallest constituent SWCNT and show subsequent buckling. The critical compression load of the first buckling appearance ($\sim 7\%$) is the same for YJRs and SWCNTs. Basically, the structures form a series of kink, as depicted exemplarily in Fig. 6.2(f) for a SWCNT under 10% compression. No changes in the hexagonal lattice are observed up to quite high values ($>30\%$) for all systems. So we can conclude that the structures are stable upon positive load.

It is well known, that the strain transfer velocity of the external force to pristine SWCNTs is quite important in theoretical simulations. For high stress transfers and low temperatures, the tubes show a more brittle behavior with high yield strains. The opening of higher order polygon is observed, which propagates rapidly around the SWCNT axis leading to the tube fracture. Slowly augmenting the system dimension with higher temperatures leads to a ductile behavior[210]. It is claimed that prior to the rupture of pristine SWCNTs, in the ductile regime, one or several Stone-Wales (SW) 5-7-7-5 defects are formed to relax the uploaded strain[211]. These pentagon-heptagon defects are formed when rotating the red bond in the inset of Fig. 6.9(a) by 90° . The activation energies E_A is defined as the maximum energy value when rotating the bond by 90° , calculated with the Tersoff potential adopted. At zero strain, the barriers are quite high, around 13 eV

for an (18,0) SWCNT at room temperature, as depicted in Fig. 6.9(a). However, the energies decrease considerably for higher strains. For example, at 22% strain, it becomes $E_f = 0$ and $E_A \sim 5\text{eV}$. For further higher strains, a negative formation energy is observed and a spontaneous formation of the 5-7-7-5 defect could occur. However, the high barrier activation energies inhibit SW defect formations when using this potential. By fixing the bond rotation angles at values in between $\pm 90^\circ$, as shown in Fig. 6.9(b), we observe yield strain maxima at the SW angles ($\pm 90^\circ$) as well as for the unrotated bond, indicating a more stable system. However, the simulation results always show the opening of higher order polygons prior to rupture (like the one depicted in Fig. 6.10) and no SW defects in the temperature range between 0 and 800K.

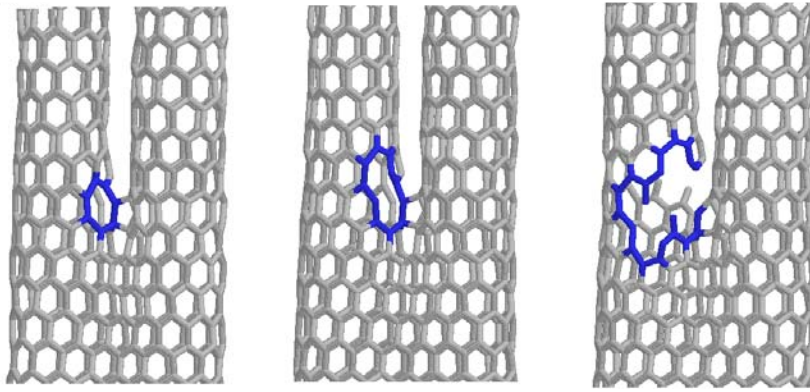


Figure 6.10: Closeups of the defect formations in YJRs at 800K. Heptagon opening process of a strained symmetric $9_{36}/9_{36}$. Blue marked atoms show from left to right: equilibrium heptagon, one bond broken and several bonds broken, leading finally to the total rupture of the system.

Contrarily to pristine SWCNTs, the rupture process of YJRs is not very sensitive to the stress transfer velocity and fracture details. As a general result one finds that the rupture always takes place at the topological defects at the junction area, as depicted by the blue marked atoms in Fig. 6.10. For tensile strains higher than the critical strain, s_c , bonds start to brake and the heptagons open further, followed by a very quick fracturing of the whole junction area. In this way, the results indicate that YJRs always behave as brittle systems.

In Fig. 6.11(a) we show the average energies per atom as a function of the strain for a symmetric YJR and a pristine (9,0) SWCNT. The yield strain, identified by the abrupt energy decay seen in the figure, is of the same order for both structures, indicating that the symmetric YJR is mechanically almost as stable as the pristine tube. On the other hand, asymmetric YJRs, in general, break for smaller strains. The rupture of these rings occur in a two steps process, first the smaller leg breaks followed by the larger one. In Fig. 6.11(b) we illustrate the particular case of the $9_{28}/9_{36}$ YJR for 300 and 800K. As expected, the larger the temperature, the lower the maximal strain. Due to the thermal vibrations upon load, rupture of carbon bonds and the following quick polygon opening takes place much earlier for higher temperatures. In all cases, the systems obey Hooke's law (quadratical energy dependence) up to very high strain values. The yield strain s_c results are summarized in table 6.1 for several metallic and semiconducting, symmetric as well as asymmetric YJRs. Symmetric rings and pristine tubes present yield strains of

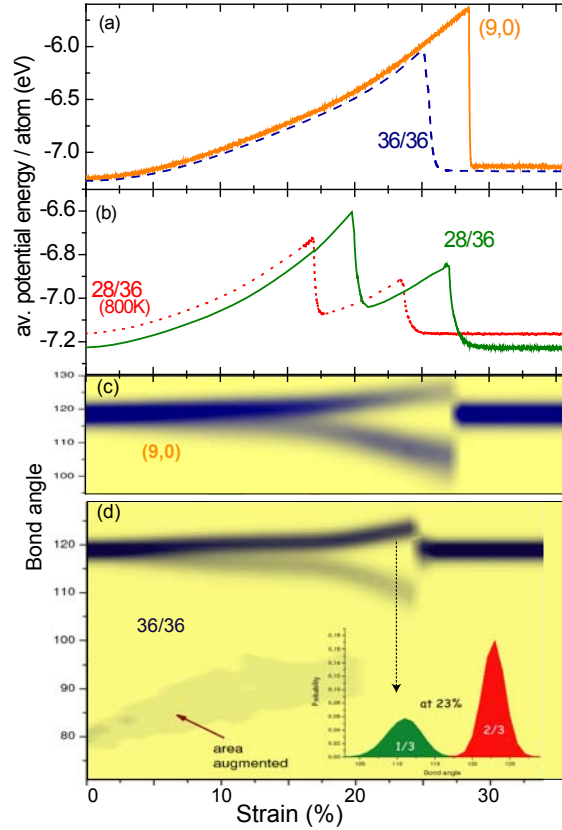


Figure 6.11: Atomic energies as a function of strain. (a) $9_{36}/9_{36}$ symmetric YJR at $T = 300K$ compared to the pristine $(9,0)$ SWCNT. (b) Typical asymmetric $(9_{28}/9_{36})$ YJR at $T = 300$ and $800K$. Bond angle distribution of $(9,0)$ (c) and $9_{36}/9_{36}$ (d). Inset depicts a cut at 23% strain as indicated by the dotted line.

the same order indicating that the symmetric version of the proposed YJR is almost as stable as the pristine ones. The critical load decreases drastically when increasing the asymmetry.

It is worth mentioning that the initial system length can be quite small for very asymmetric YJRs. In these systems the larger branch is highly compressed with lateral relaxation and kink formations due to the force exerted by the smaller branch. Elongation of the system leads to the breaking of the smaller arm and the system relaxes upon further stress until obtaining the equilibrium length of the longer arm. During this period, no strain is applied to this branch. As a result, the value of the yield strain s_c of the longer branch can be arbitrarily high, just reflecting the asymmetry of the YJR and cannot be taken as an assignment for the overall stability of the system. For example, the rupture value of the second arm of a $9_{22}/9_{36}$ YJR, shown in table 6.1, is found to be as high as 40.4%.

The bond angle distribution of a pristine SWCNT $(9,0)$ and a symmetric $9_{36}/9_{36}$ YJR is depicted in Fig. 6.11(c) and (d), respectively. In both cases, a spread on the bond angle distribution is observed upon strain. When remembering the zigzag SWCNT crystal structure, it is clear, that upon elongation, two angles get more obtuse and one more

type	$s_c(300K)$		$s_c(800K)$	
	1 st	2 nd leg	1 st	2 nd leg
pure (9,0)	28.4	-	27.4	-
$9_{36}/9_{36}$	25.0	-	23.6	-
$9_{28}/9_{36}$	20.0	26.8	16.8	23.2
$9_{22}/9_{36}$	16.6	40.4	15.2	36.8
$10_{36}/8_{36}$	23.0	-	20.3	-
$10_{28}/8_{36}$	19.4	27.0	17.6	23.8
$10_{36}/8_{28}$	18.2	28.4	15.8	23.8

Table 6.1: Yield strain s_c for pristine SWCNTs and different YJRs at $T = 300$ and $800K$.

acute. This is reflected in the inset of Fig. 6.11(d), where the integrated bond distribution areas at 23% tensile strain result in 1/3 and 2/3 percentage of angles smaller and higher than the optimal angle, respectively. The dark region in the 10 times augmented area in Fig. 6.11(d) indicates the non-optimal angles of the topological defects. After the system rupture, the bond angles naturally recover the optimal value, beside some dangling bonds. Both systems show a very similar behavior, indicating again the similarity of symmetric YJR and pristine nanotubes.

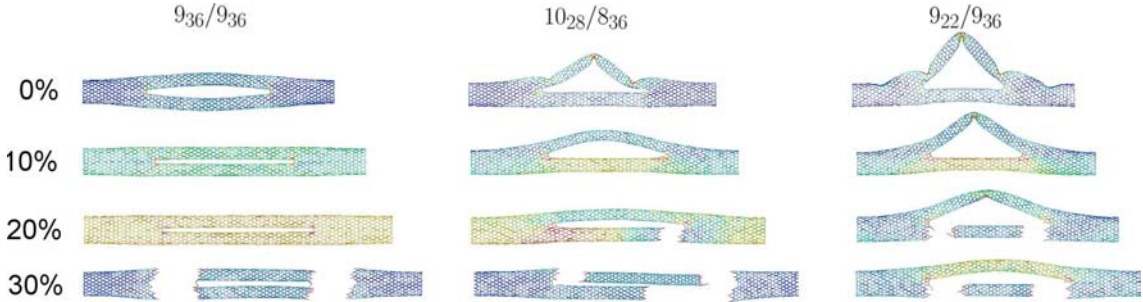


Figure 6.12: Snapshots of several atomic configurations at 300K for (a) symmetric metallic $9_{36}/9_{36}$, (b) asymmetric semiconducting $10_{28}/8_{36}$, and (c) asymmetric metallic $9_{22}/9_{36}$ under load of 0, 10, 20, and 30%.

The microscopical details of the fracture processes at 300K of all the discussed YJR systems are shown in Fig. 6.12. The atomic configurations for several strain rates (0, 10, 20 and 30%) are depicted in each column. The color map indicates the potential energies of the carbon bonds (between -7.4 and $-6eV$, see Fig. 6.2). All unstrained systems have low energy bonds [blue] with some higher energy bonds in the defective regions at the junction areas and the kinks. Augmenting the strain leads to higher bond energies in the whole system for the symmetric YJR until rupture [green and orange regions] and a following relaxation [blue] with high energetic dangling bonds at the fracture area [red]. The simulation results depicted in the first column of Fig. 6.12, show a fracture process with all four branches ruptured. Due to the thermal vibrations, we also found systems with three (e.g. as shown in second column) or only two branches broken. Statistically,

fracture processes with both arms ruptured at the same junction are the most likely one (around 50% of the simulations). As discussed above, in asymmetric YJRs, the strain is first loaded nearly entirely upon the smaller branch (second row of Fig. 6.12). After the rupture of this arm, the larger branch is albeit not under tension (blue colors in third row) until new load and following fracture. Smaller YJRs such as the $10 \rightarrow 5/5 \rightarrow 10$ exhibit similar results as compared to the bigger ones. The same defect formation processes and configurational arrangements are found. The yield strains are lower, but of the same order of the bigger rings. Summing up, in all the cases studied the values are comparable with the pristine SWCNT counterparts, indicating very high stabilities of YJRs.

6.6 Electronic properties

After demonstrating the feasibility of realization of Y-junction rings and quantum dots we now investigate the electronic properties of these systems. We expect destructive interference of the electron waves traveling along the two arms of YJRs and will address the correlation with characteristic sizes of the ring structure. For the sake of simplicity, we first adopt the constant hopping integral approach, derived in chapter 5.

6.6.1 Strictly one-dimensional ring

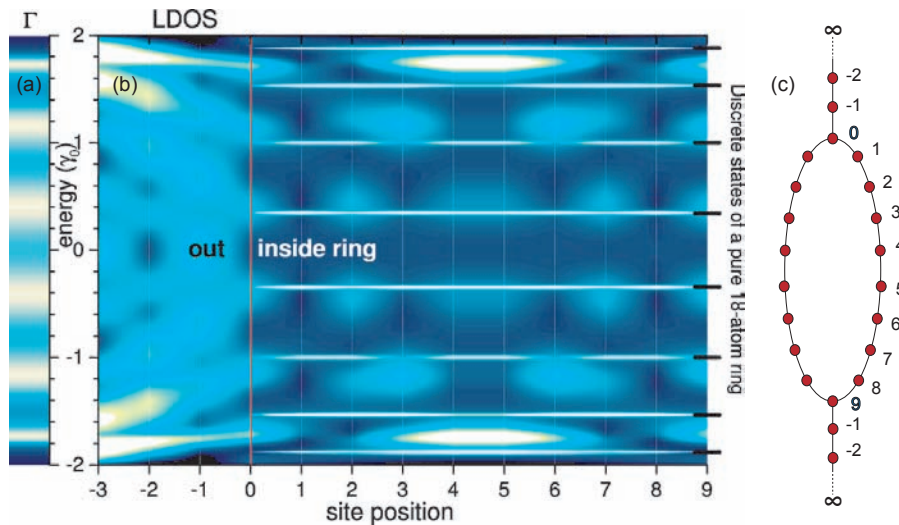


Figure 6.13: (a) Conductance and (b) LDOS as functions of Fermi energy and atomic position for a 1D ring composed of 18 atoms as depicted in (c). The ring is connected to a pair of semi-infinite chains at sites 0 and 9. Sites -3, -2, and -1 relate to lead atoms. Brighter colors correspond to higher values.

Before calculating the electronic properties of YJRs, it is instructive to present the main effects of quantum interferences in an equivalent one-dimensional chain model, composed of a loop connected to a pair of semi-infinite leads, as schematized in Fig. 6.13(c). The LDOS results at the atomic sites labeled by 0-9 of a symmetric 18-atom ring are

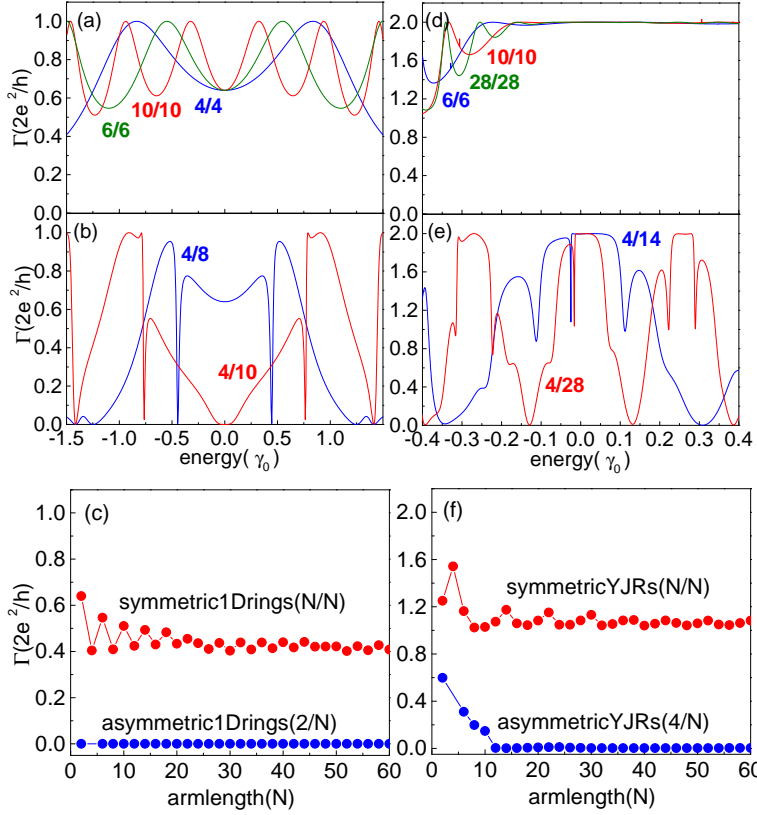


Figure 6.14: Conductance dependence on the Fermi energy for the 1D-ring model in (a,b) and for $12 \rightarrow 6_l/6_k \rightarrow 12$ YJRs in (d,e), considering symmetric and asymmetric configurations, respectively. Minimum conductance values for a 1D ring (c) and YJR (f), as a function of one branch length.

depicted in Fig. 6.13(b). The lead sites are labeled by $-1, -2, -3, \dots$. The LDOS intensity is shown by a 2D scale plot where brighter colors corresponds to higher values. One clearly notices that the LDOS exhibits symmetrical oscillatory behaviors both as functions of energy and ring atomic position. The two branches can be viewed as part of a Fabry-Perot resonator and the resulting electronic interference effects resemble the Fabry-Perot oscillation presented in the inset of Fig. 2.4. However, those symmetry features may be partially or totally lost for asymmetric rings, depending on the parity of the arms. Localized peaks with high LDOS values at certain energy values are superposed over the smooth oscillations. As expected, these peaks coincide with the eigenvalues of a corresponding pure 18 atom 1D ring, depicted by bold tick marks in the right y -axis of Fig. 6.13(b). The conductance of the system is shown in Fig. 6.13(a). It illustrates that near the Fermi-level ($E_F = 0$), the transport maxima occur for energies around the localized LDOS peaks. Now we will discuss with more details the electronic properties of rings made of SWCNTs.

6.6.2 General electronic properties of YJR

First we study metallic $12 \rightarrow 6_l/6_k \rightarrow 12$ YJRs. Quantum interference phenomena are discussed according to symmetric and asymmetric configurations. The conductance for various path-size combinations are presented on the right side of Fig. 6.14(d-f), restricted to an energy window where the pristine (12,0) SWCNT has only two ballistic channels. The 1D model calculations are also displayed for comparison on the left side Fig. 6.14(a-c).

All the results exhibit a well defined oscillation pattern with the corresponding periods being driven by the inverse of the branch size.

The conductance results of symmetric 1D rings and YJRs, shown in Fig. 6.14(a,d), exhibit just smooth oscillations with no complete destructive quantum interferences in this energy range, resembling the behavior found for a single $12 \rightarrow 6/6$ Y-junction[113]. The reduction here is caused by the multiple Fabry-Perot-like reflections at the bifurcation interfaces. One should note that, independently of the size of the symmetric loop, the conductance is not completely destroyed as a consequence of the constructive superposition of the electronic wave functions along the two equal quantum paths. Moreover, the minimum conductance value for symmetric rings systems is always around half of the lead's value (one for a chain and two for a SWCNT). This means, that in the 1D ring, the transport drops maximal to half a channel and in YJRs to one channel, independently of the arm length, as summarized in Fig. 6.14(c,f).

On the other hand, high transport reductions and even suppressions are obtained in asymmetric structures, a zero conductance is always found for particular energy values for high asymmetry coefficients [Fig. 6.14(b,e)]. This is a clear evidence of destructive quantum interference effects associated with the two distinct paths the electrons may take as they travel across the ring structure. As a consequence, an energy range with total transport suppression can always be found in both YJR (for $N > 10$) and 1D ring systems [Fig. 6.14(c,f)]. Thus, through geometrical configuration settings, YJRs may be absolutely conducting or isolating, highlighting their use as perfect rectification transistor.

Comparative results for the conductance and the total DOS are presented in Fig. 6.15 for metallic $9_l/9_k$ YJRs [6.15(a,b)] and for semiconducting $10_l/8_k$ YJRs in (d,e). The LDOS of the pristine tubes are also plotted in (c,f) for comparison. The DOS of symmetric metallic YJRs Fig. 6.15(a) present a mainly constant nonzero metallic plateau with sharp isolated peaks superposed, marking the characteristic discrete nature of the localized states of finite carbon toroidal structures[116]. This picture resembles the corresponding symmetric 1D ring counterpart discussed in Fig. 6.13. Destructive electronic wave interferences as well as a large ballistic regime of two transport channels around the Fermi level can be observed. This clearly emphasizes the possibility of using carbon nanotube rings as nanoscaled switching devices. For the asymmetric YJRs, the DOS peaks get smeared out as the asymmetry between the two paths increases, see Fig. 6.15(b). Whereas for symmetric YJRs the sharp DOS peaks are not correlated with conductance features[212], in asymmetric systems pronounced transport reductions occur at elevated DOS values.

When considering the environment dependent (EDHI) approach, the electronic properties change considerable. The observed conductance oscillations using the EDHI scheme (blue curve), are more pronounced as compared to those obtained via CHI calculations (red). Due to the varying hopping energies, more phase modulations of the electronic waves are induced leading to more transport reductions. When adopting the EDHI approach, reminiscent metallic state DOS contributions are found inside the (10,0) gap correlated with finite conductance values (marked by arrows), as illustrated in Fig. 6.15(d-e). We can distinguish two types of electronic states: delocalized (stars) and localized defect states. The extended state may be induced by the structural relaxing process, leading to quantum delocalization phenomena, which allows electronic transport for energies close to the (10,0) band edges. In contrast, localized defect states are observed near the bifurcations and kink regions, as will be shown further on. Due to tunneling processes via these defects,

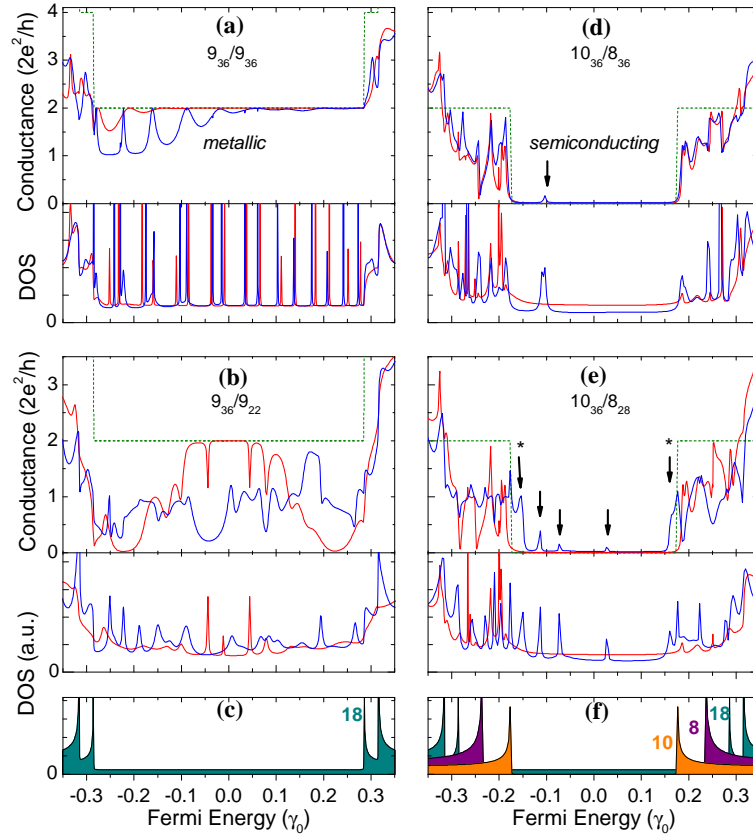


Figure 6.15: Conductance and total density of states as functions of energy for (a) symmetric $9_{36}/9_{36}$ and (b) asymmetric $9_{36}/9_{22}$ metallic rings, as well as (d) symmetric $10_{36}/8_{36}$ and (e) asymmetric $10_{36}/8_{28}$ semiconducting ones. Blue and red curves are for EDHI and CHI model calculations, respectively. Green dashed lines depict the conductance of the pristine constituent SWCNTs. Their DOS is shown in (c,f).

the effective YJR-brace barrier diminishes, leading to finite conductance values inside the semiconducting gap.

6.6.3 Standing wave formation in YJRs

We will now have a closer look on the formation of the conductance oscillation due to quantum interference effects. Interesting insights can be obtained by calculating the DOS at all the atoms in the ring as a function of energy. In Fig. 6.16(a) a typical LDOS map of a metallic $9_{36}/9_{36}$ ring is depicted. The LDOS is averaged over a single ring layer and labeled by the indices on the x -axis. The bifurcation regions, labeled by the layer indices 0 and 36 can be easily determined due to the high LDOS caused by defective interface states at the junction region. The LDOS of one of the two braces of the annular region is shown in between them and the LDOS of the (18,0) stem to the left and right. Near the Fermi-energy, well-defined narrow LDOS peaks are obtained as depicted in more detail further on in Fig. 6.20(c). Interestingly, these toroidal peaks terminate with the entrance of the first (18,0) vHs. Evidence of standing wave formation are highlighted through the

LDOS contour plots in Fig. 6.16(a). They are a consequence of two counter-propagating waves interfering constructively at the injection point. High values of the LDOS are represented by red regions. The evolution of the LDOS, layer by layer, may be used as

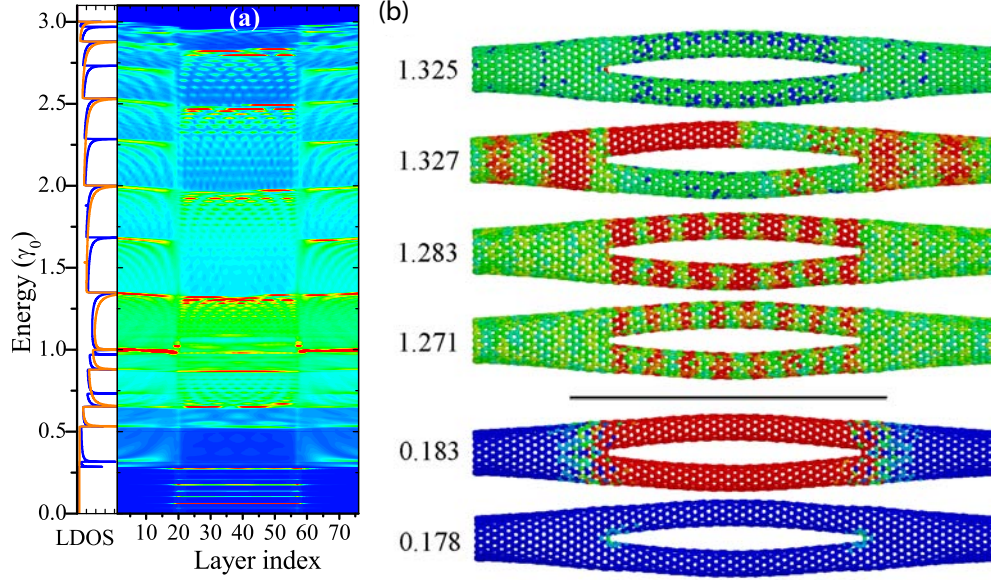


Figure 6.16: LDOS energy contour plot in the EDHI approach of a symmetric metallic $9_{36}/9_{36}$ as function of the ring layer index and energy. On laterals, the LDOS of the pristine constituent tubes $(18,0)$ [orange] and $(9,0)$ [blue] are shown. The energies for the atomic structure maps (b) convoluted with the LDOS are indicated on the left side in units of γ_0 .

a description of the electron wave characteristics inside the structure. Some remarkable features observed in this analysis are the electronic wave-function reflections in the left and right $(18,0)$ stem taking place exactly at both Y-bifurcations and leading to typical oscillatory LDOS patterns around the van Hove singularity (vHs) energies of the isolated tubes $(18,0)$, shown at the left panel of Fig. 6.16(a). For the ring region, a well defined sequence of standing waves appears each time one passes through the energy corresponding to a new vHs of the $(9,0)$ tube ($d=7\text{\AA}$). Note that these modes do not contribute to the transport through the ring system. The oscillation periods of the standing wave may be inferred from these results. We plot in Fig. 6.16(b) some structure maps at particular energy values, corresponding to typical standing waves and toroidal features. From top to bottom we observe first a structure without any evidence of correlated LDOS/atom features. The three subsequent YJRs illustrate the appearance of standing electronic waves of 1^{st} , 7^{th} and 8^{th} order. Due to the horizontal symmetry plane loss in zigzag YJRs, an asymmetry in the first order wave can be observed when adopting the EDHI approach. Furthermore, the low order waves exhibit a quite messy behavior because they turned out to be more sensitive to slight local symmetry changes caused by bonding environment taken into account in the EDHI approach. The higher order waves, indeed show very well defined oscillations.

As discussed before, at the energy region close to $E_F = 0$ sharp peaks appear in the LDOS. The last two YJR structure maps, at energy values very close together and within

this region, show the non- and appearance of an LDOS peak extended over the whole ring region as well as a couple of layer inside the stem. This supports our assumption of the toroidal nature of the nanosystems when analyzing the results shown in Fig. 6.15(a). Furthermore, the energy separations of these peaks (see also Fig. 6.20(c) with more details) correspond to the energy eigenvalue separation of a pure torus built by approximately 80 zigzag layers[21], demonstrating unambiguously the rich ring-like quantum interference effects.

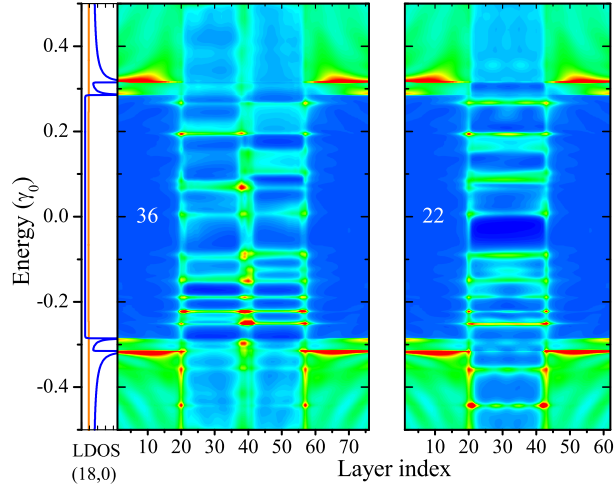


Figure 6.17: LDOS map of an asymmetric metallic $9_{36}/9_{22}$ YJR near the Fermi level using the EDHI scheme. Left panel depicts the constituent pristine SWCNT LDOS of $(18,0)$ as blue and $(9,0)$ as orange curves.

Thorough investigations are also performed on investigation of asymmetric YJRs. As expected, destructive interferences are manifested in asymmetric rings. LDOS maps of both braces of a metallic $9_{36}/9_{22}$ ring are illustrated in Fig. 6.17 adopting the EDHI. Differently to the symmetric example, the LDOS peaks found inside the rings are smoothed out reflecting clearly the loss of a quasi-perfect annular geometry of the nanoring. In the 22-layered brace, as expected, less resonant states than in the larger branch are found. When using the environment dependent description, kink defect states are present in the middle of the 36-layered brace [Fig. 6.17(a)], compare also with the atomic structure in Fig. 6.2(c). These defect states split the resonance cavity into two, as may be inferred from the different numbers of LDOS peaks in each part of the brace.

We now turn to the analysis of symmetric semiconducting YJRs. Beside the asymmetry due to the different branch diameters, the annular part is now composed of semiconducting tubes. The LDOS maps of both braces of a $10_{36}/8_{36}$ YJR, as a function of the energy, are displayed in Fig. 6.18. The LDOS evolution can be taken to identify the origins of the raised DOS and conductance through the system [Fig. 6.15(d,e)] as being interface and defect states. For instance, the white arrows highlight the localized defect states near both bifurcations, resulting in the finite conductance value marked by the arrow in Fig. 6.15(d). The formation of standing waves inside the two arms is also evident. Again, the entrance of standing waves is observed exactly at the corresponding vHs

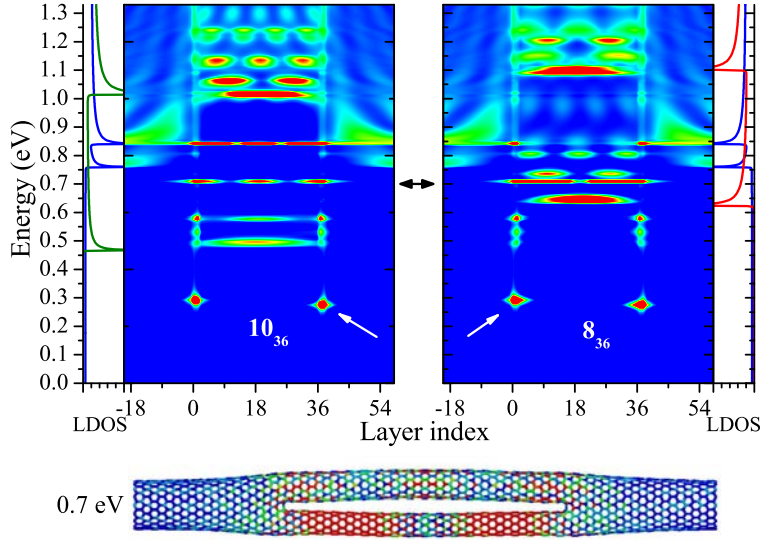
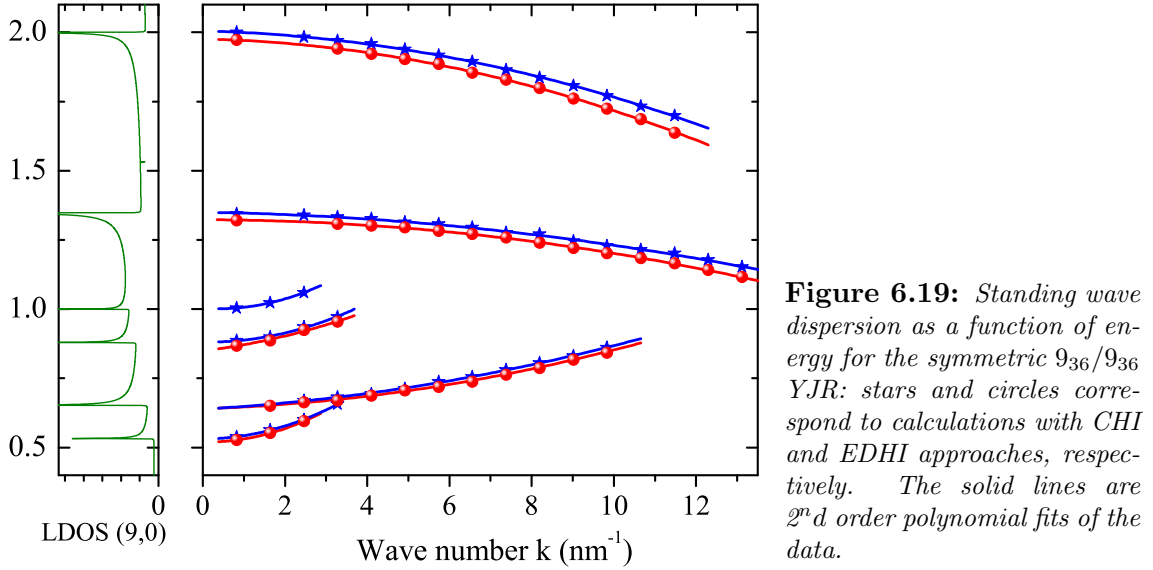


Figure 6.18: LDOS map of a symmetric semiconducting $10_{36}/8_{36}$ ring for energies next to the Fermi level. The laterals show the LDOS of the respective constituent pristine tubes, $(18,0)$ [blue], $(10,0)$ [green, left], and $(8,0)$ [red, right]. Lower panel: atomic structure map at the energy marked by the black arrow.

energies of the constituent SWCNTs of the system (stems and ring), with no correlation in between (see laterals). Thus, the appearance and quadratic dispersion of the standing wave modes occur independently in both the loop branches. This is highlighted in the atomic structure map in the lower panel of Fig. 6.18 corresponding to a quasi-standing wave state exhibiting different numbers of nodes along each one of the branch paths. This demonstrates that standing waves formed within such ring-like structures are very robust upon configurational changes.

Associating the LDOS with the square of the wave functions, the oscillation periods and the corresponding wave number, k , of the standing waves are calculated. The wave number is given by $k_j = j \cdot 2\pi/L$, with L denoting the arm length, and j the order of the standing wave. The dependence of the wave number with energy is shown in Fig. 6.19 for the EDHI (circles) and CHI (stars) approaches. The explicit correspondence between the standing-wave numbers and the isolated tube LDOS, shown in the left panel of the figure, is remarkable. Exactly at the pristine tube vHs energies a first order standing wave appears ($j=1$). At the vHs, the derivative of the energy dispersion relation vanishes, corresponding to a zero group velocity and thus the appearance of standing waves. Subsequently, the standing waves disperse inside the LDOS tail to higher order standing waves. Using the EDHI approach, one could observe a slight downshift of the energies when compared to CHI, but contrarily to the conductance, both schemes result in quite similar global behaviors. The eigenenergies of the standing waves are separated by several hundred meV and disperse quadratically. A second order polynomial fits the standing wave dispersion perfectly, as indicated by the fitted lines in Fig. 6.19. The small eigenenergies differences and the sub-nanometer resolved localization of the LDOS maxima along the ring brace raise the possibility of using the YJR as a nanoscale tunable electronic switching device



by different couplings to attached objects. In the next section, we will discuss in more detail the origin of the standing wave appearance.

6.6.4 Standing wave formation in quantum dots

The quadratic dispersion of the standing wave modes in Fig. 6.19 resembles the electronic properties of quantum dots. Thus, we carried out a thorough comparative study of the LDOS behavior in the corresponding finite-sized quantum dot presented in Fig. 6.4. A detailed comparative view at both the LDOS evolution of a $18 \rightarrow 9_{36}$ quantum dot and a $18 \rightarrow 9_{36}/9_{36} \rightarrow 18$ YJR is presented in the contour plots Fig. 6.20(a,b) and (c,d), respectively. The resemblance of the well defined sequence of standing waves of both systems in Fig. 6.20(b,d) is remarkable. Both systems show the same quadratical wave mode dispersion into the finite density of states tail with similar wave mode energy separations. Thus, we may infer that the formation and dispersion of these modes are driven mainly by a QD-like property. Although the electronic wave sense a quite different QD-junction when compared to the YJR-bifurcation when traveling through the structure (see cross-sectional view of Fig. 6.4), the standing wave evolution is almost entirely independent of the different QD termination.

Near the Fermi-energy [Fig. 6.20(a,c)], a different behavior of both systems is observed. A close-up of the as-described well-defined narrow LDOS peaks of the YJR is presented in Fig. 6.20(c). On the other hand, the QD still exhibits a series of standing waves as shown in Fig. 6.20(a). The differences in the behavior of both nanostructures are depicted in more details in Fig. 6.20(e,f) for particular energy cuts, as marked by arrows. Harmonic oscillations are found for QDs which are extended over the whole dot region, exhibiting slightly raised LDOS (green, red) when compared to the featureless energy regions in between (blue). In contrast, localized states near the Fermi level are found only in the YJR structure. These ring-like peak features have a dozens of times higher LDOS extended over the whole loop branch (red), as compared to the YJR plateau (blue). The differences can also be visualized in the atomic structures convoluted with the LDOS in the top

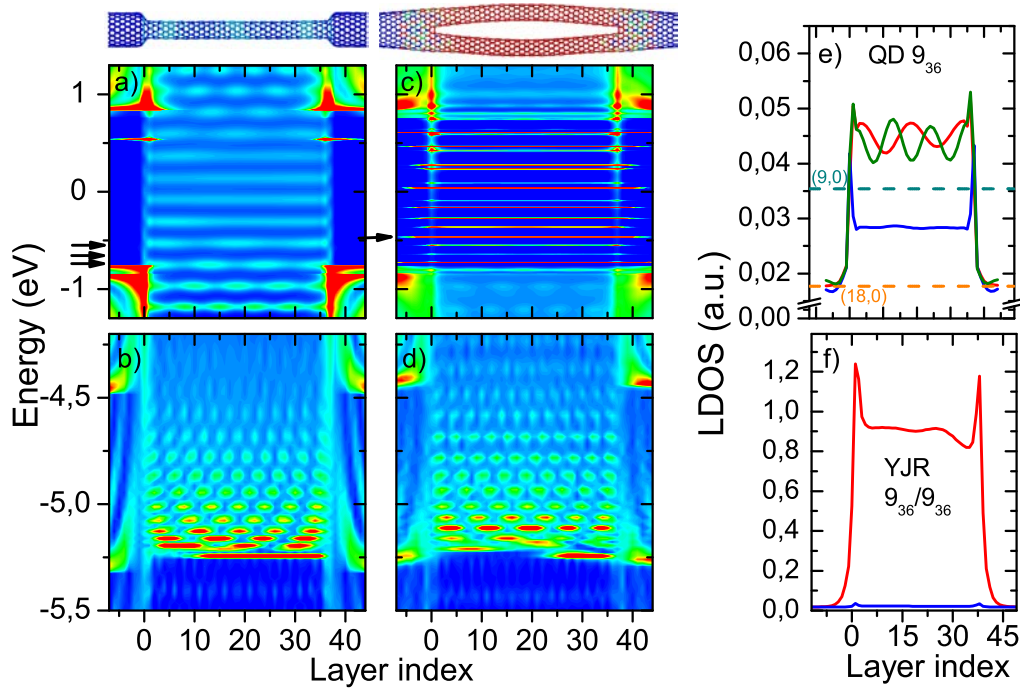
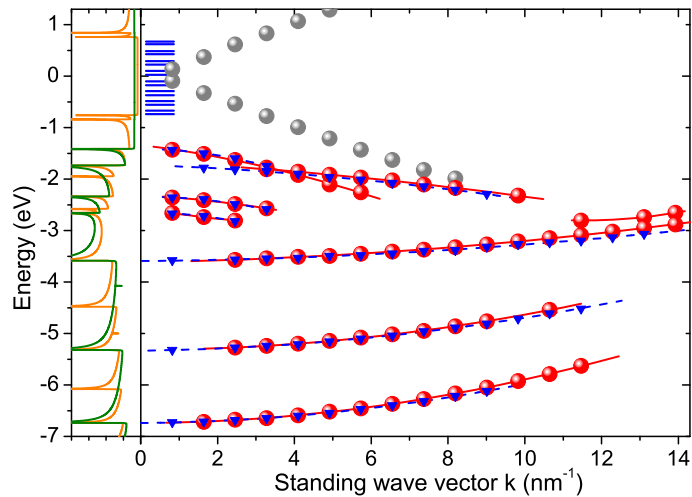


Figure 6.20: LDOS energy contour plots of a 9_{36} quantum dot (a,b) and a metallic $9_{36}/9_{36}$ ring (c,d) adopting the EDHI approach. LDOS evolution (e) along a quantum dot as marked by arrows in (a). Dashed lines indicate the LDOS plateau of the pristine constituent SWCNTs. (f) A typical ring-like peak (-170meV , red) and the metallic plateau (-175meV , blue).

panels, where a third order standing wave mode appears in the QD map and, on the other hand, an extended LDOS peak in the YJR.

Figure 6.21: Standing wave dispersion relation; triangles and spheres correspond to YJR and QD, respectively. The solid lines correspond to 2nd order polynomial fits of the data. Harmonic Fabry-Perot-like QD LDOS oscillations (gray spheres) and unique Y junction ring-like peaks (blue bars) are depicted near the Fermi level. The CHI approach is adopted



The explicit correspondence of the resulting quadratic dispersion relations of the QD (red spheres) and YJR (blue triangles) in Fig. 6.21 is remarkable. For the sake of simplicity we adopted the CHI approach. The low-energy YJR peaks terminating with the entrance

of the first (18,0) vHs and the smooth QD oscillations extending to higher energies are also depicted as blue bars and gray spheres, respectively. We thus conclude, that the high energy standing wave evolution has a purely QD origin, whereas the low energy region features are quite different and rich of quantum interference effects.

6.6.5 Fabry-Perot oscillations

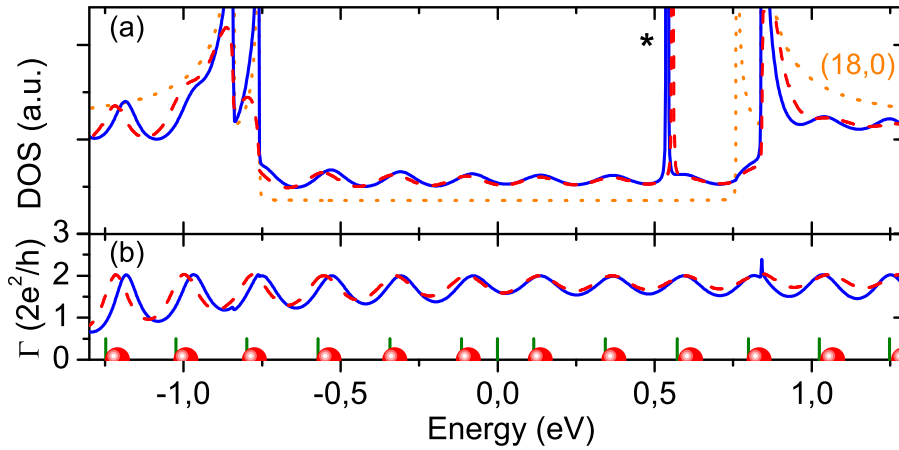


Figure 6.22: DOS and conductance Γ of a $18 \rightarrow 9_{36}$ quantum dot near the Fermi level. Blue solid and red dashed curves correspond to the EDHI and CHI approaches, respectively. Dotted orange curve shows the LDOS of the pristine (18,0) tube. The red spheres mark the energy of the standing wave modes, whereas the green bars the eigenvalues of a finite (9,0) with 36 layers.

Finally we discuss in Fig. 6.22 the transport calculation results of the QD. Comparative results for the total DOS of the system as well as the conductance are presented in Fig. 6.22(a) and (b), respectively. Very interestingly, a finite DOS as well as finite conductance Γ are observed near the Fermi level, contrarily to other proposed dots formed by a mixture of tubes of distinct chiralities demonstrating the appearance of a conductance gap[30, 194]. Our proposed QD as well as those cited QD systems have a finite LDOS near the Fermi level, so a transport suppression due to a LDOS gap caused by the defect region can be ruled out. This points to a symmetry origin of the conductance suppression in armchair/zigzag junctions[193]. Both zigzag SWCNTs composing our proposed QD $(2n, 0) \rightarrow (n, 0)_k \rightarrow (2n, 0)$ have an n -fold symmetry axis. When the two tubes are matched to form the junction, n pentagon-heptagon pairs are introduced at the interface, which itself has n -fold rotational symmetry. Therefore, the matched junction is invariant under rotations by $2\pi/n$. The two bands touching the Fermi-level are the ones with the quantum numbers $q = 2n/3$ and $q = 4n/3$. Thus, in a $(2n, 0) \rightarrow (n, 0)$ heterojunction, both energy bands have the same angular momenta and rotational symmetries. Consequently, no total reflection of the electron wave occurs at the junction interface, as it is the case of the reported dots in reference [30, 194].

The system shows a finite conductance with harmonic oscillations between one and two channels. Furthermore, a sharp environment independent LDOS peak without contribution to the transport is found around 0.55eV (star in Fig. 6.22) and is identified as

an extended interface state in Fig. 6.20(a). The observed standing waves spread smoothly over the dot region, differently to the sharp ring-like LDOS peaks of YJRs near the Fermi level. These extended oscillating modes (red spheres) contribute to the formation of broadened peaks in the DOS exhibiting a smooth oscillatory behavior completely correlated with the conductance. The harmonic periodicity is demonstrated by the linear dependence of the oscillation maxima as depicted by the gray spheres in Fig. 6.21. This Fabry-Perot like interference effect was expected due to the finite channel size, see discussion in section 2.3.3. Indeed, the discrete eigenvalues of a finite (9,0) quantum well are indicated as green bars and identify these low-energy standing wave modes as a reminiscence of the 36-layered quantum well where multiple reflections at the junction interface lead to the observed DOS and conductance oscillations.

7 Transport measurements

In this chapter we will present the first, preliminary transport results of SWCNT based devices fabricated entirely in the IFW. As described in chapter 4, the tubes are grown from pre-defined catalyst islands by CVD on a highly doped silicon substrate capped by a thick thermally grown silicon dioxide layer and contacted via electron beam lithography, see Fig. 7.1(a). The ready sample is then quickly characterized in a sample probe station with gold needles (*Karl Suss*), as shown in Fig. 7.1(b). With the probe station, electrode pads down to $10 \times 10 \mu\text{m}^2$ can be contacted. The device is mounted on a common chip carrier as depicted in Fig. 7.1(c) and bonded with thin gold wires to the bond pads of the carrier, Fig. 7.1(d). The carrier is mounted in the cryostat sample holder and ready to be inserted into a helium dewar, see further on Fig. 7.7(a).

7.1 Room temperature transport measurements of SWCNT devices

Each chip consists of 25 devices with a total of 100 electrodes in a four-terminal configuration as shown in Fig. 7.1(a). For a fast processing, the two-terminal resistance of each device is determined in a sample probe station. Frequently, we obtain 1 to 4 tubes contacted in parallel. Thus, most of the as-fabricated devices show metallic behaviors at zero gate voltage. We choose a constant current setup to measure the V/I characteristics. At room temperatures the curves are basically linear with slopes $\Gamma = dI/dV$ ranging from 4...0.1 conductance quanta ($\Gamma_0 = 2e^2/h$). Typical two-terminal room-temperature measurements of the current as function of the bias voltage V_{ds} are depicted in Fig. 7.2(a). Linear fits (solid lines) of the featureless data (symbols) give resistances between a few and several hundred $k\Omega$. The device resistances of some devices are merged in the histogram in Fig. 7.2(b). The fraction of single tube devices is highlighted by the red bars. The number of devices are summed up in ranges of the resistance quantum $\rho_0 = h/2e^2 = 13k\Omega$ and the histogram shows that in most cases we obtain nearly transparent contacts. Most single tube devices have conductances between 0.5 and $1\Gamma_0$, samples with several tubes in parallel can have even lower resistances, down to $2.5k\Omega$.

Fig. 7.3 shows the transport response to a voltage applied to an underlying gate (100nm thick oxide layer) for a device with a 2nm thick tubule. One observes a higher conductance for negative gate voltages V_g . As already mentioned in section 2.4.1, most SWCNT based devices fabricated similar to ours show a p-type behavior. Thus, in the negative gate voltage regime, both semiconducting and metallic nanotubes contribute to the conductance. In the positive regime, the gap of the semiconducting tubes lies in

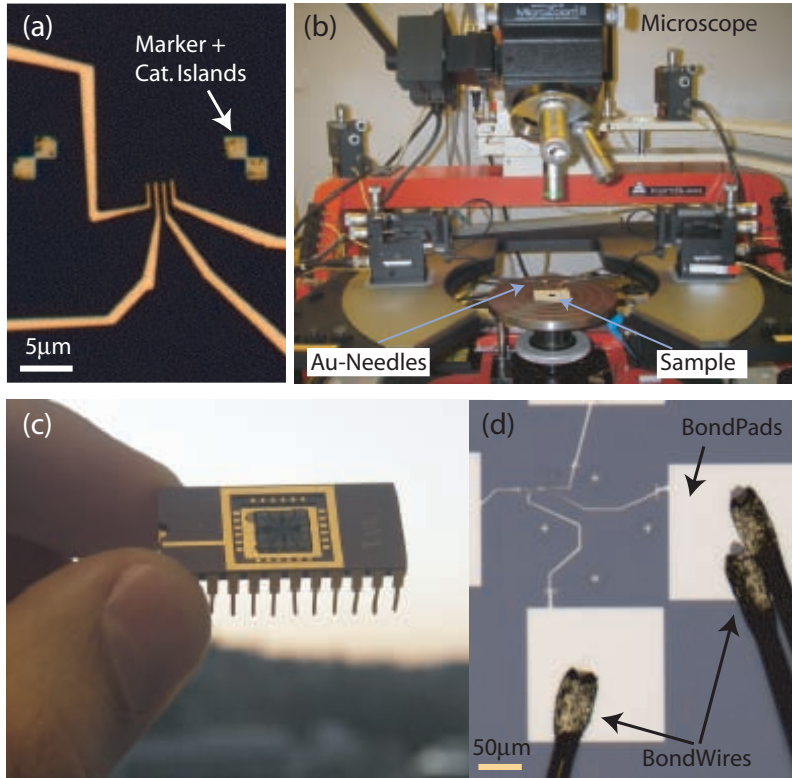


Figure 7.1: *Sample mounting for transport measurements. (a) Four-terminal electrode configuration on top of a nanotube. Quadratic thin film catalyst islands on chromium markers are also shown. (b) Sample probe station with optical microscope. (c) 24-pin chip carrier with mounted sample. Background shows the beautiful view of my office. (d) SWCNT device with gold wires bonded to the carrier.*

the bias window eV_{ds} and the transport through the semiconducting nanotubes remains blocked. The asymmetric non-linearity is contributed to at least one semiconducting tube. For a sufficient high bias, the gap or barrier is overcome and these tubes contribute also to the transport, cf. Fig. 2.6(d). The high 'off'-state conductance of $\Gamma(V_g = 10V) \approx 0.45e^2/h$ can be assigned to the contribution of at least one metallic tube in the bundle.

Another very interesting feature is the appearance of a large hysteresis in Fig. 7.3(a) when sweeping the gate voltage up and down. In the forward sweep direction, lower threshold voltages are obtained when compared to the reverse direction, as marked by the arrows. This effect occurs at ambient measurement conditions and can be exploited for nanoscale chemical sensors[213] or molecular memory elements[214]. The large hysteresis gap of $\approx 9V$ in Fig. 7.3(a) is mainly contributed to bulk oxide charge traps[214] or traps caused by the presence of some monolayers of water molecules[215]. The traps are charging and discharging slowly in time, an effect observable when changing the V_g sweep rate. In our experiments we used a slow sweep velocity of $0.1V/s$, leading to a larger hysteresis gap[215]. However, this effect is not desired for nanotube-based field-effect transistors. To get rid of the memory, devices are usually isolated from the environment by, e.g. PMMA covering. At low temperatures, the trap hoppings 'freeze' out and the hysteresis

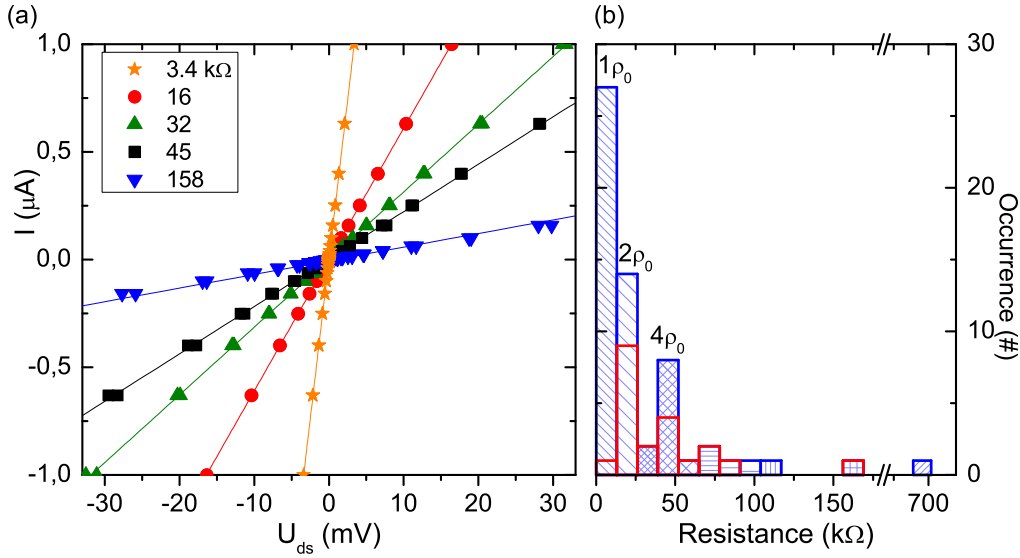


Figure 7.2: Transport results at room temperature. (a) Two-terminal measurements of some SWCNT devices. Data is depicted by symbols, linear fits by the solid curves. The resistance is given by the responding inverse of the slope $R^{-1} = dI/dV$ and is listed in the inset. (b) Histogram of the two-terminal resistances of SWCNT devices using Pd or Au as contact material. Mostly 1 to 4 tube devices were measured. Red marked bars correspond to single tube devices.

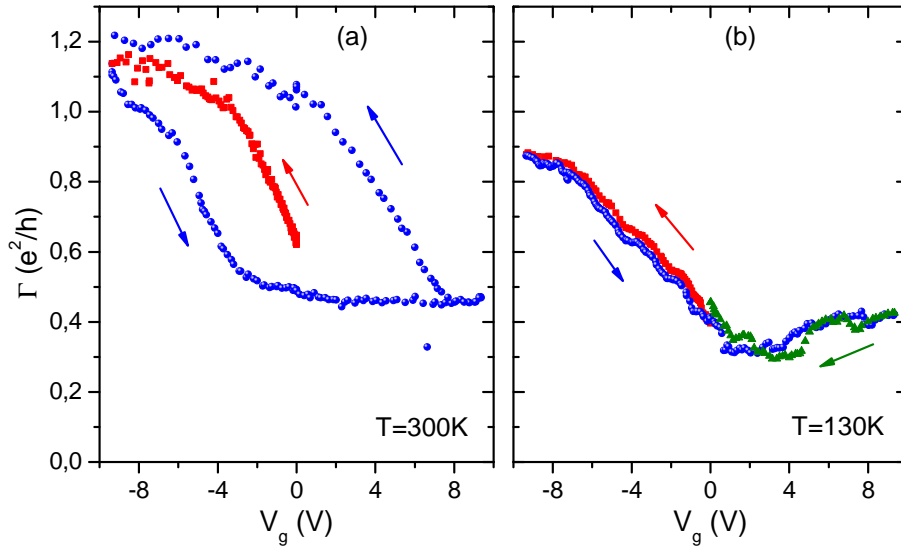


Figure 7.3: Memory effect of SWCNT devices by sweeping the gate voltage V_g in ambient environment. The sweep directions are marked in the images by arrows. (a) Measurements at room temperature exhibit a large hysteresis gap. (b) Memory effect vanishes at $T = 130\text{K}$.

vanishes. In measurements at $T = 130\text{K}$, the hysteresis is largely suppressed, as clearly demonstrated in Fig. 7.3(b) exhibiting no visible hysteresis gap.

7.1.1 Removing redundant CNTs in ready devices

Due to the very long and curly nature of our as-grown CVD SWCNTs, it happens frequently that some redundant CNTs short-cuts the electronic device as shown exemplarily in Fig. 7.6(c). We prepared samples in two manners: patterning of the electrodes near the pre-defined catalyst islands with the hope that only a few CNTs bridge the contacts or on top of individual tubes with precise positioning via AFM or low-magnification SEM. The blindly contacted samples consist of typically 1 to 4 tubes in parallel with diameters between 0.7 and 2nm, as determined by AFM measurements and we obtained rarely semiconducting transport features.

There are several easy methods to remove extra nanotubes. To obtain field effect transistor properties, the metallic tubes in the device can be burn by applying short and sufficiently high current pulses. The semiconducting tubes are afore depleted through the gate voltage action[9]. The current as a function of the bias of another device with three

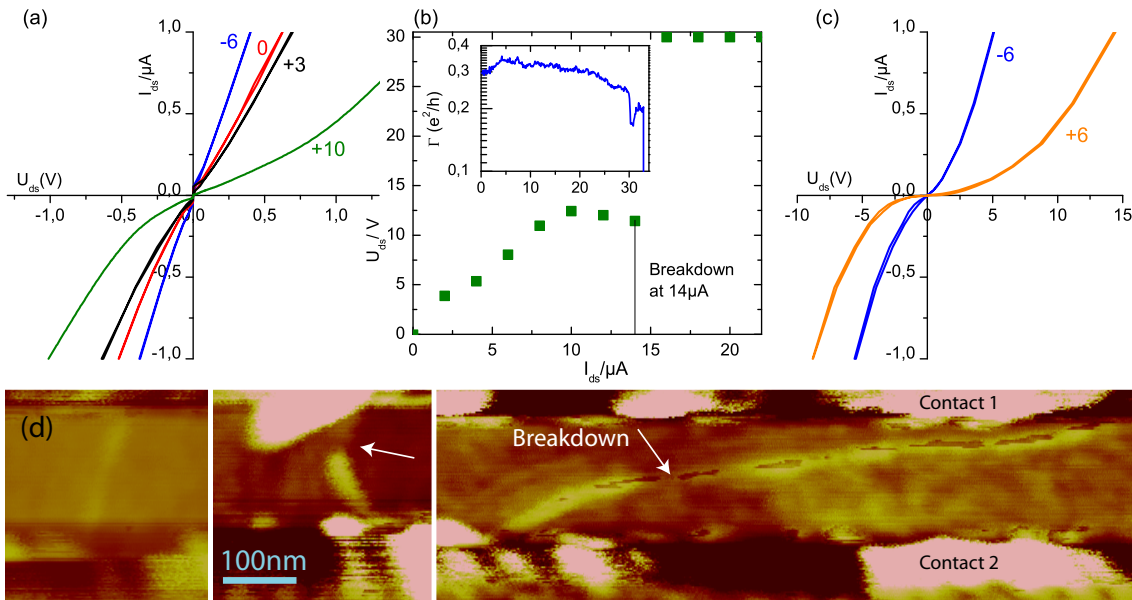


Figure 7.4: Electrical burn-down of nanotubes. (a) V/I characteristics for different gate voltages given in the image. (b) Fast burn-down by applying a constant current. The maximal supportable current is around $14 \mu\text{A}$ is marked by a sudden reaching of the maximum voltage set in priori. Inset: Slow break-down curve of another device shows negligible dependence of the conductance. $I_c \sim 32 \mu\text{A}$. (c) Pronounced semiconducting behavior after the burning process. (d) AFM images reveal that two of the three contacting tubes have now small gaps along the tube axis, as marked by arrows.

nanotubes contacted in parallel and a channel length of $L = 150 \text{nm}$ is shown in Fig. 7.4(a). Different gate voltages (given in the image) lead to different transport responses. For a negative gate voltage (blue), the current is linear with a resistance of $400 \text{k}\Omega$. Increasing V_g also increases the resistance and near $V_g = 0$ (red) we obtain $R = 700 \text{k}\Omega$ with small deviations from of the linear slope. For very positive gate voltages (green), the device exhibits a well pronounced non-linearity. The non-linearity can be attributed to the presence of semi-conducting SWCNTs as well as to a large asymmetric Schottky barrier. To burn

selectively the semiconducting SWCNTs, the current is raised in constant steps with an applied high positive gate voltage $V_g = +20V$, see Fig. 7.4(b). Breakdown occurs after a saturation phase at a critical current of $I_c \sim 14\mu A$. The bias current curves in Fig. 7.4(c) show now a pronounced non-linear behavior. For positive gate voltages (orange), a large non-conducting region, whereas for negative V_g (blue) a much higher conductance is detected. The inset of Fig. 7.4(b) shows the dependence of the conductance on the bias of another sample using $V_g = +20V$. Some conductance oscillations can be observed shortly before breakdown at $I_c \sim 32\mu A$. The graph shows a decreasing conductance with increasing bias voltage. This can be related to an increase of electron-phonon scattering and a corresponding self-heating[216]. Summing up, our tubes could withstand very high currents. By assuming a cylinder of radius $0.7nm$, the maximum current density $j = I_c/A$ of the SWCNTs can be estimated: $j \approx 1 \times 10^{-8} A/cm^2$ and $j > 2 \times 10^{-8} A/cm^2$ for the first and second device, respectively. This value is in the range of the reported data in the literature[34] and indicates a good structural quality of our as-grown tubes. A careful examination of the second device after burn-down revealed, that the nanotube could withstand the high current. Instead of that, the contacting material (a Pd/Au bilayer) melted at the smallest parts of the electrodes along several μm . We are currently analyzing the poor quality of this metallic bilayer. The topographic AFM images in Fig. 7.4(d) display the first SWCNT device after breakdown. The location of the breaks can be easily identified as the points where the tube heights vanish and are marked by arrows. For most of the (willingly or not) burnt nanotubes, the breakdown occurred approximately in the middle of the tube channel, indicating that it is the result of nanotube bulk heating and that the contacts act as heat reservoirs reducing the probability of breakdown in their vicinity.

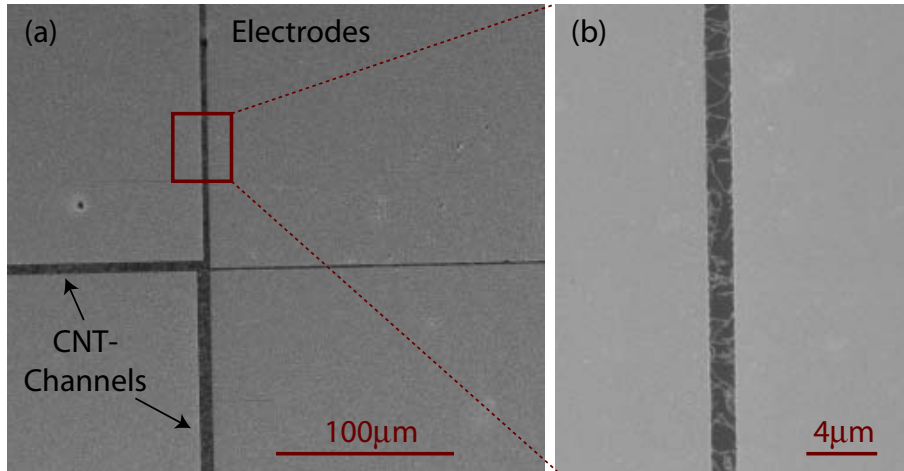


Figure 7.5: SEM images of an electronic device sustaining large currents. (a) Overview over the large bond pads. (b) Close-up of the nanotubes bridging the gap between the pads. Co-Apoferritin-assisted SWCNT synthesis was employed.

We also fabricated devices which can withstand very high currents. We contacted many nanotubes in parallel by large electrode bonding pads of $300 \times 300\mu m^2$ with a small gap of 1,2,4 and $8\mu m$ in between them, as shown in Fig. 7.5(a). The tubes bridging the

contacts can be observed in the SEM image in Fig. 7.5(b). The SWCNTs are grown by employing a substrate covered homogeneously with Co-Apoferritin. This electrode layout can withstand currents up to mA .

To obtain individual tube devices, the most intuitive way is by 'scratching' the tube off the substrate with a hard cantilever using an AFM in contact mode. This method is rather slow and cantilever-consuming but even tubes laying close together can be removed without any further damage to the device channel tube. Another way of removing is by cutting the

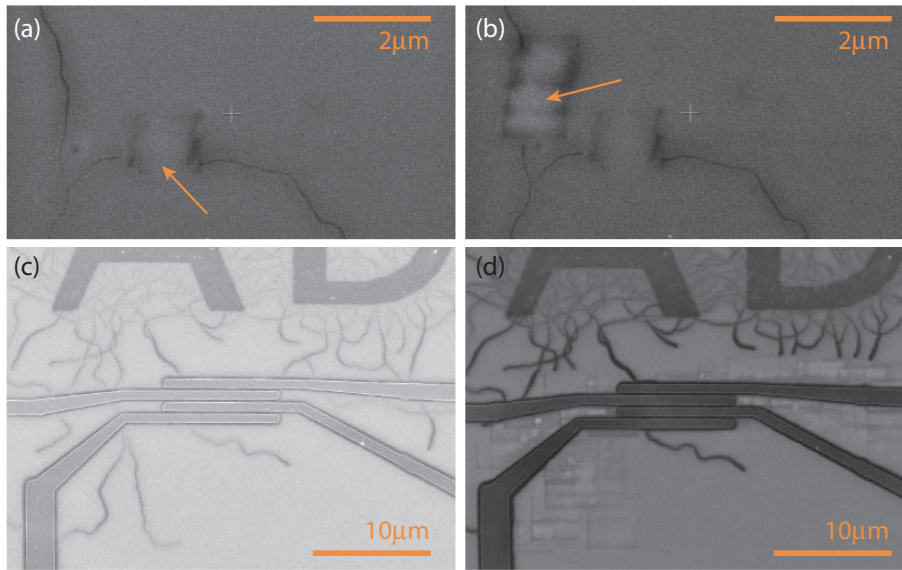


Figure 7.6: H_2O etching in environmental low-pressure SEM. The first tube (a) and second tube (b) is cut at the arrows. A ready electronic device (c) is cleaned from contacting but unwanted CNTs (d). A water pressure of 20 mbar and an etching dosis of approximately $10.000\mu C/cm^2$ was used.

tubes with an focused gallium ion beam. However the role of the Ga ions implanted in the substrate is not clear. A more controlled method is by oxygen etching in an environmental SEM. We can operate our SEM at low vacuum in the presence of water vapor and at high dosis, the e-beam brakes the water molecules. The resulting oxygen radicals etch effectively the carbon present in the irradiation region. A sequence of successful cutting of nanotubes, marked by arrows, is shown in Fig. 7.6(a,b). A water pressure of 20mbar, an etching dosis of approximately $10.000\mu\text{Coulomb}/cm^2$ and an acceleration voltage $V_a = 5kV$ were used. The ready device in Fig. 7.6(c) can be cleaned from the two redundant nanotubes outside the channel region, as demonstrated in the resulting single tube device in Fig. 7.6(d). The 2-terminal resistance augmented from $2.5k\Omega$ to $250k\Omega$ and showed a slight non-linear behavior. We attribute this increase with side-effects of the removing operation when the irradiating region is close to the remaining tube rather than with semiconducting behavior of the remaining SWCNT. Currently we are improving the parameters and the preliminary results are promising.

7.2 Low temperature measurements

As already shortly introduced in chapter 2, many interesting physical phenomena are expected at low temperatures, when the system's dimensions are of the order of characteristic length scales. Quantum effects such as Coulomb blockade oscillations, Kondo and Fabry-Perot interference phenomena become observable at low temperatures. In fact, size quantization should play an important role for a nanotube confined between two metal electrodes. The finite-size nanotube actually acts as a zero-dimensional quantum dot with a discrete energy level spectrum. The Coulomb repulsion energy $E_c = e^2/2C$ of the electrons in the QD can be very high due to the low capacitance of the dot leading to a vanishing current, also known as the Coulomb blockade regime.

Suitable devices are fixed and bonded at a sample holder in to order carry out low temperature measurements. We experienced serious bonding (grounding) problems, so that only a couple devices out of all Ohmical contacted SWCNTs could withstand the ultrasonic bonding treatment. Thus, our low-temperature measurements are only preliminary results with the main observed effects reproducible among them.

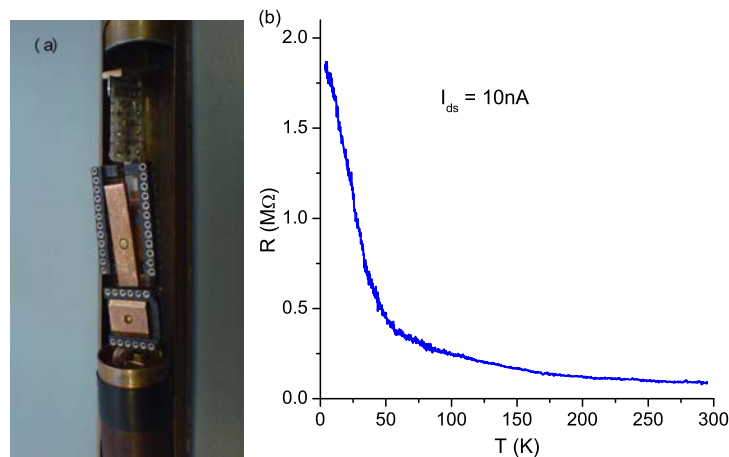
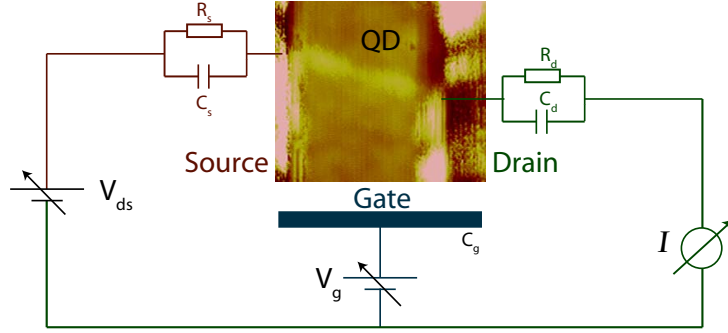


Figure 7.7: (a) Equipment for low-temperature measurements. (b) Resistance as function of temperature of a SWCNT device for a constant current $I = 10\text{nA}$.

The bonded chip carrier is mounted in the low temperature sample holder, shown in Fig. 7.7(a), and introduced into a helium dewar. Cooling to liquid helium temperatures (4.2K) usually decreases the conductance. The temperature dependence of the resistance of a sample with a room-temperature resistance of $R_{RT} = 82\text{k}\Omega$ is depicted in Fig. 7.7(b). A constant current of 10nA was used. The resistance increases slowly with the decreasing temperature until a sudden augment in the resistance up to the order of $\text{M}\Omega$ can be observed, marking the entrance of the Coulomb blockade (CB) regime. Another device with more transparent contacts increased its resistance from $13\text{k}\Omega$ at room temperature to $200\text{k}\Omega$ at 4.2K (not shown).

Figure 7.8: Electric circuit diagram of a SWCNT ($d \sim 1\text{nm}$) quantum dot of length $L \sim 150\text{nm}$. The QD is sandwiched between source and drain electrodes and the contacts can be characterized by a RC junction. The gate voltage V_g couples only capacitively to the QD via the capacitance C_g .



7.2.1 Theory of single electron tunneling

The electric circuit diagram for a SWCNT quantum dot is illustrated in Fig. 7.8, where each contacts can be characterized by a RC junction. The underlying gate is assumed not to contribute to the transport, i.e. $R_c = \infty$. The gate couples capacitively via C_g to the dot and can be used to tune the electrostatic potential of the dot with respect to the leads. The number of electrons on this QD has to be an integer N and the charge is quantized and equal Ne , with e being the electron charge. If we allow now tunneling processes from the electrodes into the dot, the number of electrons N adjusts itself to minimize the energy. When adding an extra electron to the dot, the charge discontinuously increases by e and the electrostatic potential is changed by the charging energy $U_c = \frac{e^2}{C}$, where C is the capacitance of the dot[25, 45, 217, 218]. This charging energy becomes important when it exceeds the thermal energy $k_B T$. The second requirement is that the quantum fluctuations of the electron number on the dot are suppressed. This is fulfilled when the tunneling rate is very low. A typical time scale to charge or discharge the dot is $\Delta t \sim RC$. The Heisenberg uncertainty relation yields $\Delta U \Delta t = \frac{e^2}{2C} RC \gtrsim h$ which implies that R should be larger than the resistance quantum ρ_0 to omit quantum fluctuations over the time scale of the measurements. The capacitance of a finite nanotube with length L and diameter d can be approximated by a cylinder embedded in a dielectric of thickness t [215]

$$C_{CNT} = 2\pi\epsilon_0\epsilon_r \frac{1}{\cosh^{-1}(2t/d)} \approx 2\pi\epsilon_0\epsilon_r \frac{L}{\ln(t/d)} . \quad (7.1)$$

For the SWCNTs in typical devices, $d \approx 2\text{nm}$, $L \approx 150\text{nm}$ and $\epsilon_r = 4$ the dielectric constant of the $t = 1\mu\text{m}$ thick silicon dioxide, one obtains $C_{CNT} \approx 5.4\text{aF}$ and $U_c \approx 30\text{meV}$. Charging effects should thus be observable for temperatures below 60K for a $1\mu\text{m}$ long device.

As the dimension of the system is decreased, the spacing ΔE between the discrete energy levels are increased and may become observable at low temperatures. The level spacing is easily calculated when remembering the linearity of the energy dispersion relation near the Fermi level around the K points (cf. Fig. 3.6). Assuming that the orbital level degeneracies are lifted, the eigenenergies of the discrete spectrum of a SWCNT with length L are separated by[33]

$$\Delta E = \frac{h v_F}{4L} . \quad (7.2)$$

The degeneracy may be lifted by disorder or by the contacts which may couple differently

to the two orbital states. For typical device lengths of $L = 150\text{nm}$, this amounts to $\Delta E = 5\text{meV}$.

A simple model to understand electronic transport through a QD is the constant interaction (CI) model. Two assumptions are done: First, the coupling of the system to the outer world can be described by a single capacitance $C = C_s + C_d + C_g$ and all the Coulomb interactions of the electrons on the dot are captured by C . The resistance of relevance for the suppression of the quantum fluctuations is now that of the tunnel barriers. Second, the discrete energy spectrum of the dot as well as the capacitance are independent of the number of electrons in the dot and the applied bias[219–221].

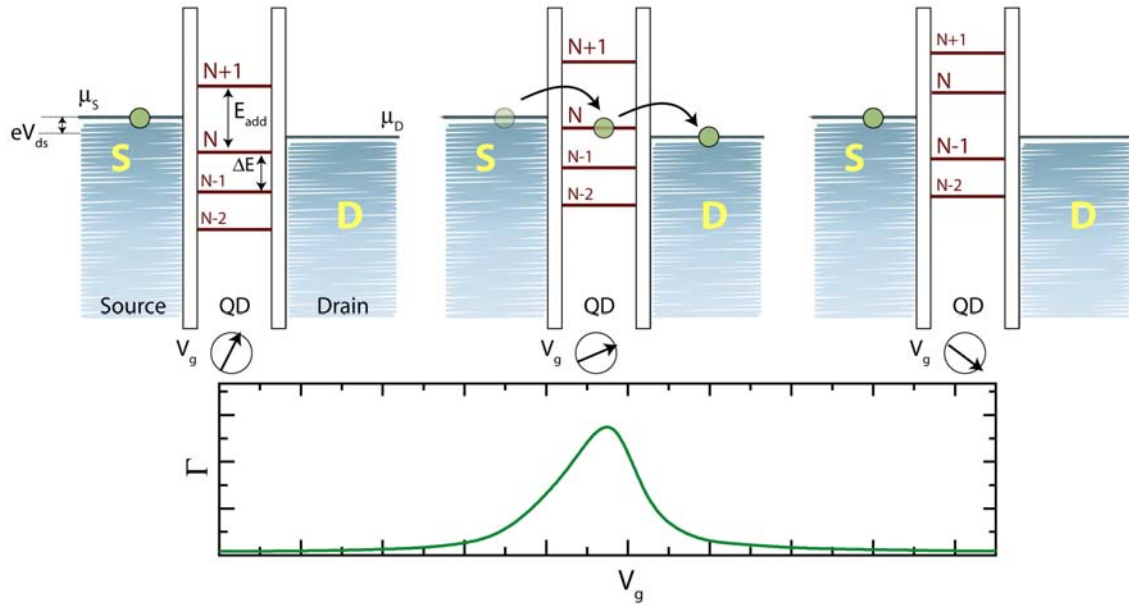


Figure 7.9: Schematic diagram of the Coulomb blockade regime. The quantum dot is isolated from the source and drain electrodes by two tunnel barriers. (a) The QD has N electrons and for low source-drain bias, the transport through the QD is blocked due to the charging energy. (b) The electrochemical potential of the QD may be changed by the action of a gate voltage V_g . Eventually, the N th level lies within the bias window $\mu_s - \mu_d = eV_{ds}$ and an onset of a sequential single electron current is detected. The number of electrons in the dot can alternate between N and $N-1$. (c) Further augment of V_g shifts the discrete dot level out of the bias window and transport is prohibited again. The number of electrons on the dot remains constant at $N-1$. (d) High bias voltages also allow transport events. A two electron tunneling situation is depicted. (e) Typical experimental result of the SET effect demonstrating one of the well-defined conductance peaks as function of V_g in the linear transport regime ($I=2nA$) at 4.2K .

Applying a voltage V_g to the gate, the electrostatic energy of the dot can be changed continuously and induces an effective continuous charge $C_g V_g$. By sweeping this voltage the induced charge will be compensated in periodic intervals by tunneling of discrete charges onto the dot, as already shortly introduced in section 2.3.1. A detailed scheme of this effect is given in Fig. 7.9(a-c) in the linear transport regime, i.e. $V_{ds} \ll \Delta E/e, e/2C$. In Fig. 7.9(a), the dot is charged with N electrons. To add one electron one has to pay the Coulomb repulsion U_c which would raise the energy above the energy of the reservoirs. A

tunneling process is thus prohibited. Fig. 7.9(d) is an experimental measurement of the conductance as function of the gate voltage taken at 4.2K and demonstrate a vanishing conductance in case (a). By changing V_g , eventually the next levels gets aligned with the electrochemical potentials of the reservoir $\mu_s \sim \mu_d$. In this condition, shown in Fig. 7.9(b), the numbers of electrons in the dot can alternate between N and $N - 1$. This charge degeneracy leads to a finite current flow and a peak in the conductance. When the dot is charged with N electrons, this electron has to tunnel first to the drain before a new electron can tunnel onto the dot. This regime is also called sequential tunneling. Upon further increase of the gate voltage, the levels get misaligned again and the dot is left with a constant number of $N - 1$ electrons, see Fig. 7.9(c). Again, transport is energetically forbidden. This process, where the current is carried by successive discrete charging and discharging of the dot is known as single electron tunneling (SET).

The total energy of a dot with N electrons and an applied voltage V_{ds} to the source (with the drain grounded, see Fig. 7.8), is given in the CI model by[219]

$$U(N) = \frac{\left[-|e|(N - N_o) + C_s V_{ds} + C_g V_g \right]^2}{2C} + \sum_{n=1}^N E_n \quad , \quad (7.3)$$

where $-|e|$ is the electron (or hole) charge and N_o the number of electrons in the dot at zero gate voltage. The last term of eq. 7.3 is a sum over the occupied single-particle energies E_n with the level spacing $\Delta E = E_n - E_{n-1}$. In the linear transport regime ($V_{ds} \approx 0$), the electrochemical potential $\mu_{QD}(N)$ of a dot with N electrons is then

$$\mu_{QD}(N) = U(N) - U(N - 1) = \left(N - N_o - \frac{1}{2} \right) \frac{e^2}{C} - eV_g \frac{C_g}{C} + E_N \quad . \quad (7.4)$$

The energy E_{add} required to store an additional electron on the dot follows directly as the difference of these potentials:

$$E_{add} = \mu_{QD}(N + 1) - \mu_{QD}(N) = \Delta E + \frac{e^2}{C} \quad . \quad (7.5)$$

It is worth mentioning, that the energy of the charging energy U_c always have to be paid, but the level spacing energy only if the electron is stored in a new level[51, 222]. We assume non-degenerated levels in our devices so that both energies are required to store an additional electron on the dot, as indicated in Fig. 7.9(a). In the high bias regime, tunneling is possible, when one or more levels are in the bias window eV_{ds} . Fig. 7.9(c) depicts exemplarily the case of current carried by two electrons.

When the action of the gate voltage aligns the next energy level with the reservoir level, the electrochemical potential of the dot is changed from the N th to the $(N + 1)$ th on-state and thus $\mu_{QD}(N, V_g) = \mu_{QD}(N + 1, V_g + \Delta V_g)$. Using eq. 7.4 and eq. 7.5, we obtain for the distance in the gate voltage ΔV_g between the Coulomb oscillations:

$$\Delta V_g = \frac{C}{C_g} \frac{E_{add}}{e} \quad . \quad (7.6)$$

The pre-factor $\alpha := C_g/C \leq 1$ is a measure of the coupling strength between the QD and

the gate. It converts a change in the gate voltage into a change in the electrochemical potential of the QD. For large islands, i.e. vanishing energy splitting $\Delta E \sim 0$, the classical capacitance-voltage relation for a single electron charge is obtained, $\Delta V_g = e/C_g$.

7.2.2 Measurements of the Coulomb blockade regime at 4.2K

The above developed theory allows us to interpret our low-temperature data. Transport measurements of a short channel SWCNT quantum dot at liquid helium temperature of 4.2K using a current source is shown in Fig. 7.10. The device consists of two SWCNTs with diameters of $d = 1.5nm$ which are contacted in parallel and is fabricated on top of a thick oxide layer ($1\mu m$ SiO₂). Well separated CB peaks are obtained in the conductance

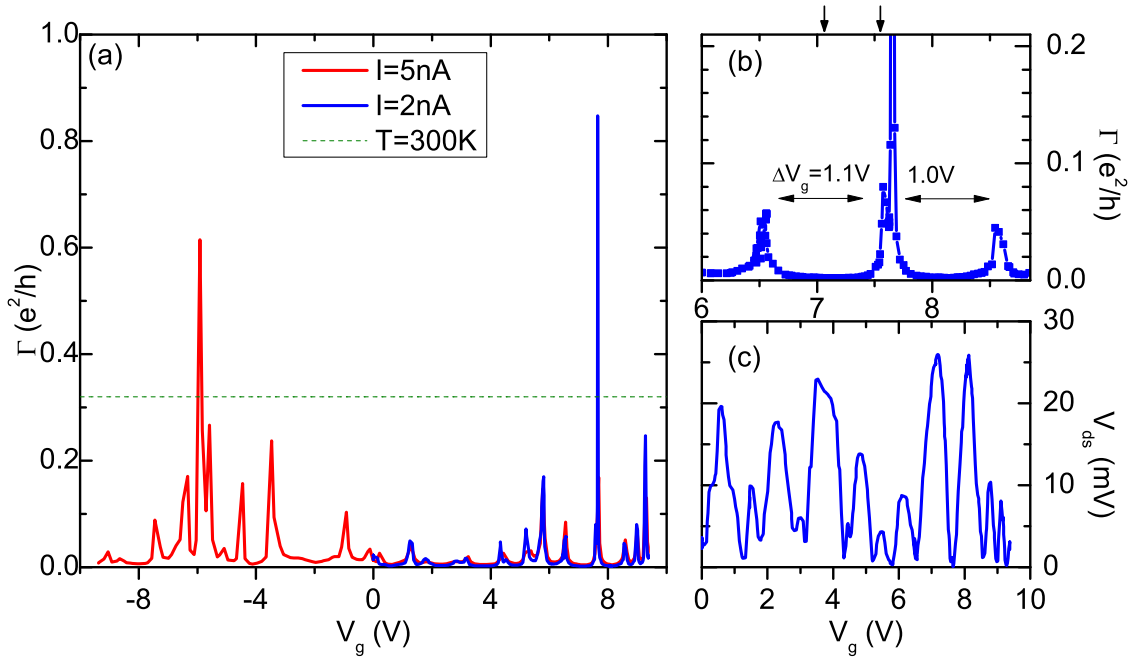


Figure 7.10: Coulomb blockade oscillation measurements at 4.2K of a short channel SWCNT quantum dot. (a) Conductance vs. gate voltage V_g exhibits well pronounced CB peaks. A constant current source was used. (b) Augmented region around $V_g = 7.6V$. (c) Bias voltage V_{ds} data showing the CB oscillations.

in Fig. 7.10(a) as a function of the gate voltage. The featureless room temperature data is shown as a dashed green line. The linear transport regime is assured by applying a current of $2nA$ (blue) and $5nA$ (red). Nevertheless, our present measurement setup does not allow the application of constant low bias voltages, so that instead of measuring along a horizontal cut of the two-dimensional conductance map, we probe the sample along the edges of the Coulomb diamond in Fig. 2.3(c). For values of V_g corresponding to peaks, conductances up to the order of e^2/h could be detected, whereas in the blockade region the resistance is several magnitudes higher. The two curves obtained by using different currents basically show the same behavior. Several sweeps of the same device in the same conditions always yielded the same CB-like oscillatory features. The obtained bias voltage

response is shown in Fig. 7.10(c). An augmented region around three typical CB peaks is exhibited in Fig. 7.10(b). From this, the large gate voltage spacing $\Delta V_g \approx 1V$ can be deduced.

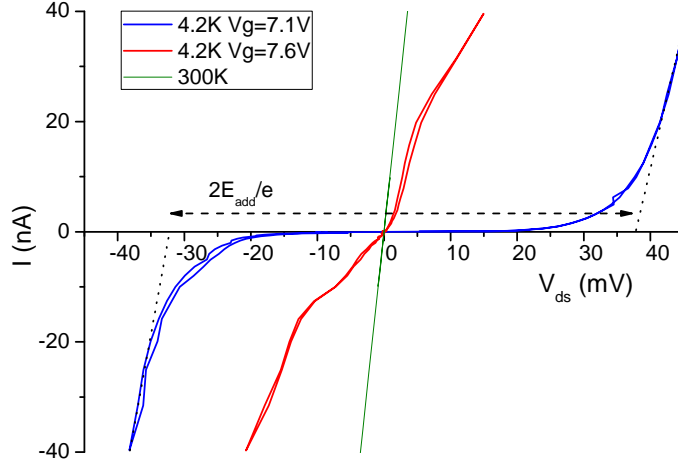


Figure 7.11: Coulomb blockade switching property at 4.2K. Blue curve was taken at V_g deep in the blockade region, whereas the red curve near the optimal on-state exhibit SET. Both voltages are marked with arrows in Fig. 7.10(b). The room temperature data is given in green. In all cases, one back and forward sweep is shown.

We investigate now the I-V characteristics at the on- and off-state of the device. Fig. 7.11 shows the current vs. bias voltage at two fixed gate voltages, as indicated by the arrows on top of Fig. 7.10(b). $V_g = 7.6V$ (red) corresponds to a conductance peak whereas $V_g = 7.1V$ (blue) lies approximately in the middle between two CB peaks. For comparison, the room temperature data is also shown as the green, linear curve. The first red curve represent the on-state of the device and SET is taking place. The curve is approximately linear with a slope of $0.1\Gamma_0$. This means that the data correspond to a situation with V_g near but not at a gate voltage with optimal aligned levels. As shown in Fig. 7.10(a), the maximum possible conductance at this peaks is around half Γ_0 . This could explain the steps observed in the conductance corresponding to excited states as introduced above. Another possibility is that CB traces of the second tube contacted in parallel are detected. The situation deep inside the Coulomb blockade is depicted by the blue curve in Fig. 7.11 exhibiting a strong non-linear slope with a large transport suppression region. The width of the transport suppression is an estimate of the energy to add an additional electron on the dot, $2E_{add}$, as indicated in Fig. 7.11. We obtain $2E_{add} = 70meV$ with a small asymmetric shift of $+5meV$ which is contributed to the capacitive coupling of the source C_s , drain C_d and gate C_g electrodes to the SWCNT[51]. The required charging energy is then, cf. eq. 7.5, $U_c = E_{add} - \Delta E \approx 30meV$. The total capacitance can be estimated through the charging energy and is approximately $C \approx 5.3aF$. This value is nearly identical to the capacitance obtained through geometrical estimations, cf. eq. 7.1. Using eq. 7.6, the gate coupling factor α can then be estimated as $\alpha = C_g/C = E_{add}/e\Delta V_g \approx 0.04$. This indicates a rather weak gate-to-dot coupling which we contribute mainly to the thick oxide employed. The gate capacitance is very low and approximately $C_g = \alpha C \approx 0.2aF$.

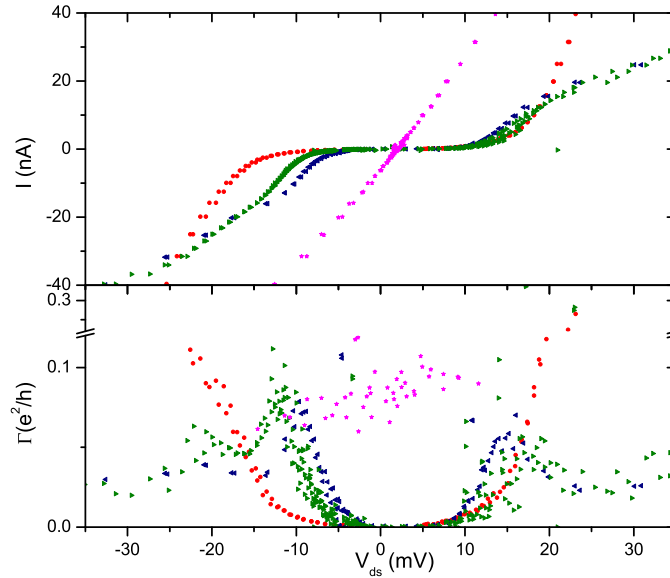


Figure 7.12: *I-V and conductance characteristics for different gate voltages in the Coulomb blockade regime at 4.2K. Two sweeps are shown.*

At intermediate gate voltage values, we obtain rich I-V characteristics. Fig. 7.12 shows the transport measurements for a device with a floating gate value under the same bias conditions. This means, that the effective gate voltage at open circuit changes due to charging slowly in time. The features can be understood when comparing the data with horizontal cuts of the conductance map in Fig. 2.3(c). The capacitance in Fig. 7.12(b) is calculated by the numerical derivative of Fig. 7.12(a). We observe again the linear conducting case of SET effects (blue) as well as transport suppression demonstrated by the large conductance gap (red). For intermediate states (green), we obtain staircase-like responses of the conductance which we identify as the contribution of excited states. Summarizing, we could fabricate SWCNT devices where we set up, carried out and improved all the required processing steps. Our samples show nearly transparent contacts as well as interesting low temperature quantum phenomena.

7.3 Non-carbon nanostructures

The active synthesis group at the institute frequently furnishes us with new one-dimensional nanostructures of varied composition. Just to state a few, we are able to produce MWCNTs, vanadium oxide nanotubes or -scrolls and manganese dioxide nanotubes. All tubes can be filled or intercalated with varied materials such as iron, potassium or lithium. The samples usually consist of larger diameter tubules which facilitates the separation due to a smaller van-der-Waals like attraction energy. The as-synthesized tubes are dispersed in ethanol or dichloroethane ($C_2H_4Cl_2$, from *VWR*), drop-coated onto a substrate with pre-defined marker structures and dry-blown with clean nitrogen. The lengths of several μm and diameters between 10 to 100nm allow an easy, fast and quite precise imaging in an optical microscope, as depicted exemplarily for a 13nm thick MnO_2 nanowire

in Fig. 4.1.

7.3.1 Transport properties of non-carbon nanostructures

Much effort has been done in the field of oxide nanostructures. The interesting magnetic properties of the bulk materials are very promising to search for new magnetic effects in low-dimensional systems. Manganese dioxide can have many polymorphic forms with very distinct properties. It gained a lot of attention due to its application as electrodes in layered MnO_2 /lithium batteries[223]. One-dimensional single crystal structures can be synthesized following a low-temperature hydrothermal and soft chemistry method. The detailed description can be found elsewhere[224, 225]. A typical TEM image of an as-produced MnO_2 nanotube is depicted in Fig. 4.10(b). A detailed analysis of the TEM images reveals that mainly (body-centered cubic) α - MnO_2 nanotubes and nanorods were synthesized.

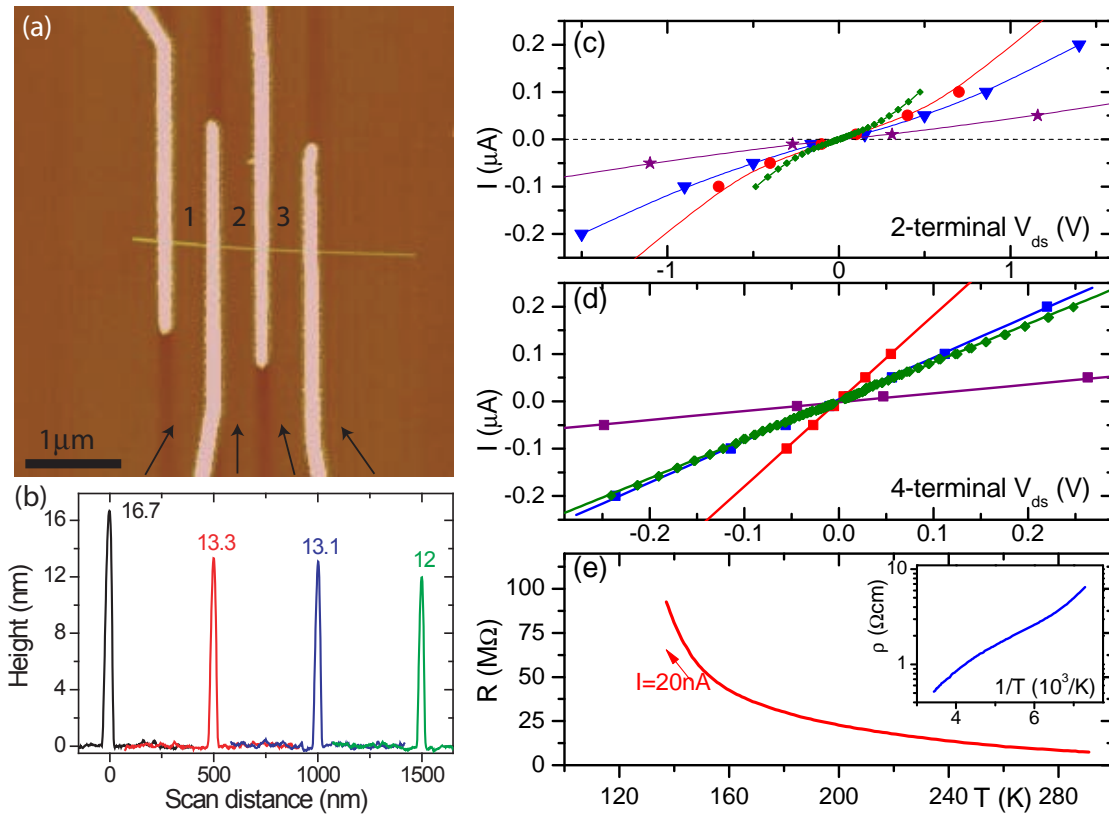


Figure 7.13: Transport properties of manganese dioxide nanotubes. (a) Topographic AFM image of a MnO_2 device with 4 top electrodes. (b) Height section across the tube of dot region 1-3 and in the right region. (c) Two-terminal non-linear and (d) four-terminal linear I - V characteristics of some devices. The two center electrodes are taken as voltage probes. The lines are linear fits to the data. (e) Temperature dependence of the resistance for $I = 20\text{nA}$ of the MnO_2 device shown in green in (c). Inset: $\log \rho$ versus $1/T$.

An as-fabricated 4-terminal MnO_2 device is shown in the topographic AFM image in Fig. 7.13(a). The nanotube is divided by the four electrodes into three quantum dots of

length $L = 450nm$. The tube diameters in the three section and on the right side are determined by AFM. The height profiles of the tube, as indicated in (a), are exhibited in Fig. 7.13(b). As clearly shown, the tube diameter changes along the tube axis up to one forth, an effect found in most investigated tubes. Diameters between 10 and 25nm are determined, consistent with TEM studies. Fig. 7.13(c) displays two-terminal transport measurements at room temperatures for various devices at the central dot 2. A pronounced non-linearity can be observed. On the other hand, the corresponding 4-terminal results of the same devices are very straight, further demonstrated by the linear fits to the data. The two outer electrodes are used to inject the current into the nanostructure and the two inner electrodes to probe the voltage drop along dot 2. As (approximately) no current flows through the voltmeter, the contact resistances are cancelled out in the measurement and from the inverse of the slope, we obtain the respective resistances. The resistance of the same dot drops about one order of magnitude in the four-point results R_{4p} when compared to the two-point measurements R_{2p} , which is actually the result of the sum over the resistances of both contacts R_c plus the three dots 1-3. By assuming equal values for the contacts as well as for the dots, we obtain $R_{2p} = 3R_{4p} + 2R_c$. This means that the contact resistance is of the same order than $R_{4p} \sim 1M\Omega$. This is verified in three-point measurements of devices with six and more electrodes. We assume, that the low contact transparency can be attributed to a large mismatch between the work functions of the nanorod and the electrodes (Pd, Cr or Au). Another possibility of the poor contacts could be a disturbed crystal structures at the contacting region. Indeed, the TEM images indicate that the outermost 'shells' of the wire do not exhibit the same regular crystal structure as the center region. This transport barrier is responsible for the non-linearity of the two-probe measurements.

The obtained resistances R_{4p} lie between 0.5 and $5M\Omega$. The apparent discrepancy of these values is lifted upon detailed examination of the tube diameter by AFM means. Exemplarily, we discuss the samples with the two R_{4p} -extrema. The device with the highest resistance, $R_{4p} = 5.3M\Omega$, corresponds to the red curve as well as the displayed AFM image in Fig. 7.13(a). From this we can estimate the resistivity, $\rho = R \cdot \frac{A}{L} = 0.16\Omega cm$, using the device length $L = 450nm$ and the diameter of dot 2, $d = 13nm$. The tube diameter of the device with the lowest resistance, $R_{4p} = 0.5M\Omega$, is determined being $d = 23nm$ and we obtain $\rho = 0.046\Omega cm$. The resistivity of the bulk mother compound, the layered MnO_2 , is reported in the range from $\rho = 0.1$ to $10^5\Omega cm$ [226–228]. Thus, our synthesized one-dimensional MnO_2 nanowires represent a lower resistivity limit, indicating a structural good quality.

We also probed the magneto-transport and applied magnetic fields up to six Tesla. No visible changes in the magneto-resistances are obtained at room temperature. Magnetization measurements have been performed on these MnO_2 nanowire samples using a superconducting quantum interference device (SQUID) magnetometer (*Quantum Design MPMS XL5*). The applied field was $B = 0.1$ Tesla and the data were obtained in the temperature range from 2 - 320K. The results show a magnetic phase transition at around 18K, presumably from paramagnetic to antiferromagnetic. At even lower temperatures (2K), a transition to the ferromagnetic phase is identified[229]. In order to observe its effect on the transport properties, we cooled down the sample corresponding to the green curves. Fig. 7.13(e) demonstrate a strong increase of the resistance R_{2p} upon decreasing temperature. We are not sure if this effect is to contribute solely to the contact barriers or

if the conductance channels of the MnO_2 nanowires also freeze out very fast. For layered bulk compounds, an exponential dependence of ρ is expected as function of $1/T$, because the layered MnO_2 compound is believed to be a compensated semiconductor with electrons and holes as carriers[227]. The inset of Fig. 7.13(e) shows roughly this behavior which we contribute to the presence of a near insulating contact barrier. When extrapolating this curve to low temperatures, we have to deal with contact resistance over $10G\Omega$ already around $T = 40K$, inhibiting a meaningful transport characterization of MnO_2 devices near the phase transition temperature. Currently, we are trying to improve the contact resistances by a post-fabrication heat treatment.

8 Conclusions & Outlook

In the course of the work of this thesis, several very important topics were addressed. Recently large nanotube-based macro-molecules were observed for the first time and pointed to a new ring-like structure. The experiments provide an advance in the fabrication of transport devices. The Theory to describe the ring like structures was fine-tuned.

8.1 Conclusions

In the theoretical part, we investigate two apparently quite different interferometric structures, namely a Y-junction ring and a quantum dot. Calculations with regards their mechanical as well as electronic properties were conducted. The annular YJR consists of a metallic single-wall carbon nanotube stem which bifurcates into two branches which are joined again. Six heptagons at each bifurcation region are required as topological defects to permit the change of the cylindrical shape resulting in a three terminal junction. We concentrate mainly on zigzag $(n, 0)$ SWCNTs due to the easy theoretical modelling as well as the possibility to tune the metallic nature depending solely on geometrical configurations. The influence of different asymmetries on the transport can then be determined: the lengths of the branches can be different, yielding an asymmetric ring, or equally, resulting in a symmetric ring. For very asymmetric systems, the longer branch appears buckled and a pronounced kink region is formed in the middle of the branch. Furthermore we can investigate different branch radii as well as semiconducting tunnelling loops. The quantum dot is modelled by two heterojunctions where a finite $(n, 0)_k$ SWCNT is sandwiched between two metallic $(2n, 0)$ stems. A ring of n heptagons, followed by n pentagons results in the drastic diameter change required to build the quantum dot.

For the first time, the formation of the newly proposed YJR could be unambiguously proven through observations in a high resolution transmission electron microscope. The asymmetric SWCNT loop with approximately 6\AA in diameter and 18nm in length is connected to two SWCNT stems of around 14\AA . Upon electron-beam irradiation in a high temperature environment (800°C), one clearly notices a merging process between the braces of the system, leading to a less asymmetric structure. After 90 seconds of irradiation we end up with a symmetric YJR. The reshaping process releases the potential energy contained in the compressed bigger branch, resulting in equal branch lengths. During the merging process, carbon atoms are knocked out of the tube walls by the intense electron-beam irradiation. The high-temperature environment allows the remaining carbon atoms to anneal and reconstruct the sp^2 lattice, leading to an overall reshaping of the systems geometry. The merging process can be stopped at any time and therefore,

ring-like SWCNT structures with defined symmetries can be realized upon electron beam irradiation at high temperatures in a controlled manner in relatively short periods of time.

We first determine the structural properties of these systems. To model the mechanical properties, Monte-Carlo simulations are performed with the Metropolis algorithm, using canonical or isothermal-isobaric ensembles. The system's energy is calculated with an empirical semi-classical potential proposed by Tersoff and the structural stability is compared with the pristine SWCNT counterparts. The influence of high temperatures on the atomic configurations are investigated upon raising adiabatically the temperatures letting the system relax completely before initiating the next temperature step. The structural changes are monitored by the change of neighbors of each atom and the resulting atomic configurations are visualized. The simulations indicate that smaller YJRs have lower formation energies, but are more sensitive to the higher temperature environment. A polymerization followed by a coalescence process of the branches of a symmetric YJR is observed at very high temperatures, resulting in a single tube with the stem's diameter. The kink region of asymmetric YJR welds at elevated temperatures forming an area with a lot of defects and upon rising the temperature, the branch ruptures starting at this region. On the other hand, bigger structures are more robust: only polymerization and kink welding is observed in symmetric and asymmetric rings, respectively.

We investigated the mechanical stability by loading an uni-axial tensile strain upon the structures and comparing the critical strain of YJRs with their pristine counterparts. The MC simulations indicate that the YJRs behave as brittle systems which rupture, always, at the bifurcation regions due to the topological heptagon defects. The rupture process starts when one or more heptagons begin to open resulting in a fast propagating of higher-order polygons around the tube axis. Very interestingly, even in the presence of these topological defects, the critical strain values of symmetric YJRs are of the same order of the pristine counterparts, indicating a very stable ring-like system. The complete fracture of asymmetric YJRs is a two stage process where first the short branch breaks at lower strain values than the pristine SWCNTs. Smaller diameter rings show comparable microscopical fracture details and mechanical stabilities.

The electronic properties of the systems are described by a tight-binding Hamiltonian adopting a single π band approximation. The other σ orbitals are easily included by extending the matrix to a 4×4 matrix, but they are omitted for the sake of computing time. The topological defects are directly incorporated by the Greens function renormalization formalism defined entirely in the real space. The electronic properties, such as density of states and conductance, are calculated using the Landauer-Bütiker description. We obtain very different transmission probabilities depending on the symmetry of the loop branches. Symmetric rings show the constant SWCNT two channel plateau near the Fermi level with some smooth Fabry-Perot-like oscillations superposed. For all metallic symmetric rings, they lead to a reduction of half the available channels. Sharp peaks are observed in the density of states and identified as being reminiscent effects of the eigenvalues of the torus of the YJR's central part. This picture changes completely when considering asymmetric YJRs. Transport suppressions are obtained correlated with DOS maxima and identified as the quantum interference effects of the phase shift the electronic wave acquires when travelling along the two branches with different lengths. These destructive quantum interference always lead to a complete transport suppression at determined energy values - depending of the system's structural configuration. Thus, asymmetric YJRs can be

tuned from metallic to semiconducting by Fermi level shifts and electron wave quantum interference effects. As expected, YJRs with a semiconducting central loop exhibit a clean transport gap corresponding to the larger semiconducting branch.

We extended the constant hopping integral approach by taking into account the atomic structure details leading to a more realistic description of macro-molecules with topological defects. For this purpose, the hopping integrals are scaled by the distance variation and bonding environment. This led to a more pronounced quantum interference oscillation and transport suppression. Furthermore, the gap of a semiconducting loop is filled by defect and extended states. A finite tunnelling probability mediated by these environment dependent states is observed. Both approaches result in very robust standing wave formations inside the central loop. A well defined sequence of standing waves appears each time one passes through the energy corresponding to a new one-dimensional van-Hove singularity. These modes do not contribute to the transport through the ring system and disperse quadratically. The origin of these modes are identified through a comparative study of the electronic properties of a finite quantum dot with similar constituent SWCNTs. As the standing wave dispersion in the QD is nearly exactly the same of the YJRs, we may conclude, that these higher-energy modes are reminiscent oscillations caused by the finite nature of the loop branches sandwiched between the stems. Instead of the low-energy DOS ring-peaks, harmonic Fabry-Perot conductance and DOS oscillations are observed in QDs. The sub-nanometer resolved oscillation maxima and low energy spacing make these interferometric structures promise candidates for a nanoscale tunable electronic switching device by different couplings to attached objects.

We succeeded with the first experimental transport devices fabricated entirely at the IFW Dresden. For this purpose we carried out a thorough study of the SWCNT synthesis via catalytic chemical vapor deposition as well as the characterization of the resulting SWCNT material by different microscopical and spectroscopical means. Thick, well aligned SWCNT forests of several hundred μm in length could be produced by using multilayer thin film catalysts and cyclohexane as the liquid carbon source. Homogeneously dispersed catalyst particles initiating the synthesis of very long individual SWCNT are obtained by Ferritin as well as cobalt inserted Apoferritin solutions using methane as carbon feedstock. Individual SWCNTs are growing off pre-patterned catalyst islands using wet chemistry catalysts as well as ultra-thin cobalt or iron films employing ethanol or *n*-heptane as carbon source. The presence of SWCNTs is determined by the appearance of a radial breathing mode in resonant Raman spectroscopy and directly visualized in a transmission electron microscope. The as-grown individual tubes without need for prior purification treatments are suitable for inclusion in transport devices. The position and diameter of the tubes laying on the clean silicon oxide substrate can be precisely determined by atomic force microscopy. The electrodes are patterned on the top of the tubes using a new electron beam lithography setup installed during the course of this thesis. The as-produced nanotube devices with gold or palladium contacts show a linear current-voltage behavior with resistances between some units and hundreds of $k\Omega$. They can withstand currents of several tenths μA corresponding to maximal current densities of at least $2 \times 10^{-8} \text{A}/\text{cm}^2$. In devices comprising semiconducting nanotubes, the memory effect in the conductance upon sweeping the gate voltage is observed. At low temperatures, the Coulomb blockade regime is observed for devices with opaque contacts. Pronounced Coulomb blockade peaks in the conductance corresponding to single electron tunneling are

obtained at $4.2K$. Individual tube devices are obtained by the controlled oxygen etching of redundant nanotubes in an environmental SEM. Furthermore, non-carbon nanotubes were also integrated into electronic devices. MnO_2 nanotubes show linear I/V characteristics in 4-terminal measurements with a resistivity around $0.1\Omega/cm$.

8.2 Outlook

What comes next?

In the future work, the aim will be the reduction of the contact resistances down to the order of a resistance quantum of individual tube devices. Different lithography parameters as well as different resist types will be tested to diminish any residue polymer layers between the nanotube and electrode metal. The influence of the CVD synthesis parameters will be analyzed with respect of the deposition of amorphous carbon on top of the tubes as well as structure quality suitable for transport measurements. Transparent contacts enables the observation of Fabry-Perot-like interferences and we want to examine the influence of the nanotube channel length on the oscillation effects.

Further important insights can be gained by the action of a dopant. A thorough study of the influence of lithium or potassium as n-type dopant on the electronic properties of the as-fabricated nanotubes will be carried out. The dopant intercalation will be done in an ultra-high vacuum environment with subsequent thermal equilibration and evaporation of redundant dopant atoms. We expect semiconducting/metallic transitions due to Fermi-level shifts. Insulating non-carbon nanotubes could thus be triggered to the metallic state which is not accessible to a finite gate-voltage action. The developed processing route allows the fabrication of free-standing nanotube devices on thin membranes for combined TEM and transport measurements. New findings of the role and positions of the dopant atoms could be gained by observation of conductance changes together with direct visualization in TEM micrographs upon step-wise doping. The suspended SWCNT synthesis may allow us to fabricate the already observed ring-like interferometric structure by contacting preferentially crossing nanotubes with subsequent merging in a transmission electron microscope using a high-temperature environment, similar to the reshaping process discussed in section 6.3.

The theoretical model can be easily extended to include the effects of a magnetic field $\vec{B} = B\hat{z}$. The equilibrium atomic positions of the relaxed YJR structure can be directly used in the calculation of the electronic properties of the ring-like system with a penetrating magnetic flux. The phase shift (cf. eq. 5.21) between two orbitals located at the cartesian coordinates \vec{R}_i and \vec{R}_j is obtained according to the general formula

$$\Delta G_{\vec{R}_i\vec{R}_j} = B \cdot \frac{2\pi}{\phi_0} \Delta y \frac{x_i + x_j}{2} \quad . \quad (8.1)$$

We expect very interesting Aharonov-Bohm like electron interference effects in the presence of an external magnetic field for otherwise un-observable SWCNT-based devices and hope to verify the theoretical predictions in experiments.

Bibliography

- [1] R. P. Feynman, "There's plenty of room at the bottom." American Physical Society at the California Institute of Technology (Caltech), 12 1959. [13](#)
- [2] M. Reibold, P. Paufler, A. A. Levin, W. Kochmann, N. Patzke, and D. C. Meyer, "Materials: Carbon nanotubes in an ancient damascus sabre," *Nature*, vol. 444, pp. 286–286, Nov. 2006. [14](#)
- [3] M. S. Dresselhaus and R. Smalley, eds., *DoD Workshop in Washington: Carbon-Carbon materials*, 1990. [14](#)
- [4] S. Iijima, "Helical microtubules of graphitic carbon," *Nature*, vol. 354, pp. 56–58, 1991. [14](#), [42](#)
- [5] L. Radushkevich and V. Lukyanovich, "O strukture ugleroda, obrazujucesja pri termiceskom razlozenii okisi ugleroda na zeleznom kontakte," *Zurn Fisic Chim*, vol. 26, pp. 88–95, 1952. [14](#)
- [6] S. Iijima and T. Ichihashi, "Single-shell carbon nanotubes of 1-nm diameter," *Nature*, vol. 363, pp. 603–05, 1993. [14](#), [42](#)
- [7] D. S. Bethune, C. H. Kiang, M. S. de Vries, G. Gorman, R. Savoy, J. Vazquez, and R. Beyers, "Cobalt-catalysed growth of carbon nanotubes with single-atomic-layer walls," *Nature*, vol. 363, pp. 605–07, 1993. [14](#), [42](#)
- [8] A. Vijayaraghavan, S. Blatt, D. Weissenberger, M. Oron-Carl, F. Hennrich, D. Gerthsen, H. Hahn, and R. Krupke, "Ultra-large-scale directed assembly of single-walled carbon nanotube devices," *Nano Lett.*, vol. 7, pp. 1556–1560, June 2007. [15](#), [40](#)
- [9] P. G. Collins, M. S. Arnold, and P. Avouris, "Engineering carbon nanotubes and nanotube circuits using electrical breakdown," *Science*, vol. 292, no. 5517, pp. 706–709, 2001. [15](#), [102](#)
- [10] R. Seidel, M. Liebau, G. S. Duesberg, F. Kreupl, E. Unger, A. P. Graham, W. Hoenlein, and W. Pompe, "In-situ contacted single-walled carbon nanotubes and contact improvement by electroless deposition," *Nano Lett.*, vol. 3, pp. 965–968, July 2003. [15](#), [39](#)
- [11] C. Papadopoulos, A. Rakitin, J. Li, A. S. Vedenev, and J. M. Xu, "Electronic transport in γ -junction carbon nanotubes," *Phys. Rev. Lett.*, vol. 85, pp. 3476–3479, Oct. 2000. [15](#), [73](#)
- [12] M. Terrones, F. Banhart, N. Grobert, J. C. Charlier, H. Terrones, and P. M. Ajayan, "Molecular junctions by joining single-walled carbon nanotubes," *Phys. Rev. Lett.*, vol. 89, p. 075505, Aug. 2002. [15](#), [73](#)
- [13] A. N. Andriotis, M. Menon, D. Srivastava, and L. Chernozatonskii, "Rectification properties of carbon nanotube γ junctions," *Phys. Rev. Lett.*, vol. 87, pp. 66802(1–4), 2001. [15](#), [74](#)
- [14] A. N. Andriotis, M. Menon, D. Srivastava, and L. Chernozatonskii, "Transport properties of single-wall carbon nanotube γ junctions," *Phys. Rev. B*, vol. 65, pp. 165416(1–13), 2002. [15](#), [73](#), [74](#)
- [15] H. Watanabe, C. Manabe, T. Shigematsu, and M. Shimizu, "Dual-probe scanning tunneling microscope: Measuring a carbon nanotube ring transistor," *Appl. Phys. Lett.*, vol. 78, no. 19, pp. 2928–2930, 2001. [15](#)
- [16] L. A. Chernozatonskii, "Carbon nanotube connectors and planar jungle gyms," *Phys. Lett. A*, vol. 172, pp. 173–76, 1992. [15](#)
- [17] A. Bachtold, C. Strunk, J.-P. Salvetat, J.-M. Bonard, L. Forro, T. Nussbaumer, and C. Schonenberger, "Aharonov-bohm oscillations in carbon nanotubes," *Nature*, vol. 397, pp. 673–675, Feb. 1999. [15](#), [66](#)
- [18] S. Roche, G. Dresselhaus, M. S. Dresselhaus, and R. Saito, "Aharonov-bohm spectral features and coherence lengths in carbon nanotubes," *Phys. Rev. B*, vol. 62, pp. 16092–16099, Dec 2000. [15](#), [69](#)
- [19] R. Martel, H. R. Shea, and P. Avouris, "Rings of single-walled carbon nanotubes," *Nature*, vol. 398, p. 299, 1999. [15](#), [73](#)
- [20] R. Martel, H. R. Shea, and P. Avouris, "Ring formation in single-wall carbon nanotubes," *J. Phys. Chem. B*, vol. 103, pp. 7551–7556, Sept. 1999. [15](#)
- [21] C. G. Rocha, M. Pacheco, Z. Barticevic, and A. Latgé, "Carbon nanotube tori under external fields," *Phys. Rev. B*, vol. 70, p. 233402, Dec. 2004. [15](#), [73](#), [93](#)
- [22] S. Latil, S. Roche, and A. Rubio, "Persistent currents in carbon nanotube based rings," *Phys. Rev. B*, vol. 67, p. 165420, Apr 2003. [15](#)
- [23] G. Kim, S. B. Lee, T. S. Kim, and J. Ihm, "Fano resonance and orbital filtering in multiply connected carbon

- nanotubes," *Phys. Rev. B*, vol. 71, p. 205415, May 2005. 15
- [24] J. Nygard, D. H. Cobden, and P. E. Lindelof, "Kondo physics in carbon nanotubes," *Nature*, vol. 408, pp. 342–346, Nov. 2000. 15, 25
- [25] P. Jarillo-Herrero, S. Sapmaz, C. Dekker, L. P. Kouwenhoven, and H. S. J. van der Zant, "Electron-hole symmetry in a semiconducting carbon nanotube quantum dot," *Nature*, vol. 429, pp. 389–392, May 2004. 15, 24, 106
- [26] W. Liang, M. Bockrath, D. Bozovic, J. H. Hafner, M. Tinkham, and H. Park, "Fabry - perot interference in a nanotube electron waveguide," *Nature*, vol. 411, pp. 665–669, June 2001. 15, 23, 25, 26
- [27] J. Jiang, J. M. Dong, and D. Y. Xing, "Quantum interference in carbon-nanotube electron resonators," *Phys. Rev. Lett.*, vol. 91, p. 056802, Aug. 2003. 15, 26
- [28] H. Kim, J. Lee, S. J. Kahng, Y. W. Son, S. B. Lee, C. K. Lee, J. Ihm, and Y. Kuk, "Direct observation of localized defect states in semiconductor nanotube junctions," *Phys. Rev. Lett.*, vol. 90, p. 216107, May 2003. 15, 73, 78
- [29] D. Orlikowski, H. Mehrez, J. Taylor, H. Guo, J. Wang, and C. Roland, "Resonant transmission through finite-sized carbon nanotubes," *Phys. Rev. B*, vol. 6315, p. 155412, Apr. 2001. 15
- [30] C. G. Rocha, A. Latgé, and L. Chico, "Metallic carbon nanotube quantum dots under magnetic fields," *Phys. Rev. B*, vol. 72, p. 085419, Aug. 2005. 15, 73, 78, 97
- [31] S. Datta, *Electronic Transport in Mesoscopic Systems*. Cambridge University Press, 1998. 19, 61, 62
- [32] T. Heinzel, *Mesoscopic Electronics in Solid State Nanostructures*. Wiley-VCH, Berlin, 2006. 19
- [33] M. S. Dresselhaus, G. Dresselhaus, and R. Saito, "Physics of carbon nanotubes," *Carbon*, vol. 33, no. 7, pp. 883–91, 1995. 19, 106
- [34] A. Javey, J. Guo, M. Paulsson, Q. Wang, D. Mann, M. Lundstrom, and H. J. Dai, "High-field quasiballistic transport in short carbon nanotubes," *Phys. Rev. Lett.*, vol. 92, p. 106804, Mar. 2004. 21, 22, 62, 103
- [35] P. L. McEuen, M. Bockrath, D. H. Cobden, Y.-G. Yoon, and S. G. Louie, "Disorder, pseudospins, and backscattering in carbon nanotubes," *Phys. Rev. Lett.*, vol. 83, pp. 5098–101, 1999. 21, 62
- [36] S. J. Wind, J. Appenzeller, and P. Avouris, "Lateral scaling in carbon-nanotube field-effect transistors," *Phys. Rev. Lett.*, vol. 91, p. 058301, Jul 2003. 21, 28, 62
- [37] A. Javey, J. Guo, Q. Wang, M. Lundstrom, and H. Dai, "Ballistic carbon nanotube field-effect transistors," *Nature*, vol. 424, pp. 654–657, Aug. 2003. 21, 62
- [38] J. Kong, E. Yenilmez, T. W. Tombler, W. Kim, H. Dai, R. B. Laughlin, L. Liu, C. S. Jayanthi, and S. Y. Wu, "Quantum interference and ballistic transmission in nanotube electron waveguides," *Phys. Rev. Lett.*, vol. 87, p. 106801, Aug 2001. 21, 62
- [39] D. Mann, A. Javey, J. Kong, Q. Wang, and H. Dai, "Ballistic transport in metallic nanotubes with reliable pd ohmic contacts," *Nano Lett.*, vol. 3, no. 11, pp. 1541–1544, 2003. 21, 26, 27
- [40] W. Liang, M. Bockrath, and H. Park, "Shell filling and exchange coupling in metallic single-walled carbon nanotubes," *Phys. Rev. Lett.*, vol. 88, p. 126801, Mar 2002. 24
- [41] J. Kondo, "Resistance minimum in dilute magnetic alloys," *Progr. Theor. Phys.*, vol. 32, no. 1, p. 37, 1964. 25
- [42] L. I. Glazman and M. É. Raikh, "Resonant kondo transparency of a barrier with quasilocal impurity states," *JETP Lett.*, vol. 47, pp. 452–455, Apr. 1988. 25
- [43] P. Jarillo-Herrero, J. Kong, H. S. J. van der Zant, C. Dekker, L. P. Kouwenhoven, and S. D. Franceschi, "Electronic transport spectroscopy of carbon nanotubes in a magnetic field," *Phys. Rev. Lett.*, vol. 94, no. 15, p. 156802, 2005. 25
- [44] R. Martel, V. Derycke, C. Lavoie, J. Appenzeller, K. K. Chan, J. Tersoff, and P. Avouris, "Ambipolar electrical transport in semiconducting single-wall carbon nanotubes," *Phys. Rev. Lett.*, vol. 87, p. 256805, Dec 2001. 26, 39
- [45] B. Babić, *Electrical Characterization of Carbon Nanotubes grown by the Chemical Vapor Deposition Method*. PhD thesis, Philosophisch-Naturwissenschaftlichen Fakultät der Universität Basel, 2004. 26, 27, 106
- [46] R. Martel, T. Schmidt, H. R. Shea, T. Hertel, and P. Avouris, "Single- and multi-wall carbon nanotube field-effect transistors," *Appl. Phys. Lett.*, vol. 73, no. 17, pp. 2447–2449, 1998. 26, 28
- [47] S. J. Tans, A. R. M. Verschueren, and C. Dekker, "Room-temperature transistor based on a single carbon nanotube," *Nature*, vol. 393, pp. 49–52, 1998. 26, 28, 62
- [48] J. Appenzeller, J. Knoch, V. Derycke, R. Martel, S. Wind, and P. Avouris, "Field-modulated carrier transport in carbon nanotube transistors," *Phys. Rev. Lett.*, vol. 89, p. 126801, Aug 2002. 27, 28
- [49] S. Heinze, J. Tersoff, R. Martel, V. Derycke, J. Appenzeller, and P. Avouris, "Carbon nanotubes as schottky barrier transistors," *Phys. Rev. Lett.*, vol. 89, p. 106801, Aug 2002. 27, 28
- [50] M. Freitag, M. Radosavljevic, Y. Zhou, A. T. Johnson, and W. F. Smith, "Controlled creation of a carbon

- nanotube diode by a scanned gate,” *Appl. Phys. Lett.*, vol. 79, no. 20, pp. 3326–3328, 2001. 27
- [51] K. Grove-Rasmussen, H. I. Jorgensen, and P. E. Lindelof, “Fabry-perot interference, kondo effect and coulomb blockade in carbon nanotubes,” *Physica E*, vol. 40, p. 92, 2007. 27, 108, 110
- [52] X. D. Cui, M. Freitag, R. Martel, L. Brus, and P. Avouris, “Controlling energy-level alignments at carbon nanotube/au contacts,” *Nano Lett.*, vol. 3, pp. 783–787, June 2003. 27
- [53] V. Derycke, R. Martel, J. Appenzeller, and P. Avouris, “Controlling doping and carrier injection in carbon nanotube transistors,” *Appl. Phys. Lett.*, vol. 80, no. 15, pp. 2773–2775, 2002. 27
- [54] T. Yamada, “Modeling of carbon nanotube schottky barrier modulation under oxidizing conditions,” *Phys. Rev. B*, vol. 69, no. 12, p. 125408, 2004. 27
- [55] A. Javey, J. Guo, D. Farmer, Q. Wang, D. Wang, R. Gordon, M. Lundstrom, and H. Dai, “Carbon nanotube field-effect transistors with integrated ohmic contacts and high- κ gate dielectrics,” *Nano Lett.*, vol. 4, no. 3, pp. 447–450, 2004. 28
- [56] R. Saito, G. Dresselhaus, and M. S. Dresselhaus, *Physical Properties of Carbon Nanotubes*. Imperial College Press, 1998. 29, 31, 35
- [57] K. S. Novoselov, A. K. Geim, S. V. Morozov, D. Jiang, Y. Zhang, S. V. Dubonos, I. V. Grigorieva, and A. A. Firsov, “Electric field effect in atomically thin carbon films,” *Science*, vol. 306, pp. 666–669, Oct. 2004. 29
- [58] A. K. Geim and K. S. Novoselov, “The rise of graphene,” *Nat. Mater.*, vol. 6, pp. 183–191, Mar. 2007. 29, 30
- [59] S. Reich, J. Maultzsch, C. Thomsen, and P. Ordejón, “Tight-binding description of graphene,” *Phys. Rev. B*, vol. 66, p. 035412, Jul 2002. 31, 37
- [60] N. Hamada, S. ichi Sawada, and A. Oshiyama, “New one-dimensional conductors: Graphitic microtubules,” *Phys. Rev. Lett.*, vol. 68, no. 10, pp. 1579–81, 1992. 35
- [61] J. W. G. Wildoer, L. C. Venema, A. G. Rinzler, R. E. Smalley, and C. Dekker, “Electronic structure of atomically resolved carbon nanotubes,” *Nature*, vol. 391, pp. 59–62, 1998. 35
- [62] P. Kim, T. W. Odom, J.-L. Huang, and C. M. Lieber, “Electronic density of states of atomically resolved single-walled carbon nanotubes: Van hove singularities and end states,” *Phys. Rev. Lett.*, vol. 82, no. 6, pp. 1225–28, 1999. 37
- [63] P. Kim, T. W. Odom, J. Huang, and C. M. Lieber, “Stm study of single-walled carbon nanotubes,” *Carbon*, vol. 38, pp. 1741–44, 2000. 37
- [64] V. N. Popov, “Curvature effects on the structural, electronic and optical properties of isolated single-walled carbon nanotubes within a symmetry-adapted non-orthogonal tight-binding model,” *New Journal of Physics*, vol. 6, p. 17, 2004. 37
- [65] H. Kataura, Y. Kumazawa, Y. Maniwa, I. Umezu, S. Suzuki, Y. Ohtsuka, and Y. Achiba, “Optical properties of single-wall carbon nanotubes,” *Synth. Met.*, vol. 103, pp. 2555–2558, June 1999. 37
- [66] R. Saito, G. Dresselhaus, and M. S. Dresselhaus, “Trigonal warping effect of carbon nanotubes,” *Phys. Rev. B*, vol. 61, pp. 2981–2990, Jan 2000. 37
- [67] B. W. Smith, M. Monthieux, and D. E. Luzzi, “Encapsulated c-60 in carbon nanotubes,” *Nature*, vol. 396, pp. 323–324, Nov. 1998. 40
- [68] H. Shiozawa, H. Rauf, T. Pichler, D. Grimm, X. Liu, M. Knupfer, M. Kalbac, S. Yang, L. Dunsch, B. Buchner, and D. Batchelor, “Electronic structure of the trimetal nitride fullerene $\text{dy}_3\text{n@c}_80$,” *Phys. Rev. B*, vol. 72, p. 195409, Nov. 2005. 40
- [69] H. Shiozawa, H. Rauf, T. Pichler, M. Knupfer, M. Kalbac, S. Yang, L. Dunsch, B. Buechner, D. Batchelor, and H. Kataura, “Filling factor and electronic structure of $\text{dy}_3\text{n@c}_80$ filled single-wall carbon nanotubes studied by photoemission spectroscopy,” *Phys. Rev. B*, vol. 73, p. 205411, May 2006. 40
- [70] H. Shiozawa, T. Pichler, C. Kramberger, A. Gruneis, M. Knupfer, B. Buchner, V. Zolyomi, J. Koltai, J. Kurti, D. Batchelor, and H. Kataura, “Fine-tuning the functional properties of carbon nanotubes via the interconversion of encapsulated molecules,” *submitted to Phys. Rev. Lett.*, 2007. 40
- [71] H. Shiozawa, T. Pichler, A. Gruneis, R. Pfeiffer, H. Kuzmany, Z. Liu, K. Suenaga, and H. Kataura, “Catalytic reaction inside a single-wall carbon nanotube,” *submitted to Advanced Materials*, 2007. 40
- [72] M. S. Arnold, A. A. Green, J. F. Hulvat, S. I. Stupp, and M. C. Hersam, “Sorting carbon nanotubes by electronic structure using density differentiation,” *Nat. Nanotech.*, vol. 1, pp. 60–65, Oct. 2006. 40
- [73] M. Zheng, A. Jagota, E. D. Semke, B. A. Diner, R. S. Mclean, S. R. Lustig, R. E. Richardson, and N. G. Tassi, “Dna-assisted dispersion and separation of carbon nanotubes,” *Nat. Mater.*, vol. 2, pp. 338–342, May 2003. 40
- [74] A. Penicaud, P. Poulin, A. Derre, E. Anglaret, and P. Petit, “Spontaneous dissolution of a single-wall carbon nanotube salt,” *J. Am. Chem. Soc.*, vol. 127, no. 1, pp. 8–9, 2005. 40
- [75] R. Krupke, F. Hennrich, H. von Lohneysen, and M. M. Kappes, “Separation of metallic from semiconducting

- single-walled carbon nanotubes," *Science*, vol. 301, pp. 344–347, July 2003. 40
- [76] D. Grimm, A. Gruneis, C. Kramberger, M. Rummeli, T. Gemming, B. Buchner, A. Barreiro, H. Kuzmany, R. Pfeiffer, and T. Pichler, "Catalytic decomposition of n-heptane for the growth of high quality single wall carbon nanotubes," *Chem. Phys. Lett.*, vol. 428, pp. 416–420, Sept. 2006. 40, 44
- [77] J. Kong, H. T. Soh, A. M. Cassell, C. F. Quate, and H. Dai, "Synthesis of individual single-walled carbon nanotubes on patterned silicon wafers," *Nature*, vol. 395, pp. 878–881, Oct. 1998. 40, 51
- [78] L. Huang, B. White, M. Sfeir, M. Huang, H. Huang, S. Wind, J. Hone, and S. O'Brien, "Cobalt ultrathin film catalyzed ethanol chemical vapor deposition of single-walled carbon nanotubes," *J. Phys. Chem. B*, vol. 110, no. 23, pp. 11103–11109, 2006. 40, 42
- [79] S. M. Huang, X. Y. Cai, C. S. Du, and J. Liu, "Oriented long single walled carbon nanotubes on substrates from floating catalysts," *J. Phys. Chem. B*, vol. 107, pp. 13251–13254, Dec. 2003. 40
- [80] S. M. Huang, M. Woodson, R. Smalley, and J. Liu, "Growth mechanism of oriented long single walled carbon nanotubes using "fast-heating" chemical vapor deposition process," *Nano Lett.*, vol. 4, pp. 1025–1028, June 2004. 40
- [81] Y. G. Zhang, A. L. Chang, J. Cao, Q. Wang, W. Kim, Y. M. Li, N. Morris, E. Yenilmez, J. Kong, and H. J. Dai, "Electric-field-directed growth of aligned single-walled carbon nanotubes," *Appl. Phys. Lett.*, vol. 79, pp. 3155–3157, Nov. 2001. 40
- [82] A. Ural, Y. M. Li, and H. J. Dai, "Electric-field-aligned growth of single-walled carbon nanotubes on surfaces," *Appl. Phys. Lett.*, vol. 81, pp. 3464–3466, Oct. 2002. 40
- [83] T. Brintlinger, Y.-F. Chen, T. Dürkop, E. Cobas, M. S. Fuhrer, J. D. Barry, and J. Melngailis, "Rapid imaging of nanotubes on insulating substrates," *Appl. Phys. Lett.*, vol. 81, no. 13, pp. 2454–2456, 2002. 42
- [84] L.-C. Qin, X. Zhao, K. Hirahara, Y. Miyamoto, Y. Ando, and S. Iijima, "The smallest carbon nanotube," *Nature*, vol. 408, p. 50, 2000. 42
- [85] N. Wang, Z. K. Tang, G. G. Li, and J. S. Chen, "Single-walled 4â carbon nanotube arrays," *Nature*, vol. 408, pp. 50–51, 2000. 42
- [86] L. X. Zheng, M. J. O'Connell, S. K. Doorn, X. Z. Liao, Y. H. Zhao, E. A. Akhador, M. A. Hoffbauer, B. J. Roop, Q. X. Jia, R. C. Dye, D. E. Peterson, S. M. Huang, J. Liu, and Y. T. Zhu, "Ultralong single-wall carbon nanotubes," *Nat. Mater.*, vol. 3, pp. 673–676, Oct. 2004. 42, 43
- [87] M. Rummeli, M. Löffler, C. Kramberger, F. Simon, F. Fulop, O. Jost, R. Schonfelder, A. Gruneis, T. Gemming, W. Pompe, B. Buchner, and T. Pichler, "Isotope-engineered single-wall carbon nanotubes; a key material for magnetic studies," *J. Phys. Chem. C*, vol. 111, no. 11, pp. 4094–4098, 2007. 42
- [88] S. Bhaviripudi, E. Mile, S. Steiner, A. Zare, M. Dresselhaus, A. Belcher, and J. Kong, "Cvd synthesis of single-walled carbon nanotubes from gold nanoparticle catalysts," *J. Am. Chem. Soc.*, vol. 129, no. 6, pp. 1516–1517, 2007. 42
- [89] H. Rauf, T. Pichler, M. Knupfer, J. Fink, and H. Kataura, "Transition from a tomonaga-luttinger liquid to a fermi liquid in potassium-intercalated bundles of single-wall carbon nanotubes," *Phys. Rev. Lett.*, vol. 93, no. 9, p. 096805, 2004. 43
- [90] A. Barreiro, C. Kramberger, M. Rummeli, A. Gruneis, D. Grimm, S. Hampel, T. Gemming, B. Buchner, A. Bachtold, and T. Pichler, "Control of the single-wall carbon nanotube mean diameter in sulphur promoted aerosol-assisted chemical vapour deposition," *Carbon*, vol. 45, pp. 55–61, 2007. 43
- [91] A. Gruneis, M. H. Rummeli, C. Kramberger, D. Grimm, T. Gemming, A. Barreiro, P. Ayala, T. Pichler, H. Kuzmany, C. Schamann, R. Pfeiffer, J. Schumann, and B. Buchner, "Growth of carbon nanotubes from wet chemistry and thin film multilayer catalysts," *phys. stat. sol. (b)*, vol. 243, no. 13, pp. 3054–3057, 2006. 44, 47, 48
- [92] A. Gruneis, C. Kramberger, D. Grimm, T. Gemming, M. H. Rummeli, A. Barreiro, P. Ayala, T. Pichler, C. Schaman, H. Kuzmany, J. Schumann, and B. Buchner, "Eutectic limit for the growth of carbon nanotubes from a thin iron film by chemical vapor deposition of cyclohexane," *Chem. Phys. Lett.*, vol. 425, pp. 301–305, July 2006. 43, 44
- [93] P. Ayala, A. Gruneis, D. Grimm, C. Kramberger, R. Engelhard, M. Rummeli, J. Schumann, R. Kaltofen, B. Buchner, C. Schaman, H. Kuzmany, T. Gemming, A. Barreiro, and T. Pichler, "Cyclohexane triggers staged growth of pure and vertically aligned single wall carbon nanotubes." accepted at *Chem. Phys. Lett.* 44
- [94] A. Gruneis, M. Rummeli, C. Kramberger, A. Barreiro, T. Pichler, R. Pfeiffer, H. Kuzmany, T. Gemming, and B. Büchner, "High quality double wall carbon nanotubes with a defined diameter distribution by chemical vapor deposition from alcohol," *Carbon*, vol. 44, pp. 3177–3182, 2006. 44, 70
- [95] F. Schaffel, C. Kramberger, M. Rummeli, D. Grimm, E. Mohn, T. Gemming, T. Pichler, B. Rellinghaus, B. Buchner, and L. Schultz, "Nanoengineered catalyst particles as a key for tailor-made carbon nanotubes," *Chem. Mater.*, vol. 19, no. 20, pp. 5006–5009, 2007. 44

- [96] F. Schaffel, C. Kramberger, M. H. Rummeli, R. Kaltofen, D. Grimm, A. Gruneis, E. Mohn, T. Gemming, T. Pichler, B. Buchner, B. Rellinghaus, and L. Schultz, "Carbon nanotubes grown from individual gas phase prepared iron catalyst particles," *phys. stat. sol. (a)*, vol. 204, no. 6, pp. 1786–1790, 2007. 44
- [97] P. Ayala, A. Gruneis, T. Gemming, B. Buchner, M. H. Rummeli, D. Grimm, J. Schumann, R. Kaltofen, F. L. Freire Jr., H. D. F. Filho, and T. Pichler, "Influence of the catalyst hydrogen pretreatment on the growth of vertically aligned nitrogen-doped carbon nanotubes," *Chem. Mater.*, vol. 19, no. 25, pp. 6131–6137, 2007. 44
- [98] P. Ayala, A. Gruneis, T. Gemming, D. Grimm, C. Kramberger, M. Rummeli, F. Freire, H. Kuzmany, R. Pfeiffer, A. Barreiro, B. Buchner, and T. Pichler, "Tailoring n-doped single and double wall carbon nanotubes from a nondiluted carbon/nitrogen feedstock," *J. Phys. Chem. C*, vol. 111, no. 7, pp. 2879–2884, 2007. 44
- [99] T. Douglas and V. T. Stark, "Nanophase cobalt oxyhydroxide mineral synthesized within the protein cage of ferritin," *Inorg. Chem.*, vol. 39, pp. 1828–1830, Apr. 2000. 44
- [100] F. Tuinstra and J. L. Koenig, "Raman spectrum of graphite," *The Journal of Chemical Physics*, vol. 53, no. 3, pp. 1126–1130, 1970. 46
- [101] L. G. Cancado, M. A. Pimenta, B. R. A. Neves, M. S. S. Dantas, and A. Jorio, "Influence of the atomic structure on the raman spectra of graphite edges," *Phys. Rev. Lett.*, vol. 93, no. 24, p. 247401, 2004. 46
- [102] C. Fantini, A. Jorio, M. Souza, M. S. Strano, M. S. Dresselhaus, and M. A. Pimenta, "Optical transition energies for carbon nanotubes from resonant raman spectroscopy: Environment and temperature effects," *Phys. Rev. Lett.*, vol. 93, no. 14, p. 147406, 2004. 47, 48
- [103] S. Maruyama, R. Kojima, Y. Miyauchi, S. Chiashi, and M. Kohno, "Low-temperature synthesis of high-purity single-walled carbon nanotubes from alcohol," *Chem. Phys. Lett.*, vol. 360, pp. 229–234, July 2002. 47
- [104] Y. Murakami, Y. Miyauchi, S. Chiashi, and S. Maruyama, "Direct synthesis of high-quality single-walled carbon nanotubes on silicon and quartz substrates," *Chem. Phys. Lett.*, vol. 377, pp. 49–54, Aug. 2003. 48
- [105] Y. R. Jeng, P. C. Tsai, and T. H. Fang, "Molecular-dynamics studies of bending mechanical properties of empty and c-60-filled carbon nanotubes under nanoindentation," *J. Chem. Phys.*, vol. 122, p. 224713, June 2005. 51, 65
- [106] G.-H. Jeong, S. Suzuki, Y. Kobayashi, A. Yamazaki, H. Yoshimura, and Y. Homma, "Size control of catalytic nanoparticles by thermal treatment and its application to diameter control of single-walled carbon nanotubes," *Appl. Phys. Lett.*, vol. 90, no. 4, p. 043108, 2007. 51
- [107] J. Lefebvre, Y. Homma, and P. Finnie, "Bright band gap photoluminescence from unprocessed single-walled carbon nanotubes," *Phys. Rev. Lett.*, vol. 90, p. 217401, May 2003. 54
- [108] M. Y. Sfeir, F. Wang, L. Huang, C.-C. Chuang, J. Hone, S. P. O'Brien, T. F. Heinz, and L. E. Brus, "Probing electronic transitions in individual carbon nanotubes by rayleigh scattering," *Science*, vol. 306, no. 5701, pp. 1540–1543, 2004. 54
- [109] B. Chandra, R. Caldwell, M. Huang, L. Huang, M. Y. Sfeir, S. P. O'Brien, T. F. Heinz, and J. Hone, "Electrical transport measurements of nanotubes with known $(j_i n_i / i_i, j_l m_l / i_l)$ indices," *phys. stat. sol. (b)*, vol. 243, no. 13, pp. 3359–3364, 2006. 54
- [110] E. N. Economou, *Green's Functions in Quantum Physics*. Springer-Verlag Berlin, 2 ed., 1983. 59
- [111] R. Kubo, "Statistical-mechanical theory of irreversible processes. i. general theory and simple applications to magnetic and conduction problems," *J. Phys. Soc. Jpn.*, vol. 12, no. 6, pp. 570–586, 1957. 59, 61
- [112] M. B. Nardelli, "Electronic transport in extended systems: Application to carbon nanotubes," *Phys. Rev. B*, vol. 60, pp. 7828–7833, Sept. 1999. 59, 60
- [113] D. Grimm, R. B. Muniz, and A. Latgé, "From straight carbon nanotubes to y-shaped junctions and rings," *Phys. Rev. B*, vol. 68, p. 193407, Nov. 2003. 59, 73, 90
- [114] A. Latgé, D. Grimm, and P. Venezuela, "Y-shaped carbon nanotubes: structural stability and transport properties," *J. Mol. Catal. A: Chem.*, vol. 228, pp. 125–130, Mar. 2005. 59, 60, 73, 81
- [115] M. S. Ferreira, T. G. Dargam, R. B. Muniz, and A. Latgé, "Radial oscillations of local density of states in carbon nanotubes," *Phys. Rev. B*, vol. 6324, p. 245111, June 2001. 60
- [116] C. G. Rocha, T. G. Dargam, and A. Latgé, "Electronic states in zigzag carbon nanotube quantum dots," *Phys. Rev. B*, vol. 65, p. 165431, Apr. 2002. 60, 90
- [117] J. Mathon, M. Villeret, and H. Itoh, "Selection-rules for oscillations of the giant magnetoresistance with nonmagnetic spacer layer thickness," *Phys. Rev. B*, vol. 52, pp. R6983–R6986, Sept. 1995. 61
- [118] S. J. Tans, M. Devoret, H. Dai, A. Thess, R. Smalley, L. Geerligs, and C. Dekker, "Individual single-wall carbon nanotubes as quantum wires," *Nature*, vol. 386, pp. 474–77, 1997. 62
- [119] H. R. Shea, R. Martel, and P. Avouris, "Electrical transport in rings of single-wall nanotubes: One-dimensional localization," *Phys. Rev. Lett.*, vol. 84, no. 19, pp. 4441–4444, 2000. 62
- [120] C. T. White and T. N. Todorov, "Carbon nanotubes as long ballistic conductors," *Nature*, vol. 393, pp. 240–42, 1998. 62

- [121] Y. S. Lee, M. B. Nardelli, and N. Marzari, "Band structure and quantum conductance of nanostructures from maximally localized wannier functions: The case of functionalized carbon nanotubes," *Phys. Rev. Lett.*, vol. 95, p. 076804, Aug. 2005. [62](#)
- [122] S. Frank, P. Poncharal, Z. L. Wang, and W. A. Heer, "Carbon nanotube quantum resistors," *Science*, vol. 280, no. 5370, pp. 1744–1746, 1998. [62](#)
- [123] A. Krishnan, E. Dujardin, T. W. Ebbesen, P. N. Yianilos, and M. M. J. Treacy, "Young's modulus of single-walled nanotubes," *Phys. Rev. B*, vol. 58, pp. 14013–14019, Nov 1998. [63](#)
- [124] M.-F. Yu, B. S. Files, S. Arepalli, and R. S. Ruoff, "Tensile loading of ropes of single wall carbon nanotubes and their mechanical properties," *Phys. Rev. Lett.*, vol. 84, pp. 5552–5555, Jun 2000. [63](#), [84](#)
- [125] K. Asaka and T. Kizuka, "Atomistic dynamics of deformation, fracture, and joining of individual single-walled carbon nanotubes," *Phys. Rev. B*, vol. 72, no. 11, p. 115431, 2005. [63](#)
- [126] C. Q. Ru, "Elastic buckling of single-walled carbon nanotube ropes under high pressure," *Phys. Rev. B*, vol. 62, pp. 10405–10408, Oct 2000. [63](#)
- [127] M. Marques, H. Troiani, M. Miki-Yoshida, M. Jose-Yacaman, and A. Rubio, "On the breaking of carbon nanotubes under tension," *Nano Lett.*, vol. 4, no. 5, pp. 811–815, 2004. [63](#), [84](#)
- [128] N. Chandra, S. Namila, and C. Shet, "Local elastic properties of carbon nanotubes in the presence of stone-wales defects," *Phys. Rev. B*, vol. 69, no. 9, p. 094101, 2004. [63](#), [84](#)
- [129] N. Metropolis, A. W. Rosenbluth, M. N. Rosenbluth, A. H. Teller, and E. Teller, "Equation of state calculations by fast computing machines," *The Journal of Chemical Physics*, vol. 21, no. 6, pp. 1087–1092, 1953. [64](#)
- [130] M. P. Allen and D. J. Tildesley, *Computer Simulation of Liquids*. Clarendon Press, Oxford, 1989. ISBN-13: 978-0-19-855645-9. [64](#)
- [131] J. Tersoff, "New empirical approach for the structure and energy of covalent systems," *Phys. Rev. B*, vol. 37, pp. 6991–7000, Apr 1988. [64](#), [65](#)
- [132] J. Tersoff, "Empirical interatomic potential for carbon, with applications to amorphous carbon," *Phys. Rev. Lett.*, vol. 61, pp. 2879–2882, Dec 1988. [64](#)
- [133] J. Tersoff, "Modeling solid-state chemistry: Interatomic potentials for multicomponent systems," *Phys. Rev. B*, vol. 39, pp. 5566–5568, Mar 1989. [64](#)
- [134] I. Jang, S. Sinnott, D. Danailov, and P. Keblinski, "Molecular dynamics simulation study of carbon nanotube welding under electron beam irradiation," *Nano Lett.*, vol. 4, no. 1, pp. 109–114, 2004. [65](#), [80](#)
- [135] P. K. Schelling and P. Keblinski, "Thermal expansion of carbon structures," *Phys. Rev. B*, vol. 68, p. 035425, Jul 2003. [65](#), [83](#)
- [136] N. R. Narayana, P. Keblinski, A. M. Rao, M. S. Dresselhaus, L. S. Schadler, and P. M. Ajayan, "Temperature dependence of radial breathing mode raman frequency of single-walled carbon nanotubes," *Phys. Rev. B*, vol. 66, p. 235424, Dec 2002. [65](#), [83](#)
- [137] L.-M. Peng, Z. L. Zhang, Z. Q. Xue, Q. D. Wu, Z. N. Gu, and D. G. Pettifor, "Stability of carbon nanotubes: How small can they be?," *Phys. Rev. Lett.*, vol. 85, pp. 3249–3252, Oct 2000. [65](#)
- [138] M. Terrones, H. Terrones, F. Banhart, J. C. Charlier, and P. M. Ajayan, "Coalescence of single-walled carbon nanotubes," *Science*, vol. 288, pp. 1226–1229, May 2000. [65](#), [73](#), [80](#), [81](#)
- [139] S.-i. Sawada and N. Hamada, "Energetics of carbon nano-tubes," *Solid State Commun.*, vol. 83, pp. 917–919, Sept. 1992. [65](#)
- [140] A. Maiti, A. Svizhenko, and M. P. Anantram, "Electronic transport through carbon nanotubes: Effects of structural deformation and tube chirality," *Phys. Rev. Lett.*, vol. 88, p. 126805, Mar 2002. [65](#)
- [141] L. Yang and J. Han, "Electronic structure of deformed carbon nanotubes," *Phys. Rev. Lett.*, vol. 85, pp. 154–157, Jul 2000. [65](#)
- [142] M. S. Tang, C. Z. Wang, C. T. Chan, and K. M. Ho, "Environment-dependent tight-binding potential model," *Phys. Rev. B*, vol. 53, pp. 979–982, Jan 1996. [66](#)
- [143] S. Ogata and Y. Shibutani, "Ideal tensile strength and band gap of single-walled carbon nanotubes," *Phys. Rev. B*, vol. 68, p. 165409, Oct. 2003. [66](#)
- [144] C. H. Lee, W. R. L. Lambrecht, B. Segall, P. C. Kelires, T. Frauenheim, and U. Stephan, "Electronic structure of dense amorphous carbon," *Phys. Rev. B*, vol. 49, pp. 11448–11451, Apr 1994. [66](#)
- [145] A. G. Aronov and Y. V. Sharvin, "Magnetic-flux effects in disordered conductors," *Rev. Mod. Phys.*, vol. 59, pp. 755–779, July 1987. [66](#)
- [146] V. Chandrasekhar, M. J. Rooks, S. Wind, and D. E. Prober, "Observation of aharonov-bohm electron interference effects with periods h/e and $h/2e$ in individual micron-size, normal-metal rings," *Phys. Rev. Lett.*, vol. 55, no. 15, pp. 1610–1613, 1985. [66](#)
- [147] Y. Aharonov and D. Bohm, "Significance of electromagnetic potentials in the quantum theory," *Phys. Rev.*,

- vol. 115, no. 3, pp. 485–491, 1959. 66
- [148] J. M. Luttinger, “The effect of a magnetic field on electrons in a periodic potential,” *Phys. Rev.*, vol. 84, pp. 814–817, Nov 1951. 67
- [149] H. Ajiki and T. Ando, “Electronic states of carbon nanotubes,” *J. Phys. Soc. Jpn.*, vol. 62, pp. 1255–1266, Apr. 1993. 68, 69
- [150] T. Shimada, T. Sugai, Y. Ohno, S. Kishimoto, T. Mizutani, H. Yoshida, T. Okazaki, and H. Shinohara, “Double-wall carbon nanotube field-effect transistors: Ambipolar transport characteristics,” *Appl. Phys. Lett.*, vol. 84, pp. 2412–2414, Mar. 2004. 70
- [151] S. Bando, M. Takizawa, K. Hirahara, M. Yudasaka, and S. Iijima, “Raman scattering study of double-wall carbon nanotubes derived from the chains of fullerenes in single-wall carbon nanotubes,” *Chem. Phys. Lett.*, vol. 337, pp. 48–54, Mar. 2001. 70
- [152] M. Abe, H. Kataura, H. Kira, T. Kodama, S. Suzuki, Y. Achiba, K.-i. Kato, M. Takata, A. Fujiwara, K. Matsuda, and Y. Maniwa, “Structural transformation from single-wall to double-wall carbon nanotube bundles,” *Phys. Rev. B*, vol. 68, p. 041405, Jul 2003. 70
- [153] Y. Saito, T. Yoshikawa, M. Inagaki, M. Tomita, and T. Hayashi, “Growth and structure of graphitic tubules and polyhedral particles in arc-discharge,” *Chem. Phys. Lett.*, vol. 204, pp. 277–282, Mar. 1993. 70
- [154] J.-C. Charlier and J.-P. Michenaud, “Energetics of multilayered carbon tubules,” *Phys. Rev. Lett.*, vol. 70, pp. 1858–1861, Mar 1993. 70
- [155] A. H. R. Palser, “Interlayer interactions in graphite and carbon nanotubes,” *Phys. Chem. Chem. Phys.*, vol. 1, pp. 4459–4464, 1999. 70
- [156] A. Urbina, I. Echeverría, A. Pérez-Garrido, A. Díaz-Sánchez, and J. Abellán, “Quantum conductance steps in solutions of multiwalled carbon nanotubes,” *Phys. Rev. Lett.*, vol. 90, p. 106603, Mar 2003. 70
- [157] H. Kajiura, H. Huang, and A. Bezryadin, “Quasi-ballistic electron transport in double-wall carbon nanotubes,” *Chem. Phys. Lett.*, vol. 398, pp. 476–479, Nov. 2004. 70
- [158] R. Saito, R. Matsuo, T. Kimura, G. Dresselhaus, and M. S. Dresselhaus, “Anomalous potential barrier of double-wall carbon nanotube,” *Chem. Phys. Lett.*, vol. 348, pp. 187–193, Nov. 2001. 70
- [159] J. P. Lu, X. P. Li, and R. M. Martin, “Ground-state and phase-transitions in solid c-60,” *Phys. Rev. Lett.*, vol. 68, pp. 1551–1554, Mar. 1992. 70
- [160] Y. H. Ho, C. P. Chang, F. L. Shyu, R. B. Chen, S. C. Chen, and M. F. Lin, “Electronic and optical properties of double-walled armchair carbon nanotubes,” *Carbon*, vol. 42, no. 15, pp. 3159–3167, 2004. 70
- [161] G. W. Ho, Y. H. Ho, T. S. Li, C. P. Chang, and M. F. Lin, “Band structure and absorption spectrum of double-walled zigzag carbon nanotubes in an electric field,” *Carbon*, vol. 44, pp. 2323–2329, Sept. 2006. 70
- [162] S. Uryu and T. Ando, “Electronic intertube transfer in double-wall carbon nanotubes,” *Phys. Rev. B*, vol. 72, no. 24, p. 245403, 2005. 70
- [163] R. Saito, G. Dresselhaus, and M. S. Dresselhaus, “Electronic-structure of double-layer graphene tubules,” *J. Appl. Phys.*, vol. 73, pp. 494–500, Jan. 1993. 70
- [164] Y.-K. Kwon and D. Tománek, “Electronic and structural properties of multiwall carbon nanotubes,” *Phys. Rev. B*, vol. 58, pp. R16001–R16004, Dec 1998. 70, 71
- [165] K. H. Ahn, Y. H. Kim, J. Wiersig, and K. J. Chang, “Spectral correlation in incommensurate multiwalled carbon nanotubes,” *Phys. Rev. Lett.*, vol. 90, p. 026601, Jan. 2003. 70
- [166] S. Roche, F. m. c. Triozon, A. Rubio, and D. Mayou, “Conduction mechanisms and magnetotransport in multiwalled carbon nanotubes,” *Phys. Rev. B*, vol. 64, p. 121401, Sep 2001. 70
- [167] B. Gao, A. Komnik, R. Egger, D. C. Glatzli, and A. Bachtold, “Evidence for luttinger-liquid behavior in crossed metallic single-wall nanotubes,” *Phys. Rev. Lett.*, vol. 92, p. 216804, May 2004. 73
- [168] A. N. Andriotis and M. Menon, “Are electrical switching and rectification inherent properties of carbon nanotube y junctions?,” *Appl. Phys. Lett.*, vol. 89, p. 132116, Sept. 2006. 73
- [169] P. R. Bandaru, C. Daraio, S. Jin, and A. M. Rao, “Novel electrical switching behaviour and logic in carbon nanotube y-junctions,” *Nat. Mater.*, vol. 4, pp. 663–666, Sept. 2005. 73
- [170] J. Li, C. Papadopoulos, and J. Xu, “Growing y-junction carbon nanotubes,” *Nature*, vol. 402, pp. 253–54, 1999. 73
- [171] P. Nagy, R. Ehlich, L. Biró, and J. Gyulai, “Y-branching of single walled carbon nanotubes,” *Appl. Phys. A: Mater. Sci. Process.*, vol. V70, pp. 481–483, Apr. 2000. 73
- [172] Y. C. Choi and W. Choi, “Synthesis of y-junction single-wall carbon nanotubes,” *Carbon*, vol. 43, pp. 2737–2741, Nov. 2005. 73
- [173] P. M. Ajayan, V. Ravikumar, and J.-C. Charlier, “Surface reconstructions and dimensional changes in single-walled carbon nanotubes,” *Phys. Rev. Lett.*, vol. 81, pp. 1437–1440, Aug 1998. 73, 80
- [174] L. P. Biró, R. Ehlich, Z. Osváth, A. Koós, Z. E. Horvath, J. Gyulai, and J. B. Nagy, “From straight carbon

- nanotubes to y-branched and coiled carbon nanotubes," *Diamond Relat. Mater.*, vol. 11, pp. 1081–85, 2002. [73](#)
- [175] J.-P. Cleuziou, W. Wernsdorfer, V. Bouchiat, T. Ondarcuhu, and M. Monthieux, "Carbon nanotube superconducting quantum interference device," *Nat. Nanotech.*, vol. 1, pp. 53–59, Oct. 2006. [73](#)
- [176] A. Latgé, R. B. Muniz, and D. Grimm, "Carbon nanotube structures: Y-junctions and nanorings," *Braz. J. Phys.*, vol. 34, pp. 585–589, June 2004. [73](#)
- [177] D. Grimm, P. Venezuela, and A. Latgé, "Thermal and mechanical stability of y-shaped carbon nanotubes," *Phys. Rev. B*, vol. 71, p. 155425, Apr. 2005. [73](#)
- [178] D. Grimm, A. Latgé, and P. Venezuela, "Standing-wave observations in single-wall carbon nanotube quantum dots and y-junction rings," *phys. stat. sol. (b)*, vol. 244, no. 11, pp. 4283–4287, 2007. [73](#), [78](#)
- [179] D. Grimm, P. Venezuela, F. Banhart, N. Grobert, H. Terrones, P. Ajayan, M. Terrones, and A. Latgé, "Synthesis of swcnt rings made by two y junctions and possible applications in electron interferometry," *Small*, vol. 3, no. 11, pp. 1900–1905, 2007. [73](#), [78](#)
- [180] V. H. Crespi, "Relations between global and local topology in multiple nanotube junctions," *Phys. Lett. B*, vol. 58, p. 12671, 1998. [73](#)
- [181] G. E. Scuseria, "Negative curvature and hyperfullerenes," *Chem. Phys. Lett.*, vol. 195, no. 5-6, pp. 534–36, 1992. [74](#)
- [182] I. Laszlo, "A possible topological arrangement of carbon atoms at nanotube junctions," *Fullerenes Nanotubes And Carbon Nanostructures*, vol. 13, pp. 535–541, 2005. [74](#)
- [183] A. Rochefort, D. R. Salahub, and P. Avouris, "The effect of structural distortions on the electronic structure of carbon nanotubes," *Chem. Phys. Lett.*, vol. 297, pp. 45–50, 1998. [75](#)
- [184] O. Lourie, D. M. Cox, and H. D. Wagner, "Buckling and collapse of embedded carbon nanotubes," *Phys. Rev. Lett.*, vol. 81, no. 8, pp. 1638–41, 1998. [75](#)
- [185] M. A. Kanter, "Diffusion of carbon atoms in natural graphite crystals," *Phys. Rev.*, vol. 107, pp. 655–663, Aug 1957. [76](#)
- [186] E. Kaxiras and K. C. Pandey, "Energetics of defects and diffusion mechanisms in graphite," *Phys. Rev. Lett.*, vol. 61, pp. 2693–2696, Dec 1988. [76](#)
- [187] A. J. Lu and B. C. Pan, "Nature of single vacancy in achiral carbon nanotubes," *Phys. Rev. Lett.*, vol. 92, p. 105504, Mar. 2004. [76](#)
- [188] J. Rossato, R. Baierle, A. Fazzio, and R. Mota, "Vacancy formation process in carbon nanotubes: First-principles approach," *Nano Lett.*, vol. 5, no. 1, pp. 197–200, 2005. [76](#)
- [189] M. Ouyang, J. L. Huang, C. L. Cheung, and C. M. Lieber, "Atomically resolved single-walled carbon nanotube intramolecular junctions," *Science*, vol. 291, pp. 97–100, Jan. 2001. [78](#)
- [190] T. W. Ebbesen and T. Takada, "Topological and sp³ defect structures in nanotubes," *Carbon*, vol. 33, no. 7, pp. 973–978, 1995. [78](#)
- [191] J.-C. Charlier, T. W. Ebbesen, and P. Lambin, "Structural and electronic properties of pentagon-heptagon pair defects in carbon nanotubes," *Phys. Rev. B*, vol. 53, pp. 11108–11113, Apr 1996. [78](#)
- [192] D. Orlikowski, M. Buongiorno Nardelli, J. Bernholc, and C. Roland, "Ad-dimers on strained carbon nanotubes: A new route for quantum dot formation?," *Phys. Rev. Lett.*, vol. 83, pp. 4132–4135, Nov 1999. [78](#)
- [193] L. Chico, M. P. L. Sancho, and M. C. Munoz, "Carbon-nanotube-based quantum dot," *Phys. Rev. Lett.*, vol. 81, pp. 1278–1281, Aug. 1998. [78](#), [97](#)
- [194] L. Chico and W. Jaskolski, "Localized states and conductance gaps in metallic carbon nanotubes," *Phys. Rev. B*, vol. 69, p. 085406, Feb. 2004. [78](#), [97](#)
- [195] C. Journet, W. K. Maser, P. Bernier, A. Loiseau, M. L. delaChapelle, S. Lefrant, P. Deniard, R. Lee, and J. E. Fischer, "Large-scale production of single-walled carbon nanotubes by the electric-arc technique," *Nature*, vol. 388, pp. 756–758, Aug. 1997. [78](#)
- [196] P. Nikolaev, M. J. Bronikowski, R. K. Bradley, F. Rohmund, D. T. Colbert, K. A. Smith, and R. E. Smalley, "Gas-phase catalytic growth of single-walled carbon nanotubes from carbon monoxide," *Chem. Phys. Lett.*, vol. 313, pp. 91–97, Nov. 1999. [78](#)
- [197] M. Yoon, S. W. Han, G. Kim, S. B. Lee, S. Berber, E. Osawa, J. Ihm, M. Terrones, F. Banhart, J. C. Charlier, N. Grobert, H. Terrones, P. M. Ajayan, and D. Tomanek, "Zipper mechanism of nanotube fusion: Theory and experiment," *Phys. Rev. Lett.*, vol. 92, p. 075504, Feb. 2004. [79](#)
- [198] E. Hernandez, V. Meunier, B. Smith, R. Rurali, H. Terrones, M. BuongiornoNardelli, M. Terrones, D. Luzzi, and J.-C. Charlier, "Fullerene coalescence in nanopeapods: A path to novel tubular carbon," *Nano Lett.*, vol. 3, no. 8, pp. 1037–1042, 2003. [80](#)
- [199] T. Yuzvinsky, W. Mickelson, S. Aloni, G. Begtrup, A. Kis, and A. Zettl, "Shrinking a carbon nanotube," *Nano Lett.*, vol. 6, no. 12, pp. 2718–2722, 2006. [80](#)

- [200] G. Dereli, B. Sungu, and C. Ozdogan, "Thermal stability of metallic single-walled carbon nanotubes: an o(n) tight-binding molecular dynamics simulation study," *Nanotechn.*, vol. 18, p. 245704, June 2007. 82
- [201] M. J. Lopez, A. Rubio, and J. A. Alonso, "Deformations and thermal stability of carbon nanotube ropes," *IEEE T. Nanotechnol.*, vol. 3, pp. 230–236, June 2004. 82
- [202] M. J. Lopez, A. Rubio, J. A. Alonso, S. Lefrant, K. Metenier, and S. Bonnamy, "Patching and tearing single-wall carbon-nanotube ropes into multiwall carbon nanotubes," *Phys. Rev. Lett.*, vol. 89, p. 255501, Nov 2002. 82
- [203] K. Metenier, S. Bonnamy, F. Beguin, C. Journet, P. Bernier, M. L. de La Chapelle, O. Chauvet, and S. Lefrant, "Coalescence of single-walled carbon nanotubes and formation of multi-walled carbon nanotubes under high-temperature treatments," *Carbon*, vol. 40, no. 10, pp. 1765–1773, 2002. 82
- [204] M. Yudasaka, T. Ichihashi, D. Kasuya, H. Kataura, and S. Iijima, "Structure changes of single-wall carbon nanotubes and single-wall carbon nanohorns caused by heat treatment," *Carbon*, vol. 41, no. 6, pp. 1273–1280, 2003. 82
- [205] Y. Yosida, "High-temperature shrinkage of single-walled carbon nanotube bundles up to 1600 k," *J. Appl. Phys.*, vol. 87, pp. 3338–3341, Apr. 2000. 83
- [206] Y. Maniwa, R. Fujiwara, H. Kira, H. Tou, H. Kataura, S. Suzuki, Y. Achiba, E. Nishibori, M. Takata, M. Sakata, A. Fujiwara, and H. Suematsu, "Thermal expansion of single-walled carbon nanotube (swnt) bundles: X-ray diffraction studies," *Phys. Rev. B*, vol. 64, p. 241402, Nov 2001. 83
- [207] C. Li and T.-W. Chou, "Axial and radial thermal expansions of single-walled carbon nanotubes," *Phys. Rev. B*, vol. 71, no. 23, p. 235414, 2005. 83
- [208] C. Y. Wei, K. J. Cho, and D. Srivastava, "Tensile strength of carbon nanotubes under realistic temperature and strain rate," *Phys. Rev. B*, vol. 67, p. 115407, Mar. 2003. 84
- [209] G. Guhados, W. K. Wan, X. L. Sun, and J. L. Hutter, "Simultaneous measurement of young's and shear moduli of multiwalled carbon nanotubes using atomic force microscopy," *J. Appl. Phys.*, vol. 101, p. 033514, Feb. 2007. 84
- [210] M. B. Nardelli, B. I. Yakobson, and J. Bernholc, "Brittle and ductile behavior in carbon nanotubes," *Phys. Rev. Lett.*, vol. 81, pp. 4656–4659, Nov 1998. 84
- [211] Q. Zhao, M. B. Nardelli, and J. Bernholc, "Ultimate strength of carbon nanotubes: A theoretical study," *Phys. Rev. B*, vol. 65, p. 144105, Mar 2002. 84
- [212] F. L. Hu, H. T. Yang, X. P. Yang, and J. M. Dong, "Electronic transport and fano resonance in carbon nanotube ring systems," *Phys. Rev. B*, vol. 73, p. 235437, June 2006. 90
- [213] P. G. Collins, K. Bradley, M. Ishigami, and A. Zettl, "Extreme oxygen sensitivity of electronic properties of carbon nanotubes," *Science*, vol. 287, pp. 1801–04, 2000. 100
- [214] M. Radosavljevic, M. Freitag, K. Thadani, and A. Johnson, "Nonvolatile molecular memory elements based on ambipolar nanotube field effect transistors," *Nano Lett.*, vol. 2, no. 7, pp. 761–764, 2002. 100
- [215] W. Kim, A. Javey, O. Vermesh, Q. Wang, Y. Li, and H. Dai, "Hysteresis caused by water molecules in carbon nanotube field-effect transistors," *Nano Lett.*, vol. 3, no. 2, pp. 193–198, 2003. 100, 106
- [216] Z. Yao, C. L. Kane, and C. Dekker, "High-field electrical transport in single-wall carbon nanotubes," *Phys. Rev. Lett.*, vol. 84, pp. 2941–2944, Mar 2000. 103
- [217] B. Babic, T. Kontos, and C. Schönberger, "Kondo effect in carbon nanotubes at half filling," *Phys. Rev. B*, vol. 70, p. 235419, Dec 2004. 106
- [218] L. P. Kouwenhoven, A. T. Johnson, N. C. van der Vaart, C. J. P. M. Harmans, and C. T. Foxon, "Quantized current in a quantum-dot turnstile using oscillating tunnel barriers," *Phys. Rev. Lett.*, vol. 67, pp. 1626–1629, Sep 1991. 106
- [219] L. Kouwenhoven, C. Marcus, P. McEuen, S. Tarucha, R. Westervelt, and N. Wingreen, *Electron transport in quantum dots*, vol. Kluwer Series E345, p. 105–214. Proceedings of the NATO Advanced Study Institute on Mesoscopic Electron Transport, 1997. 107, 108
- [220] D. V. Averin, A. N. Korotkov, and K. K. Likharev, "Theory of single-electron charging of quantum wells and dots," *Phys. Rev. B*, vol. 44, pp. 6199–6211, Sep 1991. 107
- [221] C. W. J. Beenakker, "Theory of coulomb-blockade oscillations in the conductance of a quantum dot," *Phys. Rev. B*, vol. 44, pp. 1646–1656, Jul 1991. 107
- [222] J. Cao, Q. Wang, and H. Dai, "Electron transport in very clean, as-grown suspended carbon nanotubes," *Nat. Mater.*, vol. 4, pp. 745–749, Oct. 2005. 108
- [223] A. R. Armstrong and P. G. Bruce, "Synthesis of layered limno₂ as an electrode for rechargeable lithium batteries," *Nature*, vol. 381, pp. 499–500, June 1996. 112
- [224] X. Wang and Y. Li, "Selected-control hydrothermal synthesis of α - and β -mno₂ single crystal nanowires," *J. Am. Chem. Soc.*, vol. 124, no. 12, pp. 2880–2881, 2002. 112

- [225] X. Wang and Y. D. Li, "Synthesis and formation mechanism of manganese dioxide nanowires/nanorods," *Chem.-A Europ. Journ.*, vol. 9, pp. 300–306, Jan. 2003. 112
- [226] P. H. Klose, "Electrical properties of manganese dioxide and manganese sesquioxide," *J. Electrochem. Soc.*, vol. 117, no. 7, pp. 854–858, 1970. 113
- [227] J. M. Albella, L. Fernández-Navarrete, and J. M. Martínez-Duart, "Electrical properties of pyrolytic mno₂ layers," *J. Appl. Electrochem.*, vol. 11, pp. 273–279, May 1981. 113, 114
- [228] H. Sato, T. Enoki, M. Isobe, and Y. Ueda, "Transport properties and magnetism of a helically hund-coupled conductor: beta-mno₂," *Phys. Rev. B*, vol. 61, pp. 3563–3569, Feb. 2000. 113
- [229] I. Hellmann. private communication. 113

*"Knowledge is of two kinds.
We know a subject ourselves,
or we know where we can find information upon it."
Samuel Johnson, XVIII*

List of Publications

1. P. Ayala, A. Grüneis, **D. Grimm**, C. Kramberger, R. Engelhard, M. Rümmeli, J. Schumann, R. Kaltofen, B. Büchner, C. Schaman, H. Kuzmany, T. Gemming, A. Barreiro and T. Pichler: *Cyclohexane triggers staged growth of pure and vertically aligned single wall carbon nanotubes* Chem. Phys. Lett., **454**, 332–336, (2008)
2. **D. Grimm**, P. Venezuela, F. Banhart, N. Grobert, H. Terrones, P. Ajayan, M. Terrones and A. Latgé: *Synthesis of SWCNT Rings Made by Two Y Junctions and Possible Applications in Electron Interferometry*, Small, **3**, 1900–1905, (2007)
3. **D. Grimm**, A. Latgé and P. Venezuela: *Standing-wave observations in single-wall carbon nanotube quantum dots and Y-junction rings*, phys. stat. sol. (b), **244**, 4283–4287, (2007)
4. F. Schäffel, C. Kramberger, M. H. Rümmeli, R. Kaltofen, **D. Grimm**, A. Grüneis, E. Mohn, T. Gemming, T. Pichler, B. Büchner, B. Rellinghaus and L. Schultz: *Carbon nanotubes grown from individual gas phase prepared iron catalyst particles*, phys. stat. sol. (a), **204**, 1786–1790, (2007)
5. F. Schäffel, C. Kramberger, M. Rümmeli, **D. Grimm**, E. Mohn, T. Gemming, T. Pichler, B. Rellinghaus, B. Büchner and L. Schultz: *Nanoengineered Catalyst Particles as a Key for Tailor-Made Carbon Nanotubes*, Chem. Mater., **19**, 5006–5009, (2007)
6. A. Latgé and **D. Grimm**: *Band-gap modulations of double-walled carbon nanotubes under an axial magnetic field*, Carbon, **45**, 1905–1910, (2007)
7. A. Barreiro, C. Kramberger, M. Rümmeli, A. Grüneis, **D. Grimm**, S. Hampel, T. Gemming, B. Büchner, A. Bachtold and T. Pichler: *Control of the single-wall carbon nanotube mean diameter in sulphur promoted aerosol-assisted chemical vapour deposition*, Carbon, **45**, 55–61, (2007)
8. P. Ayala, A. Grüneis, T. Gemming, **D. Grimm**, C. Kramberger, M. Rümmeli, F. Freire, H. Kuzmany, R. Pfeiffer, A. Barreiro, B. Büchner and T. Pichler: *Tailoring N-Doped Single and Double Wall Carbon Nanotubes from a Nondiluted Carbon/Nitrogen Feedstock*, J. Phys. Chem. C, **111**, 2879–2884, (2007)

9. P. Ayala, A. Grüneis, T. Gemming, B. Büchner, M. H. Rummeli, **D. Grimm**, J. Schumann, R. Kaltofen, F. L. Freire Jr., H. D. F. Filho and T. Pichler: *Influence of the Catalyst Hydrogen Pretreatment on the Growth of Vertically Aligned Nitrogen-Doped Carbon Nanotubes*, Chem. Mater., **19**, 6131-6137, (2007)
10. H. Shiozawa, H. Rauf, **D. Grimm**, M. Knupfer, M. Kalbac, S. Yang, L. Dunsch, B. Büchner and T. Pichler: *Charge distribution of potassium intercalated $Dy_3N@C_{80}$ observed with core-level and valence-band photoemission*, phys. stat. sol. (b), **243**, 3004–3007, (2006)
11. M. H. Rummeli, C. Kramberger, M. Löffler, M. Kalbác, H. Hübers, A. Grüneis, A. Barreiro, **D. Grimm**, P. Ayala, T. Gemming, F. Schäffel, L. Dunsch, B. Büchner and T. Pichler: *Synthesis of single wall carbon nanotubes with invariant diameters using a modified laser assisted chemical vapour deposition route*, Nanotechn., **17**, 5469-5473, (2006)
12. M. H. Rummeli, A. Grüneis, M. Löffler, O. Jost, R. Schonfelder, C. Kramberger, **D. Grimm**, T. Gemming, A. Barreiro, E. Borowiak-Palen, M. Kalbac, P. Ayala, H. Hubers, B. Büchner and T. Pichler: *Novel catalysts for low temperature synthesis of single wall carbon nanotubes*, phys. stat. sol. (b), **243**, 3101–3105, (2006)
13. A. Grüneis, M. H. Rummeli, C. Kramberger, **D. Grimm**, T. Gemming, A. Barreiro, P. Ayala, T. Pichler, H. Kuzmany, C. Schamann, R. Pfeiffer, J. Schumann and B. Büchner: *Growth of carbon nanotubes from wet chemistry and thin film multilayer catalysts*, phys. stat. sol. (b), **243**, 3054–3057, (2006)
14. A. Grüneis, C. Kramberger, **D. Grimm**, T. Gemming, M. H. Rummeli, A. Barreiro, P. Ayala, T. Pichler, C. Schaman, H. Kuzmany, J. Schumann and B. Büchner: *Eutectic limit for the growth of carbon nanotubes from a thin iron film by chemical vapor deposition of cyclohexane*, Chem. Phys. Lett., **425**, 301–305, (2006)
15. **D. Grimm**, A. Grüneis, C. Kramberger, M. Rummeli, T. Gemming, B. Büchner, A. Barreiro, H. Kuzmany, R. Pfeiffer and T. Pichler: *Catalytic decomposition of n-heptane for the growth of high quality single wall carbon nanotubes*, Chem. Phys. Lett., **428**, 416–420, (2006)
16. H. Shiozawa, H. Rauf, T. Pichler, **D. Grimm**, X. Liu, M. Knupfer, M. Kalbac, S. Yang, L. Dunsch, B. Büchner and D. Batchelor: *Electronic structure of the trimetal nitride fullerene $Dy_3N@C_{80}$* , Phys. Rev. B, **72**, 195409, (2005)
17. A. Latgé, **D. Grimm** and P. Venezuela: *Y-shaped carbon nanotubes: structural stability and transport properties*, J. Mol. Catal. A: Chem., **228**, 125–130, (2005)

18. **D. Grimm**, P. Venezuela and A. Latgé: *Thermal and mechanical stability of Y-shaped carbon nanotubes*, Phys. Rev. B, **71**, 155425, (2005)
19. **D. Grimm**, A. Latgé, R. Muniz and M. Ferreira: *Polymer-doped carbon nanotubes: electronic properties and transport suppression*, AIP Conference Proceedings, **786**, 244–247, (2005)
20. **D. Grimm**, A. Latgé, R. B. Muniz and M. S. Ferreira: *Transport suppression in polymer-doped zigzag carbon nanotubes*, Phys. Rev. B, **71**, 113408, (2005)
21. A. Latgé, R. B. Muniz and **D. Grimm**: *Carbon nanotube structures: Y-junctions and nanorings*, Braz. J. Phys., **34**, 585–589, (2004)
22. **D. Grimm**, R. B. Muniz and A. Latgé: *From straight carbon nanotubes to Y-shaped junctions and rings*, Phys. Rev. B, **68**, 193407, (2003)

CURRICULUM VITAE

Daniel Grimm

10.12.1976	Born in Cologne, Germany
1987-1989	Werner-von-Siemens Gymnasium, München, Germany
1989-1993	Gymnasium am Deutenberg, Villingen-Schwenningen, Germany
1993-1997	Gymnasium Philippinum, Weilburg, Germany
1994-1995	Liceo de Belén, Heredia, Costa Rica
<hr/>	
1997-1998	Civil Service, Integrative Kindertagesstätte, Weilburg, Germany
<hr/>	
1998-2002	Study of Physics, University Freiburg, Germany
2001-2002	Study-abroad at University Federal Fluminense, Rio de Janeiro, Brazil
2002-2003	University Federal Fluminense, Rio de Janeiro, Brazil Masters of Science thesis, supervisor: Prof. Dr. Andrea Latgé <i>Carbon nanotube based Y shaped junctions and rings</i>
2003	Start of PhD research at University Federal Fluminense, Rio de Janeiro, Brazil supervisor: Prof. Dr. Andrea Latgé
2004-2008	Continuing PhD research at the IFW Dresden, Germany supervisor: Prof. Dr. Bernd Büchner

Acknowledgements

In the first place I want to thank my family for all the support during the course of this thesis. Thank you Christiana and Juliano for your joyfulness and for waiting so often until so late after a hard day working in the lab.

Of course, this thesis would not have been finished without the support and fruitful discussions with my supervisors, Prof. Andrea Latgé and Prof. Thomas Pichler. Their enthusiasm for research is very contagious for everyone involved, especially on the field of nanotubes. I would like to thank Prof. Bernd Büchner for giving me the possibility and confidence to proceed the experimental work at the IFW Dresden.

Many people contributed to this work. Danny Haberer, who's diploma thesis I had the pleasure to supervise; together we succeeded in the fabrication of the first working devices after a very hard time work. I acknowledge the help of Joseph Biberger & Ralph Pulwey from *nanonic, Germany* who helped me to bugfix our new SEM equipment. Certainly, the lithography facility would not be half the way without them. Thanks to Mark Rummeli for all the great TEM images and fruitful discussions about CVD. Claudia Gomes, Pedro Venezuela and Roberto Bechara, muito obrigado for all the important theoretical input. Mauricio Terrones, I am grateful for the TEM experiments you did on the Y-Junction rings demonstrating their realization. Thanks to our Austrians, Alex Grüneis and Christian Kramberger for all the CVD processes we made in parallel as well as many other lab-matters. I acknowledge Amelia Barreiro and Paola Ayala for the interesting time we had at the CVD lab and in our 'panorama' room. Special thanks to Hartmut Vinzelberg for all the discussions we had concerning the fascinating transport properties of nanotubes and for the help on the transport measurements. I acknowledge the support of the whole group 11, especially Martin Knupfer, Roland Hübel, Hide Shiozawa, Ronny Schönfelder, Stefan Leger, and not to forget the former 11er Hendrik Rauf. Thanks to Cesar Bof Bufon and Ronny Engelhard for the fast(!) and countless metallizations, especially near the end of the thesis. I acknowledge Thomas Mühl and Andreas Winkler for all the time we spent together in front the AFM. Thanks to Ingolf Mönch and Joachim Schumann for the discussions concerning our clean room facility, Rainer Kaltoven for the sputtering and Horst Wendrock for the FIB milling. I acknowledge Hallen Daniel for her help in understanding the chemistry of ferritins. Thank you Siggy Pichl for the technical assistance on our SEM and for being always so cordially. Also Barbara Eichler and Sandra Sieber for some of the

processing steps and fruitful discussions about the EBL. To all my room-mates, for all the discussions about physics and non-physics, Markus Löffler (our other TEM man), Mandy Grobosch (the never sleeping woman) and Norman Leps (has always something interesting to tell). I acknowledge the support of our theoretical institute, specially Ulrike Nietzsche, and the possibility to use the computer cluster *digedag* where part of the simulations were done. To Manja Maluck and Kerstin Höllner who are the good souls of the institute, keeping things running.

I appreciate all the help of my friends to live the life outside of the institute. Our neighbors Ute Queitsch, Tine Hamann, Franzi Schäffel (who is currently joining our nanotube group, good luck!), Franzi Thoss and Bert Lange. Of course not to forget the small ones, Luka, Carla and Luise. To all the other members of our IFW band *nanonic*, Nadja Wizen, Tom Woodcock, Rudi Schäfer, Glen Guhr and Elias Mohn. Together we rock the world! Not to forget the rock man Martin Pötschke (climbs everything), Basti Tröger, Susi Thoss, Uwe Gaitzsch and Julia Lyubimova (for the frequent tea sessions). And my former colleagues in Freiburg and now friends elsewhere, Inga Müller, Florian Dähne, Dirk Vetter, Stefan Meckler, Jochen Mikosch, Andreas Thoman and Patricia Hagendorn. Y claro, a mi hermano tico, Bryan Corrales Lara.

Very important influence on the success of this work had also all my Brazilian friends who expected me always with open arms. It is a pity that we can see us only so sparsely. So, thank you so much Carla Carvalho, Bernardo Mosquera, Suenne Riguette, Renata Rangel, Renata Zocatelli, Bernardo Coutinho, Karen Luz, Fernanda Hingel, Ze Augusto and all the other people in the Physics Institute at UFF. The folk of the *unicerj* for all the climbing and trekking weekends in the mountains, especially Buarque, Bonolo, Godinho, Gabriela, Rodrigo, Willy and all the others. A special thank to the people of the PUC, Sandra, Patricia, Amalia and Maria Christina who helped to organize the important conference in Búzios where I had the pleasure to meet Christiana.

Special attention deserves my family who saw me studying and researching always far away. Thank you Mam and Dad.

Livros Grátis

(<http://www.livrosgratis.com.br>)

Milhares de Livros para Download:

[Baixar livros de Administração](#)

[Baixar livros de Agronomia](#)

[Baixar livros de Arquitetura](#)

[Baixar livros de Artes](#)

[Baixar livros de Astronomia](#)

[Baixar livros de Biologia Geral](#)

[Baixar livros de Ciência da Computação](#)

[Baixar livros de Ciência da Informação](#)

[Baixar livros de Ciência Política](#)

[Baixar livros de Ciências da Saúde](#)

[Baixar livros de Comunicação](#)

[Baixar livros do Conselho Nacional de Educação - CNE](#)

[Baixar livros de Defesa civil](#)

[Baixar livros de Direito](#)

[Baixar livros de Direitos humanos](#)

[Baixar livros de Economia](#)

[Baixar livros de Economia Doméstica](#)

[Baixar livros de Educação](#)

[Baixar livros de Educação - Trânsito](#)

[Baixar livros de Educação Física](#)

[Baixar livros de Engenharia Aeroespacial](#)

[Baixar livros de Farmácia](#)

[Baixar livros de Filosofia](#)

[Baixar livros de Física](#)

[Baixar livros de Geociências](#)

[Baixar livros de Geografia](#)

[Baixar livros de História](#)

[Baixar livros de Línguas](#)

[Baixar livros de Literatura](#)
[Baixar livros de Literatura de Cordel](#)
[Baixar livros de Literatura Infantil](#)
[Baixar livros de Matemática](#)
[Baixar livros de Medicina](#)
[Baixar livros de Medicina Veterinária](#)
[Baixar livros de Meio Ambiente](#)
[Baixar livros de Meteorologia](#)
[Baixar Monografias e TCC](#)
[Baixar livros Multidisciplinar](#)
[Baixar livros de Música](#)
[Baixar livros de Psicologia](#)
[Baixar livros de Química](#)
[Baixar livros de Saúde Coletiva](#)
[Baixar livros de Serviço Social](#)
[Baixar livros de Sociologia](#)
[Baixar livros de Teologia](#)
[Baixar livros de Trabalho](#)
[Baixar livros de Turismo](#)